Novel roles of the adaptor-associated kinase 1 (AAK1)

Andrea Lius

A dissertation
submitted in partial fulfillment of the
requirements for the degree of
Doctor of Philosophy

University of Washington
2025

Reading Committee:
Shao-En Ong, Chair
Ning Zheng
Dustin James Maly

Program Authorized to Offer Degree:
Pharmacology

University of Washington

Abstract

Novel roles of the adaptor-associated kinase 1 (AAK1)

Andrea Lius

Chair of Supervisory Committee:

Shao-En Ong

Pharmacology

Epithelial-mesenchymal transition (EMT) is a reversible cellular program that is involved in normal biological processes, such as embryogenesis and wound healing, and pathological processes, such as fibrosis and cancer. In cancer, EMT can drive therapeutic resistance and metastasis, the hallmarks of malignancy. We recently developed a mass spectrometry-based proteomics approach to study protein complexes in native cells and tissues. Using this tool, we characterized protein complexes that are differentially enriched between epithelial-like and mesenchymal-like states in hepatocellular carcinoma (HCC). We found that the adaptor associated kinase 1 (AAK1) protein complex is highly enriched in mesenchymal-like HCC cells and tissues, and that the depletion of AAK1 resulted in EMT reversal. Before this, AAK1 was mostly known for its role in the regulation of Clathrin-mediated endocytosis through the phosphorylation of adaptor protein 2, and it was never directly linked to cancer or EMT. We also identified U3 small nucleolar RNA-associated protein 25 homolog (UTP25), an understudied nucleolar protein, as one of AAK1's interacting partners. We showed that the depletion of UTP25, like AAK1, produced phenotypes that are consistent with EMT reversal. Finally, through our investigation of AAK1's

functional relationship with UTP25, we discovered that AAK1 can localize to the nucleus, and that this nuclear localization may have isoform-specific preference.

Table of contents

List of figures

Glossary

Abbreviation	Full name
aa	Amino acid
AAK1	Adaptor-associated kinase 1
ADRBK2	β-adrenergic receptor kinase
AID	α-adaptin-interacting domain
AiP	Apoptosis-induced proliferation
AKAP	A-kinase anchoring protein
ALK	Anaplastic lymphoma kinase
ALS	Amyotrophic lateral sclerosis
AP	Adaptor protein
AP2M1	AP2 subunit μ2
APEX	Ascorbate peroxidase
AP-MS	Affinity purification mass spectrometry
aPKC	Atypical protein kinase C
ASCH	Activation segment C-terminal helix
ATCC	American Type Culture Collection
ATM	Ataxia-telangiectasia mutated
ATP	Adenosine triphosphate
AURK	Aurora kinase
AUTS2	Autism susceptibility gene 2 protein
AXL	Tyrosine-protein kinase receptor UFO
BIKE, BMP2K	BMP2-inducible kinase
BH	Benjamini-Hochberg
bp	Basepair
BSA	Bovine serum albumin
CAM	Chloroacetamide
CaMK1	Ca^{2+}/calmodulin-dependent protein kinase I
CAPN3	Calpain 3
CBD	Clathrin-binding domain
CBL	E3 ubiquitin ligase CBL
CCLE	Cancer Cell Line Encyclopedia
CCV	Clathrin-coated vesicle
CDK	Cyclin-dependent kinase
cDNA	Complementary DNA
CHC	Clathrin heavy chain
CHEK	(Cell cycle) checkpoint kinase
CID	Collision-induced dissociation
CK	Casein kinase
CLC	Clathrin light chain
CME	Clathrin-mediated endocytosis
Ct	Threshold cycle
CoIP/MS	Co-immunoprecipitation/mass spectrometry
CSL	CBF-1/RBPJ-κ, Suppressor of Hairless, or Lag-1
DEA	Differential expression analysis
Def, DIEXF	Digestive expansion factor (also see UTP25)

DMEM	Dulbecco's minimum essential medium
DMSO	Dimethyl sulfoxide
DNA	Deoxyribonucleic acid
DTT	Dithiothreitol
EC_{50}	Half maximal effective concentration
ECL	Enhanced chemiluminescence
EDTA	Ethylenediaminetetraacetic acid
EGF	Epidermal growth factor
EGFR	Epidermal growth factor receptor
eIF-3	Eukaryotic translation initiation factor 3
EMP	Epithelial-mesenchymal plasticity
EMT	Epithelial-mesenchymal transition
EPHA2	Ephrin receptor A2
FA	Formic acid
FBS	Fetal bovine serum
FDR	False discovery rate
FGF1	Fibroblast growth factor 1
FGFR	Fibroblast growth factor receptor
FISH	Fluorescent in situ hybridization
fmPPI	Functional marker protein-protein interaction
FSBA	Fluorosulphonylbenzoyladenosine
FZD	Frizzled (receptor)
GAK	Cyclin G-associated kinase
GAP	GTPase activating protein
GAPDH	Glyceraldehyde-3-phosphate dehydrogenase
GdnHCl	Guanidine hydrochloride
GFP	Green fluorescent protein
GO	Gene ontology
GOI	Gene of interest
GOBP	Gene ontology biological process
GOCC	Gene ontology cellular component
GOMF	Gene ontology molecular function
GPCR	G-protein coupled receptor
GRB2	Growth factor receptor-bound protein 2
GSEA	Gene set enrichment analysis
GSK3B	Glycogen synthase kinase-3 beta
GTP	Guanosine triphosphate
HBS	HEPES-buffered saline
HCC	Hepatocellular carcinoma
HCl	Hydrochloride
HCV	Hepatitis C virus
HGF	Hepatocyte growth factor
HAP	Hydroxyapatite
HEK	Human embryonic kidney (cells)
HRP	Horseradish peroxidase
IAV	Influenza A virus

IC_{50}	Half maximal inhibitory concentration
IF	Immunofluorescence
IP-MS	Immunoprecipitation-mass spectrometry
IQR	Interquartile range
kb	kilobase
KCLB	Korean Cell Line Bank
kDa	kiloDalton
KI	Kinase inhibitor
kiCCA	kinobead competition and correlation analysis
KIP	Kinase interactome probe
KS	Kolmogorov-Smirnov (test)
LC-MS	Liquid chromatography-mass spectrometry
LCMV	Lymphocytic choriomeningitis virus
LDS	Lithium dodecyl sulfate
LKB1	Liver kinase B1
lncRNA	Long noncoding RNA
LPS	Lipopolysaccharide
LRP	Low-density lipoprotein receptor-related protein
MAPK	Mitogen-activated protein kinases
Mdm2	Mouse double minute 2
MET	Mesenchymal-epithelial transition
MIB	Multiplexed inhibitor beads
miRNA	MicroRNA
MPSK1	Myristoylated and palmitoylated S/T kinase 1
mRNA	Messenger RNA
MS	Mass spectrometry
mTOR	Mammalian target of rapamycin
MYLK	Myosin light-chain kinase
NaCl	Sodium chloride
NaF	Sodium fluoride
NAK	Numb-associated kinase
NaOH	Sodium hydroxide
NDR	Nuclear dbf2-related kinase
NES	Normalized enrichment score
Nicd	Notch intracellular domain
nLC	Nano-scale liquid chromatography
NLS	Nuclear localization sequence
NMP	Noradrenergic-mesenchymal plasticity
NTL	Non-tumor liver (tissue)
PBS	Phosphate buffered saline
PCR	Polymerase chain reaction
PD-1	Programmed cell death protein 1
PDPK	Phosphoinositide-dependent protein kinase
PI3RK2	Phosphatidylinositol 3-kinase regulatory subunit 2
PKA	Protein kinase A
PPI	Protein-protein interaction

PRC	Polycomb repressive complex
PRKAA	Protein kinase AMP-activated catalytic subunit alpha
PSMB2	Proteasome subunit beta type-2
PTM	Post-translational modification
PXN	Paxillin
qPCR	Real-time PCR
RALBP1	RalA binding protein 1
rcf	Relative centrifugal force
rpm	Revolutions per minute
REPS1/2	RALBP1-associated Eps domain-containing protein 1/2
RNA	Ribonucleic acid
RNAi	RNA interference
ROC	Receiver operating characteristic (curve)
rRNA	Ribosomal RNA
R-spine	Regulatory spine
SDS-PAGE	Sodium dodecyl-sulfate polyacrylamide gel electrophoresis
SHC1	SHC-transforming protein 1
shRNA	Short hairpin RNA
siRNA	Small interfering RNA
SOS1	Son of sevenless homolog1
SSU	(Ribosome) small subunit
S/T	Serine/threonine
STK	Serine/threonine kinase
TAE	Tris-acetate-EDTA (buffer)
TANK	TRAF family member-associated NF-kappa-B activator
TBK1	TANK-binding kinase 1
TBS	Tris-buffered saline
TBS-T	TBS-Tween20 (buffer)
TCEP-HCl	Tris(2-carboxyethyl)phosphine hydrochloride
TEAB	Triethylamine bicarbonate
TGFβ	Transforming growth factor-beta
TRC	The RNAi consortium
UTP25	U3 small nucleolar RNA-associated protein 25 homolog (also see Def, DIEXF)
VAV3	Guanine nucleotide exchange factor VAV3
WT	Wild type
YWHAZ	14-3-3 protein zeta/delta

Acknowledgments

I thank and acknowledge my thesis advisor, Shao-En Ong, for his guidance, support and mentorship in the past five years. I also thank current members and alumni of the Ong lab, particularly Martin Golkowski and Tanmay Sapre, for their guidance, discussion and friendship; and Claude Beltejar, Daphnee Marciniak and Alyah Perkins for their support and contributions to my project. I am grateful to other members of my thesis committee: Bill Mahoney, Dustin Maly, Yasemin Sancak and Ning Zheng, for their advice, encouragement and support; members of the Scott, Sancak and Shechner labs for sharing their expertise, reagents and equipment; and the department's chair and administrative staff: John Scott, Debbie Bale and Jenny Nelson, for their support.

I thank the mentors of my undergraduate and post-baccalaureate years: Ben Sugg, Sadie Rosenthal, Peggy Harbol, Dan Smith, Brett Kaiser and Karol Bomsztyk, for believing in my potential and instilling my love for science; and my science communication mentors: Comfort Dorn, Marissa Locke Rotttinghaus, Allison Frick, Meenakshi Prabhune, Sarah Ellinwood, Mallory Smith and Ellen Kuwana, for helping me find a place where I would not have to choose between my appetite for science and my love of words. I also thank Andrea Pereyra, Maksim Dolmat and Sharona Gordon for always providing me with a safe space to share my hardships and frustrations.

I thank Kacey Rosenthal, Cameron Smith, Suzie and Jay Klauda, Maryanne Kihiu, Anna Elmaris and Alex Bilba, for being my family in Seattle and for making my days here much less gloomy than the weather. I thank Kacey, Cam, Anna and Alex for welcoming me into their families and for being the siblings I never had. I feel incredibly lucky to have met Kacey in graduate school and grateful that we became inseparable despite our near-opposite personalities and interests. She celebrates me at my best and lifts me up at my worst, and failing that, she sticks by me anyway. I

will miss and forever cherish the early mornings we shared at barre, the afternoons we spent finding the perfect lunch table with both sunshine and shade, and the late nights we drank and danced away at bars. I am grateful to Anna for introducing me to The New York Times' daily puzzles, for being the best aunt to Jasper, and for always bearing with my complaints about work, school, books and occasionally, though rarely, her brother. Although I tend to introduce Cam and Alex as Kacey's and Anna's partners rather than as my friends, they are some of the best and closest friends I have ever had. As a child, I used to wish for an older brother—now, I have two. As excited as I am for what comes next, I am saddened by the thought of having to leave all of them behind.

My gratitude for my parents, Fujianto Lius and Linda Gumulia, my grandmother, Ellen Swandayani, extend far beyond words. I am forever indebted to my parents, who have given me their everything and more so I could be the person that I am today, and my grandmother, who helped raise me and remembers every single part of my story better than anyone, including myself. Ever since I was born, they have always put me first and done everything with me in mind. In everything that I do, I hope that I am making them proud. I hope they always remember how much I love and appreciate them, even when my words fail me.

I feel incredibly lucky to have Vlad Neoberdin as my partner and my very best friend. The light in which he sees me has gotten me through my hardest times and inspires me to be a better person each day. I am grateful that we never tire of each other, no matter how much time we spend together or where we are—on vacation, in the car, on the couch and even on the phone.

And last but not least, I wish to acknowledge my sons, nephews and nieces: Jasper, Gillis, Millis, Pushok, Zola, Lily, Bubba and Riley, whose love for me lacks words, but is unconditional, unfaltering and timeless.

Chapter One: Introduction

1.1. Epithelial-mesenchymal transition (EMT) can promote cancer malignancy

Epithelial-mesenchymal transition (EMT) is a reversible process in which cells lose epithelial phenotypes, such as a cobblestone-like appearance, apical-basal polarity, fast proliferation and low migratory capacity, and gain mesenchymal phenotypes, such as a spindly appearance, front-to-back polarity, slow proliferation and high migratory capacity. Elizabeth Hay first described epithelial mesenchymal "transformation" in embryonic development in the 1960s.[1, 2] After scientists discovered the role of EMT transcription factors, such as SNAIL, in cancer in the early 2000s, they changed the word transformation to "transition" in order to prevent it from being confused with neoplastic transformation in cancer biology, the process by which normal cells become cancerous.[2, 3]

EMT is now widely known to be involved in normal processes in the cell such as embryogenesis and wound healing, and the development of pathological conditions such as fibrosis and cancer. The process can be induced by various growth factors, such as hepatocyte growth factor (HGF), fibroblast growth factor 1 (FGF1) and transforming growth factor-beta (TGFβ).[2, 4-7] EMT is also regulated by many different things in the cells, such as transcription factors, epigenetics, microRNAs (miRNAs), long noncoding RNAs (lncRNAs) and post-translational modifications (PTMs).[7] Both the induction and regulation of EMT are typically also context dependent, which can make research on this topic challenging. Another reason why studying EMT is often difficult is because the process occurs in a spectrum and is often incomplete, so cells that undergo EMT are typically in intermediate states with mixed epithelial and mesenchymal features.[2, 7] For instance, different variations of EMT are activated to different extents in different cancers, so the process cannot be universally described by a constrained set of molecular markers.[2, 7] Yet despite these challenges, there was a dramatic increase in EMT-related studies in the literature since it was connected to cancer.[2]

The study of EMT in cancer is important because multiple studies have linked EMT to therapeutic resistance and metastatic tendency, the hallmarks of cancer malignancy.[2, 7] Thus, the connection between EMT and cancer malignancy suggests that targeting EMT may overcome key challenges in improving cancer patient prognoses, especially in malignant cases. In the field, it is widely understood that cancer cells in early stages of the disease are more epithelial like, then gradually acquire mesenchymal phenotypes as the disease progresses to later.[7] It is also commonly known that mesenchymal-epithelial transition (MET), the reverse of EMT, takes place once mesenchymal-like tumor cells have spread to distant organs in order to establish metastatic colonies.[7] According to Yang et al., although EMT may not always be necessary for metastasis, at least a transient and partial activation of the process is likely required.[2] Similarly, Dongre and Weinberg stated that the malignant progression of “quite possibly all” types of carcinomas depends on EMT activation in cancer.[7]

In addition to therapeutic resistance and migratory capacity, cancer EMT has also been connected to cell proliferation rates. In fact, one of the reasons why EMT is thought to impact drug resistance is because it promotes slow proliferation and/or cell cycle arrest.[8] Not surprisingly, EMT is regulated by signaling pathways that are important in proliferation, such as Wnt and Notch.

The Wnt signaling pathway regulates many processes in the cell, including proliferation, differentiation and migration. In the canonical pathway, Wnt ligands binds to Frizzled (Fzd) receptors, and this leads to cascade of molecular events that eventually leads to the translocation of β-catenin to the nucleus, where it acts as a transcription factor. Wnt is known to promote EMT in development; it has also been shown to regulate EMT to promote malignancy in several types of cancer, such as lung adenocarcinoma and metastatic colon cancer.[7, 9-10]

E-cadherin, a classical epithelial marker, negatively regulates Wnt by sequestering it at the membrane.[7] SNAIL, an EMT transcription factor, can render cells more sensitive to Wnt signaling.[7, 11] β-Catenin interacts with other transcription factors that act on EMT transcription factors SLUG, ZEB1 and TWIST.[7, 12] There is also crosstalk between Wnt and TGFβ, another EMT-promoting pathway: multiple studies have shown that β-Catenin interact with SMAD complexes downstream from TGFβ to regulate cell adhesion and metastasis.[7, 13-15]

The Notch signaling pathway also regulates cell proliferation and differentiation. Transmembrane Notch receptors bind to Delta or Jagged ligands, and this eventually leads to the cleavage of the Notch intracellular domain (Nicd) and its translocation to the nucleus, where it acts as a transcription factor. Notch has been shown to regulate EMT in different types of cancer, such as breast, lung, pancreatic and squamous cell carcinomas.[7, 16-19] It is thought to promote EMT by acting on EMT transcription factors such as SNAIL and SLUG.[20, 21] Like Wnt, Notch also has crosstalk with TGFβ to promote EMT via SMAD complexes.[7]

In mammals, the protein Numb is known to inhibit Notch by promoting its ubiquitylation. This negative regulation mechanism has been shown to impact EMT in triple-negative breast cancer.[7, 16] Numb and Notch also have established roles in endocytosis through its relationship with a family of proteins known as Numb-associated kinases (NAKs).

1.2. AAK1 is a member of the Ark1/Prk1 protein family

The adaptor-associated kinase 1, or AAK1, is a serine/threonine (S/T) kinase that was first identified in a phage display screen which used α-adaptin, a subunit in the adaptor protein 2 (AP2) complex, as a bait in a rat brain cDNA library.[22] In this paper, the authors showed that AAK1 interacts with adaptor proteins (APs), clathrin and clathrin-coated vesicles (CCVs), and specifically phosphorylate the μ1 and μ2 subunits of the AP2 complex for the first time.[22] AAK1 was initially identified in the brain. Biochemical fractionation experiments in bovine brain samples showed that AAK1 is highly enriched in the cell membrane and the presynaptic terminals.[22] The authors also found that AAK1 colocalized with endocytic markers, such as clathrin, AP2 and dynamin 1.[22]

AAK1 contains an N-terminal kinase domain, a "QPA-rich" middle domain (28% glutamine, 18% proline, 13% alanine) and a C-terminal domain with DPF, NPF and DLL motifs, which are known to be important for endocytosis.[22] Based on sequence similarity, AAK1 was classified as a member of the Ark1/Prk1 protein family.[22] Members of the Ark1/Prk1 protein family share a lot of identity in their kinase domains, but not much elsewhere. The human protein BMP2-inducible kinase (BMP2K or BIKE), the closest AAK1 homolog, only shares approximately 50% sequence identity with AAK1.[23] It shares 74% identity with AAK1 in the kinase domain but only 28% in the QPA-rich domain.[22, 23] Numb-associated kinase (NAK), AAK1's homologue in *Drosophila melanogaster*, shares 66% of homology in its kinase domain; it also has the DPF and DLL motifs.[22, 24]

Members of the Ark1/Prk1 protein family are defined by their N-terminal kinase domain and a conserved substrate phosphorylation site (L(I)XXQXTG).[24] All known Ark1/Prk1 kinases, from yeasts to mammals are involved in endocytosis and are regulated by cycles of phosphorylation and dephosphorylation.[24] More recently, members of the Ark1/Prk1 protein family in higher organisms have been referred to as Numb-associated kinases (NAKs), whose name originated from the NAK protein in *Drosophila*. There are four NAKs in humans: AAK1, BIKE, cyclin G-associated kinase (GAK) and myristoylated and palmitoylated serine/threonine kinase 1 (MPSK1/STK16).[23] Phylogenetic analysis revealed that AAK1 and BIKE are the most closely related to NAK.[23]

Sorrell et al. solved crystal structures of AAK1 and BIKE, revealing unique structural properties of these kinases and other NAKs.[23] Based on crystallography experiments, the authors reported that AAK1 and BIKE predominantly exist as monomers.[23] They also found that NAKs are likely constitutively active, as the regulatory spine (R-spine) is aligned even in a dephosphorylated state—a kinase's R-spine is aligned in its active state and "broken" in its inactive state.[23] In addition, the authors found that dephosphorylated AAK1 can still achieve a catalytically competent conformation.[23]

Sorrell et al.'s study also revealed several structural features of NAKs that differ from typical kinases. The authors found that NAKs have an additional large α-helix C-terminal to the kinases' activation segment, another regulatory element whose confirmation affects substrate interactions and catalytic efficiency—they called this structure activation segment C-terminal helix (ASCH).[23] They also observed that the glycine-rich "P loop", a flexible phosphate-binding region at the ATP site, in NAKs do not conform to the G-X_1-G-X_2-φ-G motif.[23] The third G is replaced with S in MPSK1, and first and third G's are replaced with A's or A and S in AAK1 and GAK and BIKE, respectively.[23]

1.3. AAK1 mediates clathrin-mediated endocytosis

The literature has extensively characterized AAK1's involvement in clathrin-mediated endocytosis (CME) through the phosphorylation of the AP2 protein complex subunits. The AP2 complex has four subunits: two large (α and β2), one medium (μ2) and one small (σ2). The α and β2 subunits recruit critical endocytic components, the μ2 subunit regulates the interaction between the cargo and the endocytic machinery and the σ2 subunit stabilizes the core of the complex. Assembly of clathrin and the AP2 complex is regulated by phosphorylation and dephosphorylation reactions. For instance, phosphorylation of the μ2 subunit increases the binding affinity of AP2 to tyrosine-based motifs in the cytoplasmic side of membrane-bound receptors that have been targeted for endocytosis.

AAK1 has been described as an atypical kinase because its reaction rate is not limited by substrate concentration, rather, by its own concentration.[25] In this paper, the authors found that a two-fold increase in AP2, incubated with a fixed concentration of AAK1, only increased μ2 phosphorylation by 30%.[25] On the other hand, when the authors incubated an increasing concentration of AAK1 with a fixed concentration of AP2, they observed a stepwise increase in μ2 phosphorylation with increasing AAK1.[25] The increase in μ2 phosphorylation eventually plateaued at the maximum AAk1 concentration, which suggested that the concentration of AAK1, not its substrates, limits its rate of enzymatic reaction.

AP2 μ2 is known to be phosphorylated at T156.[26, 27] In 2002, Ricotta et al. showed that AAK1 was likely AP2's endogenous kinase, although they never validated the connection between AP2 μ2's phosphorylation by AAK1 and this phosphorylation site.[28] The authors showed that phosphorylation by AAK1 increased μ2's binding affinity to tyrosine-based sorting signals on endocytosis targets.[28] In their experiments, they used a synthetic peptide which represented the tyrosine-based sorting motif on lysosomal acid phosphatase.[28] They found that treating AP2 with phosphatases resulted in a fourfold decrease in binding affinity, while incubating it with ATP resulted in an eightfold increase.[28] Furthermore, the authors showed that incubation of AP2 with both ATP and AAK1 caused a sixfold increase in its binding activity to the tyrosine-based sorting motif, and there was a 25-fold increase in the binding affinity of AAK1-phosphorylated AP2 when directly compared to dephosphorylated AP2.[28]

The authors noted that GAK was also previously reported to phosphorylate AP2 μ2, so they investigated how the two kinases associate with AP2.[28, 29] The authors found that both AAK1 and

GAK are found in clathrin-coated vesicles from pig brain.[28] However, by performing hydroxyapatite (HAP) chromatography, the authors showed that GAK mostly co-purified with AP1, while AAK1 with AP2—suggesting that AAK1 is the kinase that phosphorylates AP2 μ2.[28] The authors found that 1mM of *N*-ethylmaleimide abolished μ2 phosphorylation by endogenous and purified AAK1, while 20nM of staurosporine, a broad-spectrum PKC inhibitor, produced a significant decrease in μ2 phosphorylation.[28]

Interestingly, in their 2002 paper, Conner and Schmid found that the overexpression of AAK1 resulted in a decrease in the sequestration of transferrin, a CME target, by AP2. They also showed that they could reduce this inhibitory effect by inactivating AAK1 via treatment with fluorosulphonylbenzoyladenosine (FSBA), an ATP analogue that irreversibly binds to the ATP-binding site. The authors proposed that the inhibition of transferrin uptake was due to additional AAK1 kinase activity.[22] They also tested the effects of wild-type (WT) and kinase-dead AAK1 overexpression on epidermal growth factor (EGF) uptake.[30] Unlike with transferrin, the authors found that AAK1 overexpression did not affect EGF internalization, which suggested that AAK1-mediated endocytosis may be cargo-specific.[30]

To investigate a possible mechanism for the inhibitory effect of AAK1 overexpression on transferrin uptake, the authors immunoprecipitated the AP2 complex from cells overexpressing WT and kinase-dead (K74A and D176A mutants) AAK1 and observed the change in the phosphorylation of AP2 complex subunits.[30] Surprisingly, the authors found that the significant decrease in the phosphorylation occurred on the large AP2 subunits, not μ2, which they had previously shown AAK1 to phosphorylate.[30] Based on this, the authors proposed that the inhibition of AP2 function upon AAK1 overexpression likely results from the binding of AAK1 to AP2 that is independent from its kinase activity.[30]

In contrast to the observable effects of AAK1 expression, siRNA knockdown of AAK1, which reduced AAK1 expression by about 80%, in A549 and HeLa human cell lines did not affect μ2 phosphorylation or transferrin internalization.[30] The authors proposed two possible explanations for these observation: compensation by functionally redundant kinases in the Ark1/Prk1 family or that the remaining 20% of AAK1 in the cell was enough to maintain the normal amount of μ2 phosphorylation.[30]

AAK1's activity on μ2 is at least partially influenced by the clathrin triskelia, three-legged protein complexes which are building blocks of the clathrin coat, cage-like structures that form around cell membranes and eventually bud off during endocytosis. Clathrin stimulates AAK1's phosphorylation of μ2, and assembled clathrin cages have about twice as much of an effect than unassembled clathrin triskelia.[30]

The clathrin triskelia consist of three heavy chains (CHCs) and three light chains (CLCs), both of which interact with AAK1.[25] They found that CHCs can interact with all regions of AAK1, although it has the greatest affinity to the N-terminal two-thirds of the protein.[25] On the other hand, CLCs seem to mostly bind to AAK1's kinase domain and clathrin-binding motif, located within a C-terminal region known as the α-adaptin-interacting domain (AID).[25] A previous study also reported that AAK1's C-terminal AID is the major binding site for AP2, as AAK1 constructs that lack this region fail to recruit AP2 or phosphorylate μ2.[30]

To date, AAK1's known physiological substrates are AP1 (T154), AP2 (T156), Numb (T102) and Eps15.[31] The roles of AAK1 in Numb and Notch signaling will be explored in a later section. AAK1 is also known to autophosphorylate.[22] Sorrell et al. showed that the kinase, grown in *Escherichia coli*, can autophosphorylate at residues T207 and S235 on the activation loop, along with other sites (S115/S116, T144/T147, T170) (2016).[23]

1.4. AAK1 regulates various molecular pathways in the cell

Wnt

In the literature, AAK1 has been described to negatively regulate Wnt signaling: AAK1 knockdown in mouse embryonic stem cells upregulated Wnt signaling, and AAK1 was reported to regulate Wnt signaling through negative feedback via endocytosis of low-density lipoprotein receptor-related protein 6 (LRP6), a receptor for Wnt ligands.[32, 33]

In the presence of Wnt, LRP5/6 associates with Frizzled (FZD) receptors, and this leads to the stabilization of β-catenin. Agajanian et al. found that small interfering RNA (siRNA) silencing of AAK1 in fibrosarcoma and colon cancer cell lines resulted in the stabilization of β-catenin.[33] The authors also found that AAK1 silencing increased the expression of Wnt target genes *AXIN2* and *NKD1*, and this effect was reversed when they overexpressed AAK1.[33] Agajanian et al. showed that AAK1's regulation of Wnt is dependent on its kinase activity, because when they treated cells with SGC-AAK1-1, a specific AAK1 inhibitor (IC_{50} = 240 nM; BIKE IC_{50} = 600-1.5uM), they observed phenotypes that mimic AAK1 silencing.[33] Furthermore, overexpression of AAK1 constructs that lack kinase activity or AP2 binding fail to destabilize β-catenin.[33]

The authors also found that the treatment of cells with WNT3A, a ligand in the Wnt signaling pathway, induced AP2M1 phosphorylation, and that this effect was blocked by the addition of SGC-AAK1-1, the AAK1 inhibitor.[33] WNT3A treatment also resulted in decreased surface expression of LRP6 and its association with AAK1, and treatment with SGC-AAK1-1 rescued the reduction in LRP6 surface expression.[33] These results indicate the negative feedback regulation of Wnt signaling via AAK1-mediated endocytosis.

Numb

Numb is a protein with established roles in development and endocytosis. It is best known for its negative regulation of Notch signaling, specifically in *Drosophila*.[34] Scientists had previously identified Numb as an interactor of NAK, the AAK1 homolog in *Drosophila*, in a yeast two-hybrid screen.[35] In 2008, Sorensen and Conner found that AAK1 interacts with and phosphorylates Numb. This interaction and phosphorylation were abrogated when the researchers mutated a conserved threonine residue on Numb (T102) to an alanine.[36]

Sorensen and Conner also showed that phosphorylation by AAK1 altered Numb's localization in the cell.[36] In endogenous contexts, Numb is found at the plasma membrane and perinuclear endosomes. Sorensen and Conner observed that overexpression of wild-type AAK1, but not kinase-dead AAK1 (K74A and D176A mutants), increased Numb's perinuclear localization.[36] Conversely, depletion of AAK1 and T102A mutation caused Numb to localize more to the plasma membrane.[36] Moreover, the authors found a significant increase in the co-localization of T102A Numb, compared to its wild-type counterpart, with endocytic coat proteins such as AP2, Eps15 and epsin, which suggested the disruption of endocytic vesicle formation due to increased stability of clathrin-coated pits.[36] Moreover, the authors found that T102A Numb overexpression disrupted the endocytosis of transferrin, but not EGF.[36] This evidence for cargo selectivity was consistent with a previous finding in the literature.[30]

Besides AAK1, Numb is also known to be phosphorylated by Ca^{2+}/calmodulin-dependent protein kinase I (CaMKI) and atypical protein kinase C (aPKC) at multiple sites.[37, 38] Likely due to the existence of multiple phosphorylation sites, WT Numb is known to migrate on SDS-PAGE as a doublet, with the larger species migrating about 10kDa slower than its smaller counterpart.[36, 39, 40] Phosphatase treatment caused Numb to migrate as a single band at the doublet's molecular weight.[39] Sorensen and Conner observed that AAK1 knockdown mimicked this effect of phosphatase treatment, suggesting that phosphorylation by AAK1 might be necessary to "prime" Numb for phosphorylation by other kinases.[36]

Notch

The transmembrane protein Notch is activated by two cleavage events: the removal of its extracellular domain by a metalloprotease and the release of its intracellular domain (Nicd) by γ-secretase, where it will translocate to the nucleus and act as a transcription factor. In mammals, γ-secretase cleavage of activated, membrane-tethered Notch requires both monoubiquitination and endocytosis.[41, 42]

In 2011, Gupta-Rossi et al. showed AAK1 as a positive regulator Notch signaling using a CSL firefly luciferase reporter assay.[41] CSL stands for CBF-1/RBPJ-κ, Suppressor of Hairless, or Lag-1, transcription factors in the Notch signaling pathway in mammals, *Drosophila*, and *Caenorhabditis elegans*, respectively. As expected, the introduction of γ-secretase-cleaved, activated Notch (ΔE) dramatically increased Notch signaling pathway activity. In addition, the authors showed that AAK1 knockdown caused up to a 7-fold decrease in Notch activation, and that the effects of both Notch ΔE addition AAK1 knockdown were abrogated in the presence of a γ-secretase inhibitor.[41]

Gupta-Rossi et al. showed that AAK1 interacts with activated ΔE Notch, but not full-length Notch.[41] The authors found that the ankyrin repeats of Notch, spanning residues 1840-2142, and the C-terminus of AAK1, which contains the AP2 binding domain, residues 632 and beyond, are needed for this interaction.[41] The authors also reported that AAK1 preferentially interacts with the monoubiquitinated form of ΔE Notch and that this interaction requires AAK1's kinase activity, as it was not observed with kinase-dead (K74A mutant) AAK1.[41] However, using *in vitro* kinase assays, the authors found that AAK1 does not phosphorylate Notch.[41]

Furthermore, Gupta-Rossi et al. showed that AAK1 stabilizes ΔE, but not full-length, inactive Notch.[41] By performing experiments in the presence of cycloheximide, a protein synthesis inhibitor, the authors observed a notable decrease in Notch ΔE degradation upon AAK1 overexpression and increase in degradation when AAK1 is knocked down.[41] On the other hand, neither AAK1 overexpression or silencing affected the stability of full-length Notch.[41]

The authors also explored the possible connection between AAK1, Notch and Numb. Numb is a known negative regulator of Notch, and as discussed above, AAK1's involvement in Numb signaling has been previously reported.[36, 41] Gupta-Rossi et al. expressed a constitutively active mutant small GTPase Rab5 (Rab5Q79L), which is expected to induce enlarged early endosomes.[41] The authors reported a significant increase in Notch ΔE and Rab5Q79L upon AAK1 overexpression, and the reverse was true when AAK1 was knocked down.[41] On the other hand, Numb overexpression resulted in less colocalization between Notch ΔE and Rab5Q79L.[41] Based on these results, the authors proposed a regulatory mechanism by which AAK1 sorts Notch ΔE towards the endocytic pathway, while Numb drives it towards degradation.[41]

1.5. AAK1 is involved in various biological processes

Viruses often hijack the endocytic machinery to enter cells, and NAKs are known to regulate endocytosis via phosphorylation. Not surprisingly, AAK1 has been linked to various viral infections, including COVID-19, rabies, hepatitis C and dengue.[43-46] Karim et al. reported that both the inhibition and RNAi knockdown of AAK1 and other NAKs, such as BIKE and GAK, reduced SARS-CoV-2 viral entry in Calu-3, a human lung adenocarcinoma cell line.[43] Similarly, Neveu et al. reported that the RNA interference (RNAi) knockdown and inhibition of AAK1 and GAK impaired hepatitis C virus (HCV) assembly and entry into Huh7, a hepatocellular carcinoma cell line.[44] Wang et al. showed that rabies infection requires both AAK1's presence and kinase activity, as both AAK1 RNAi knockdown and inhibition impaired rabies virus entry in HEK293 cells.[45] Tongmuang et al. found that inhibition of AAK1 activity by the tyrosine kinase inhibitor sunitinib resulted in lower production of dengue virus production in Huh7.[46]

In addition to viral entry, AAK1 has also been linked to various neuronal processes in relation to its well-known role in endocytosis. Various studies have reported AAK1's high expression in the nervous system, and AAK1 has been connected to various nervous system disorders, including Alzheimer's, Parkinson, amyotrophic lateral sclerosis (ALS) and neuropathic pain.[47-50] On a molecular level, several studies have identified AAK1 as a substrate nuclear dbf2-related kinase 1/2 (NDR1/2 or STK38) and cyclin-dependent kinase 16 (CDK16 or PCTAIRE-1), which have been implicated in the regulation of synaptic transmission and dendritic branching, respectively.[51, 52] While PCTAIRE-1 is widely expressed and is best known as a mitotic kinase, it is highly expressed in the brain. To characterize the neuronal function of PCTAIRE-1, Shehata et al. performed a chemical genetic approach followed by mass spectrometry (MS) analysis in mouse brain lysates and identified AAK1, along with dynamin and synaptojanin 1, as PCTAIRE-1 substrates.[51] Ultanir et al. found that both RNAi knockdown and inhibition of NDR1/2 resulted in increased dendrite branching, which indicated the kinase's negative regulatory role in this process.[52] Then, using a chemical genetics approach, they identified AAK1 and Rabin8, a guanine nucleotide exchange factor is also known to be involved in vesicle trafficking, as NDR1/2 substrates.[52]

Also in relation to its regulation of endocytosis, AAK1 has been linked to macroautophagy, a recycling process in cells that targets proteins and organelles for degradation as part of an immune response.[53] Specifically, Loi et al. found that AAK1 prevents the degradation and stabilizes the expression of major histocompatibility complex (MHC) class I molecules on the surfaces of cells, enhancing CD8$^+$ T cell responses during influenza A virus (IAV) and lymphocytic choriomeningitis virus (LCMV) infection.[53] Another study further described AAK1's role in immune responses in relation to its regulation of endocytosis; Yuan et al. showed that AAK1 inhibition could prevent the internalization of bacterial lipopolysaccharide (LPS), which can trigger caspase 11-mediated sepsis.[54]

A past study reported that AAK1 was the most frequently mutated gene in mouse models of melanoma, lymphoma and lung carcinoma, and this mutation frequency was increased upon inhibition of the immune checkpoint programmed cell death protein 1 (PD-1).[55] The authors also reported that AAK1 inhibition increased tumor infiltration by CD4$^+$ T cells.[55] Prior to this, AAK1 has been indirectly linked to cancer through the observed antiviral effects of kinase inhibitor drugs used against cancer, such as sunitinib, erlotinib and baricitinib.[56-58] Bioinformatics analyses in multiple studies revealed that AAK1 can be differentially expressed or phosphorylated in various cancers, such as diffuse gastric cancer, diffuse large B-cell lymphoma and lung adenocarcinoma.[59-61] Furthermore, a study reported the presence of an anaplastic lymphoma kinase (ALK)-AAK1 fusion gene using fluorescent in situ hybridization (FISH) experiments on formalin-fixed paraffin embedded tissues from patients with lung adenocarcinoma.[62]

In 2023, our group directly established AAK1's role in cancer EMT in hepatocellular carcinoma (HCC).[63] We showed that AAK1 and its protein-protein interaction (PPI) partners are highly enriched in HCC cell lines with mesenchymal-like phenotypes, such as high migration, slow proliferation and drug resistance.[63] We also found that RNAi knockdown of AAK1 reversed EMT in these cell lines.[63] Recently, another study also reported that AAK1 knockdown reduced proliferation and invasion in ovarian cancer cells and suppressed tumor growth and metastases *in vivo* in a mouse xenograft model.[64]

1.6. Putative novel kinase-independent functions of AAK1

Considering there is little conservation between members of the Ark1/Prk1 protein family outside of the kinase domain, Smythe and Ayscough suggested that C-terminal regions might determine unique functions of each kinase.[24] Tissue-specific splice variants of AAK1 have been reported in the literature. Like other NAKs, these variants share identity in the N-terminal kinase domain and have unique C-terminal ends. Lysates from rat brain, bovine brain and rat liver revealed a single polypeptide migrating at different molecular weights: around 145 kDa in rat and bovine brain and around 100 kDa in rat liver.[22] A later study provided further evidence for the existence of at least two alternatively spliced AAK1 forms: one with 863 amino acids and another with 961.[65]

In this paper, the authors performed a Northern blot using an antisense RNA probe targeting a region that is shared between the two AAK1 isoforms and observed two transcripts at 9 and 5kb.[65] They found that endogenously, AAK1-863 exists at a much lower abundance than AAK1-961.[65] The C-terminus of AAK1-961 contains an additional clathrin-binding domain (CBD2) with several low-affinity binding motifs.[65] Biochemical assays showed that both AAK1-863 and AAK1-961 interact with clathrin and phosphorylate of the μ subunits of AP complexes.[65] However, only the overexpression of CBD2, which is on AAK1-961, but not CBD1, shared between the two isoforms, impairs transferrin uptake.[65]

Recently, Knop et al. described that SEL-5, the AAK1 homolog in *C. elegans*, positively regulates Wnt signaling in a kinase-independent manner.[66] Before this study, AAK1 was previously described as a negative regulator of Wnt signaling.[32, 33] Knop and colleagues showed that SEL-5 phosphorylates DPY-23, the AP2 subunit μ2 (AP2M1) homolog in *C. elegans*, yet it regulates Wnt in the context of neuroblast migration in a kinase-independent manner.[66] The authors found that RNAi knockdown of SEL-5 alone did not affect *C. elegans* neuroblast migration.[66] However, they observed a migration defect when they did this knockdown in a strain lacking VPS-29, part of the endocytosis machinery in *C. elegans* known as the retromer complex.[66] The authors also saw that this defect could be rescued by the expression of kinase-dead SEL-5 (K75A or D178A mutants, corresponding to K74A and D176A mutants in humans).[30, 66] These results suggest the possibility that AAK1 may have previously unexplored roles that are separate from its kinase activity and/or endocytosis.

1.7. UTP25, a nucleolar protein, regulates ribosome biogenesis and p53 stability

The U3 small nucleolar RNA-associated protein 25 homolog (UTP25, also known as digestive expansion factor, or DIEXF/Def) is an understudied nucleolar protein. It was first identified to upregulate an isoform of the p53 tumor suppressor.[67] Utp25p, the protein's homolog in yeast, has been described as an RNA helicase with a DEAD-box motif and is involved in the maturation of ribosome small subunit (SSU) processome.[68-70] Bao et al. showed that in human cells, UTP25's entry into the nucleolus depended on UTP3, another nucleolar protein.[70]

A 2017 study linked UTP25's role in ribosome biogenesis to cancer.[71] The authors found that human neuroblastoma with amplification of the *MYCN* oncogene had significantly higher expression levels of UTP25.[71] They then showed that UTP25 knockdown reduced cell proliferation and increased cell apoptosis in human *MYCN*-amplified neuroblastoma cell lines.[71] On the other hand, a different group of scientists who studied UTP25 following liver hepatectomy in mice found that UTP25 knockdown resulted in an increase of cell proliferation and the proportion of mitotic cells.[72] However, the role of UTP25 on ribosome biogenesis in this model was not directly tested; thus, it is possible that UTP25 could affect liver cell proliferation via a different mechanism. Although neither of these studies have been replicated, they suggest that the roles of UTP25 could be context-, species- and/or organ-specific.

Since the 2005 paper, several other studies have reported the negative regulatory role of UTP25 on p53. Specifically, scientists have described UTP25's involvement in the ubiquitin-proteasome pathway-independent degradation of the well-known tumor suppressor.[73, 74] Although p53 is commonly mutated and Chen et al.'s study first connected UTP25 to an N-terminal truncated isoform of p53, Tao et al. showed that UTP25 knockdown increased p53 protein levels in human cancer cell lines regardless of whether they have wild-type or altered forms of p53.[73]

Tao et al. also found that UTP25 degradation of p53 requires p53's DNA-binding motif and is independent of the mouse double minute 2 (Mdm2), the best-known negative regulator of p53 that acts via the ubiquitin-proteasome pathway.[73] By performing experiments using different protein degradation inhibitors, the authors discovered that UTP25's effect on p53 degradation is mediated by the cysteine protease calpain 3 (CAPN3).[73] In 2016, Guan et al. reported that knockdowns of UTP25 and CAPN3 resulted in cell cycle arrest, which is expected with p53 upregulation.[74] They also found that UTP25 phosphorylation is required for its function in p53 degradation.[74]

1.8 Conclusions

In cancer, EMT has been associated with poor patient outcomes due to therapeutic resistance and metastasis. However, the study of EMT is challenging because the regulation of EMT is context dependent, and EMT often only occurs partially. Both AAK1 and UTP25 have been associated with other proteins and/or pathways that regulate EMT-related cellular processes, such as Wnt and Notch signaling and the tumor suppressor p53, respectively; however, neither was previously linked to EMT directly. Although the phosphorylation of UTP25 was shown to be necessary in its mediating of p53 degradation, UTP25 lacks known NAK phosphorylation motif. This suggests that the relationship between the two proteins may be independent of phosphorylation and/or AAK1's kinase activity.

In the literature, AAK1's best known for its role in mediating CME by phosphorylating AP2M1. AAK1's endocytic function is shared with other members of the NAK family, along with its N-terminal kinase domain and the high degree of sequence homology in this region. This suggests that functions that are unique to AAK1, unrelated to endocytosis, or kinase-independent will likely be encoded by the protein's C-terminus. Two isoforms of AAK1 were previously described. These isoforms are identical in the first 823 amino acids, which include AAK1's kinase and clathrin-binding domain, and are, not surprisingly, comparable in their ability to interact with clathrin and the APs and phosphorylate AP2M1. The two isoforms differ in the last 41 and 139 amino acids, respectively, which further suggests that any unique function will likely be determined by the protein's C-terminal region.

Chapter Two: Multiplexed kinase interactome profiling quantifies cellular network activity and plasticity

Martin Golkowski, Andrea Lius, Tanmay Sapre, Ho-Tak Lau, Taylor Moreno, Dustin J. Maly, Shao-En Ong

Molecular Cell, Volume 83, Issue 5, p803-818.e8, March 02, 2023

2.1 Introduction

Proteins form dynamic protein-protein interaction (PPI) networks that cooperatively carry out their biological functions. PPI network topology is regulated at the level of protein abundance and through signaling events, such as protein post-translational modifications (PTMs), affecting network composition and connectivity.[75, 76] Numerous human diseases alter signaling pathways and protein homeostasis, leading to the rewiring of PPI networks and disease progression.[77-80] The 538 protein kinases in the human kinome are central players in cell signaling, embedded within large PPI networks that respond to physiological and pathological cues.[81-84] Greater understanding of how the kinome integrates with cellular PPI networks can provide insights into physiological processes, identify disease mechanisms, and discover specific kinase complexes that are unique drivers of disease; such complexes may serve as valuable, novel drug targets and biomarkers.[85]

Large-scale maps of PPI networks have been generated with MS-based approaches, such as affinity purification (AP)-MS,[86, 87] and proximity labeling-MS methods, such as BioID[88, 89] and APEX.[90-92] However, AP-MS and proximity labeling-MS lack the necessary throughput and multiplexing capabilities to globally profile PPI network dynamics across many samples and conditions. Furthermore, these methods typically require the expression of epitope-tagged proteins, which can interfere with native cell signaling and is difficult to implement in primary cells and tissues. Size-exclusion chromatography-MS[93] and protein cross-linking-MS[94] allow multiplexed detection of native protein complexes but currently lack the required sensitivity to detect low-abundance PPIs such as kinase-dependent signaling and transcription factor complexes.[91] Sensitive and high-throughput methods are urgently needed to map native kinase PPIs and their dynamic interactomes.

To address this need, we developed kinobead competition and correlation analysis (kiCCA), a MS-based chemoproteomic method for rapid and highly multiplexed profiling of native kinase PPIs in cell and tissue lysates. kiCCA uses a panel of multi-targeted kinase probes to compete kinases and their interaction partners from immobilized kinase inhibitor beads (kinobeads or multiplexed inhibitor beads, MIBs)[95-99] to identify kinase PPIs. We used kiCCA to systematically map kinase interactomes in 18 diverse cancer cell lines and to investigate PPI changes in the context of cancer type, plasticity, and signaling states; this revealed that PPI network topologies are highly dynamic and context dependent. Through our profiling efforts, we identified and quantified 1,154 high-confidence PPIs between 238 kinases and 684 non-kinase proteins, which we compiled into an extensive and easily accessible kinase interactome knowledgebase (https://quantbiology.org/kiCCA).

Using this knowledgebase, we discovered that kinase PPIs can describe kinase functional states and their integration into signaling pathways. We found that cancer cells showing epithelial-mesenchymal plasticity (EMP) and increased therapy resistance[100-102] drastically rewired their kinase PPI networks. Specifically, we found that EMP altered endocytic and vesicle trafficking pathways that are controlled by an adapter-associated kinase 1 (AAK1) interaction network. RNAi-mediated knockdown of AAK1 complex components affected EMP marker expression and greatly sensitized cancer cells to targeted therapy, highlighting that kiCCA can provide actionable leads for drug target discovery. Collectively, our kiCCA method and kinase interactome knowledgebase are invaluable tools for studying kinase PPI networks and can help understand how signaling events influence disease states.

2.2. Results

2.2.1. kiCCA, a method for rapid and highly multiplexed profiling of native kinase interactomes

We and others have shown that kinobeads enrich kinases along with their interactors[95, 99, 103-105]; yet, assigning interactors to specific kinase complexes remained challenging. We demonstrated that selective ATP-competitive kinase inhibitors (KIs) can be used to identify specific kinase interactors by monitoring the co-competition of kinases and non-kinase proteins (Figure 2.1A).[106, 107] We reasoned that if one selective KI displaces a protein complex from the kinobeads, then broadly selective KIs will compete for multiple kinase complexes in a single experiment. By correlating abundances of kinases and their interaction partners across a panel of competition experiments using multiple broad-selectivity KIs with orthogonal kinase binding affinities, hereafter referred to as kinase interactome probes (KIPs), our kiCCA approach would simultaneously identify hundreds of kinobead-bound kinase complexes (Figure 2.1B).

To identify suitable KIPs, we collated kinobead competition data (i.e., MS intensity ratios) from a study profiling targets of 243 Kis[96] and applied pairwise Pearson correlation of MS intensity ratios for all KIs, followed by unsupervised hierarchical clustering of the resulting matrix of *r* values; this identified 12 distinct groups of KIs with orthogonal kinome binding profiles. On average, clusters 1–5, 8–10, and 12 contained more broadly-selective inhibitors compared with clusters 6, 7, and 11. Consequently, we chose one to five KIs from clusters 1–5, 8–10, and 12 to obtain 21 KIPs with broad kinome coverage (Figure 2.2A).

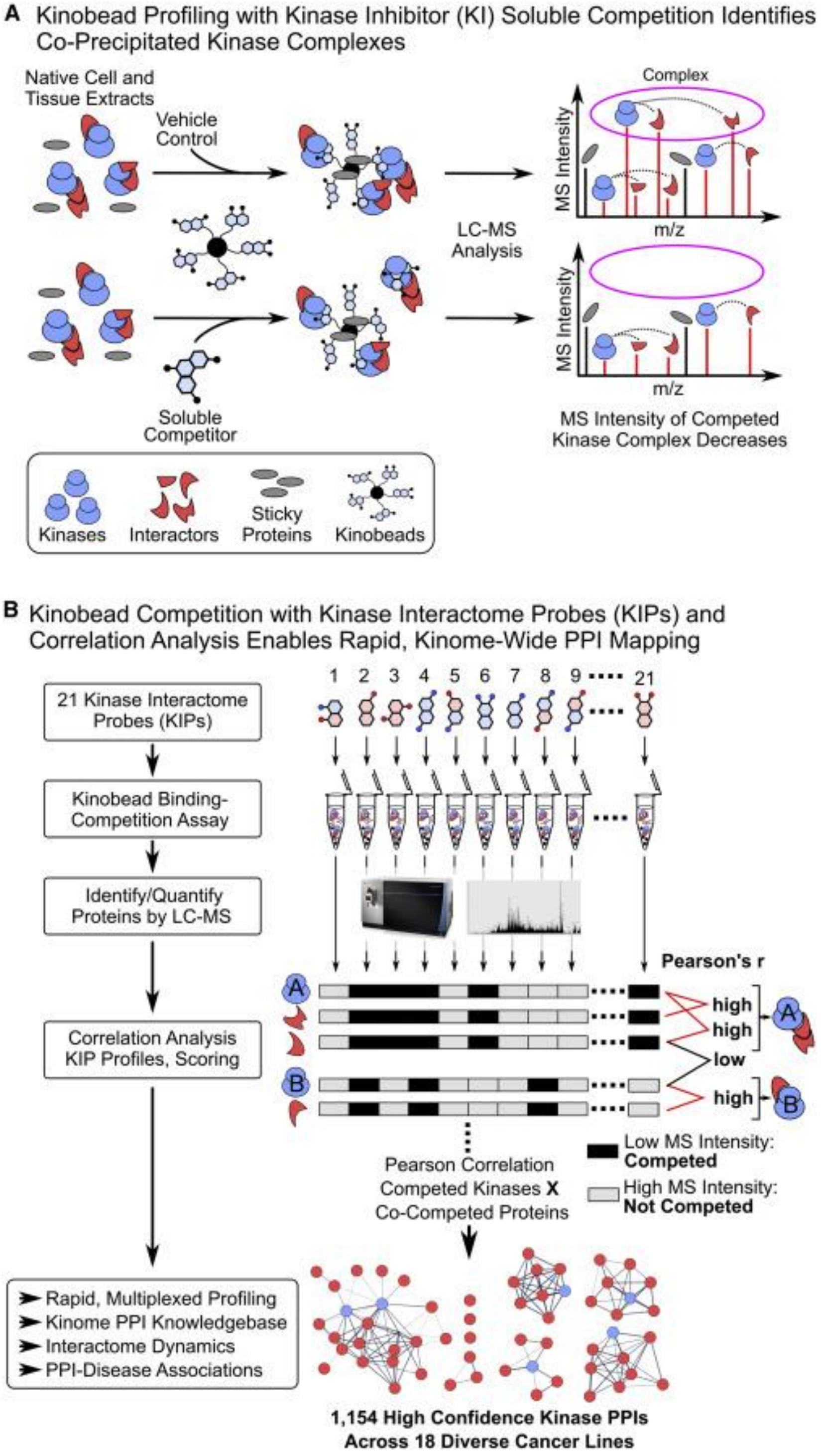

Figure 2.1. Overview of kinobead competition and correlation analysis (kiCCA), a chemoproteomic approach for rapid, sensitive, and highly multiplexed kinase protein-protein interaction (PPI) profiling. (A) Kinome profiling with kinobead/LC-MS and kinase inhibitor (KI) soluble competition identifies co-precipitating kinase complexes. (B) Workflow of our kiCCA

analysis using 21 kinase interactome probes (KIPs) to identify multiple kinase complexes in the same experiment.

To validate that our KIPs compete most expressed kinases, we evaluated their kinome selectivity, each at a single high concentration in HeLa cell lysate (10–50 μM) using our kinobead/LC-MS workflow and label-free quantification.[97, 106] Of the 232 kinases quantified, 199 (86%) were efficiently competed by at least one KIP ($\log_2$ MS Intensity ratio >0.75, two sample t test $p < 0.1$, $n = 2$) and kinase binding profiles of individual KIPs were highly dissimilar (average Pearson's r value = 0.27, Figure S2.1A and S2.1B). Because highly homologous kinases, such as the adenosine monophosphate-activated kinases AMPK1 and 2 (PRKAA1 and 2), showed very similar KIP binding profiles (Pearson's $r \geq 0.9$), we combined these kinases into 54 groups of two to four members, with the other 239 kinase groups comprising one member each (293 kinase groups total, Figure S2.1C). Our results show that by binding and competing kinases of all major families, our 21 KIPs can broadly identify kinase PPIs in kiCCA.

2.2.2. kiCCA accurately and broadly identifies native kinase PPIs

Seeing that our KIPs competed not only kinases but also non-kinase proteins in HeLa cell lysate, we next sought to identify specific kinase PPIs in our HeLa data using correlation analysis (Figure S2.1B). We correlated the MS intensity values of all 199 competed kinases and 573 co-competed non-kinase proteins across the 21 KIP panel and the DMSO control experiment and called the kinase group showing the highest Pearson's r value for each non-kinase protein its most likely interactor. Matching the resulting list of PPIs with the BioGRID protein interaction database v.4.4.200,[109] the BioPlex 3.0 dataset,[87] and the kinome-centric AP-MS dataset from Buljan et al.,[86] we found that 144 of 573 kiCCA interactions had been previously reported, with independent validation for 58 of these. Validated PPIs had highly positive Pearson's r values (median $r = 0.88$, Figure 2.2B), demonstrating that kiCCA can identify known kinase PPIs.

Previously reported but unvalidated kinase PPIs showed a bimodal distribution of *r* values, with many kiCCA interactions showing high *r* values (n = 38, $r > 0.5$). In contrast, unreported kiCCA interactions generally had low *r* values (median $r = 0.43$) although a tail of kiCCA interactions with highly positive *r* values suggested that novel kinase PPIs were identified (Figure 2.2B). Importantly, previously reported and validated interactions were distributed among 37 distinct kinase groups from all kinome sub-families, showing that kiCCA achieves broad and unbiased coverage of kinase PPIs (Figure 2.2C and S2.1D).

To explore kiCCA's ability to identify kinase interactomes across different model systems, we analyzed 17 additional cell lines representing distinct types of cancers, including carcinoma (10 HCC lines), neuroblastoma (SK-N-SH and SH-SY5Y), glioblastoma (A172), osteosarcoma (U2-OS), as well as myeloid malignancies such as chronic myeloid leukemia (K562), mantle cell lymphoma (JeKo1), and T-cell leukemia (Jurkat). Across all 18 lines, our KIPs competed 357 kinases (66% of the human kinome) and 4,136 non-kinase proteins. kiCCA identified 10,791 interactions of these proteins with 294 kinase groups, of which 1,783 PPIs were previously reported.[86, 87, 109] The kiCCA data from our full cell line panel recapitulated our observations in HeLa cell lysates (Figure S2.1E). Comparing the *r*value distributions of reported and unreported interactions from each of the 18 cell lines using Kolmogorov-Smirnov (KS) tests (Figure S2.2), we found that most reported PPIs were identified above a median Pearson's *r* value ≥ 0.594 (Figure 2.2D), and that hundreds of unreported PPIs had *r* values surpassing this threshold (Figure S2.1E). We concluded that an *r* value of >0.6 identifies kinase PPIs, both previously reported and unreported, with high confidence.

Applying our $r > 0.6$ selection rule to our kiCCA dataset of 18 diverse cancer lines, we mapped 1,154 high-confidence kinase PPIs, of which 692 interactions (60%) were not previously reported. Each kinase group interacted on average with six proteins, with the casein kinase 2 group

(CK2 or CSNK2A1, 2, and 3) forming the largest interaction network of 88 members (Figure 2.2E). For proteins interacting with several kinases, we introduced a compound score, hereafter referred to as the kiCCA score, to identify its most likely kinase interactor. This kiCCA score considers both the kiCCA *r* value and the frequency of identification across our 18-cancer line panel and can be used to annotate kinase PPIs in kinobead/LC-MS profiling data. For example, although 14-3-3 binding protein YWHAZ can interact with multiple kinase groups, including the MAP3K2/3 (kiCCA score = 0.21) and the PDPK1/2 group (kiCCA score = 0.08), the higher kiCCA score suggested that the MAP3K2/3-YWHAZ PPI is the more likely interaction.

To experimentally validate the accuracy of kiCCA, we performed co-immunoprecipitation/MS (coIP/MS) experiments in the U2-OS osteosarcoma line using antibodies specific to the catalytic CK2α subunit and the regulatory CK2β subunit, as well as GFP (control). kiCCA identified 31 CK2 interactions in U2-OS cells, and our antibody-based coIP/MS study confirmed 24 (83%) of these interactions (Figures 2.2F and S2.3A). Collectively, these results highlight the high accuracy of kiCCA and its potential to identify cancer cell type-specific kinase PPIs.

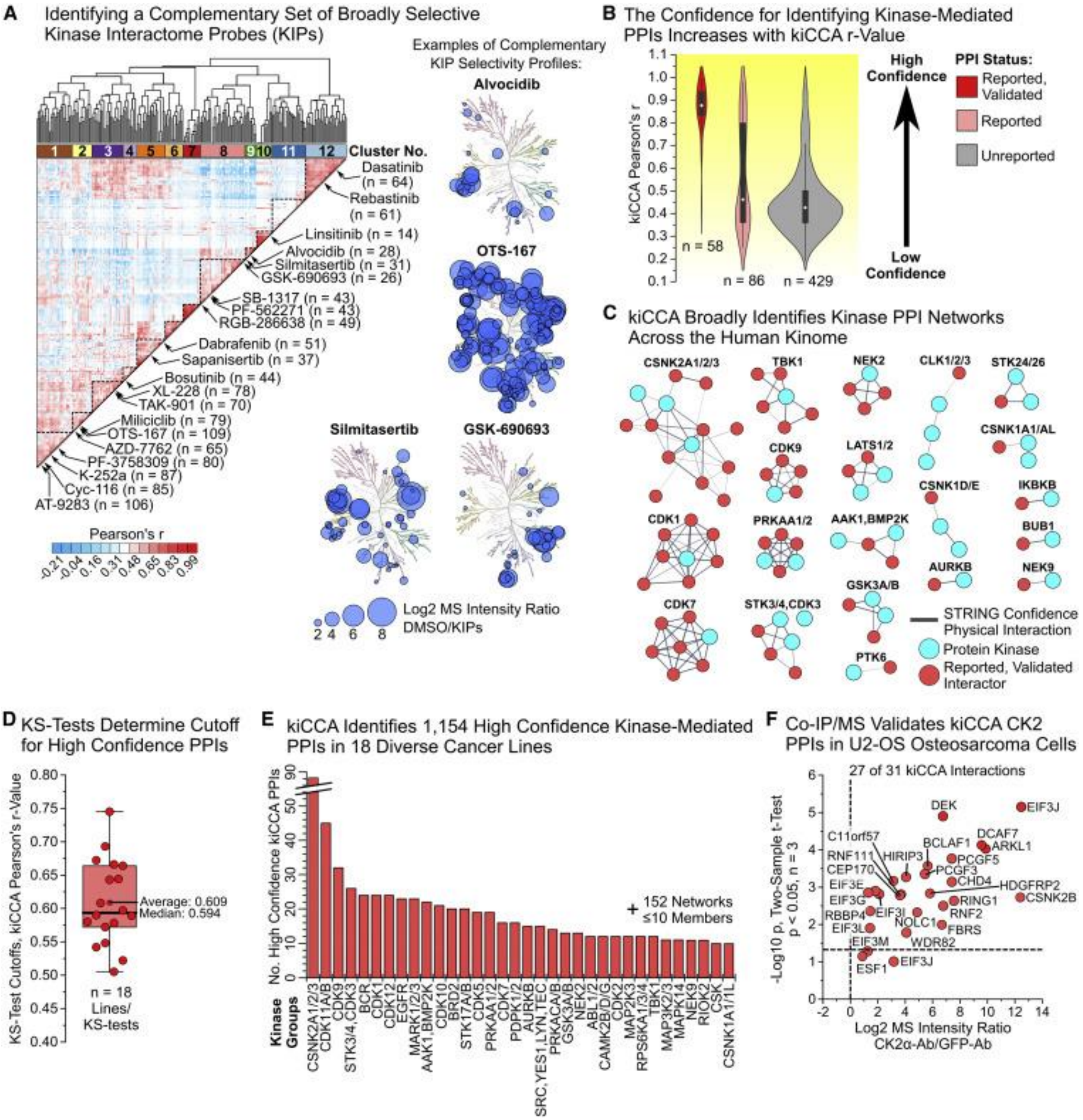

Figure 2.2. Selecting kinase interactome probes (KIPs), proof-of-concept in HeLa lysate, and kiCCA profiling of a diverse 18-cancer line panel. (A) Unsupervised hierarchical clustering of kinase inhibitors (KIs) by their kinome selectivity profiles identifies 21 complementary KIPs. (B) kiCCA accurately identified previously reported PPIs in HeLa cells with high, positive Pearson's *r* values. Violin plot of *r* value distributions for previously reported and independently validated (left), reported but unvalidated (center), and unreported kinase PPIs (right). (C) kiCCA identified kinase PPI networks across the human kinome. Shown are previously reported, independently validated PPI networks of 37 kinase groups identified using kiCCA in unstimulated HeLa cell lysates. Network models created with STRING 11.5.[34] (D) Kolmogorov-Smirnov (KS)

tests of kiCCA data from each of the 18 cancer lines showed that $r > 0.6$ identified most previously reported PPIs. (E) kiCCA in 18 diverse cancer cell lines identified 1,154 high-confidence kinase interactions between 684 proteins and 238 kinase groups. (F) Co-immunoprecipitation/MS (coIP/MS) experiments with casein kinase 2 catalytic and regulatory subunits (CK2α and β) antibodies validated a CK2 PPI network identified by kiCCA in U2-OS cells (two sample t test, $p < 0.05$, $n = 3$), demonstrating kiCCA's high accuracy.

2.2.3. kiCCA quantifies kinase interactome changes linked to cancer cell plasticity

Cancer cells dramatically rewire signaling pathways in response to drugs and changing conditions in the tumor microenvironment, resulting in cellular plasticity that promotes therapy escape and metastasis.[98, 100, 102] To explore if kiCCA can quantify differences in kinase interactomes associated with pathway rewiring and plasticity, we compared the abundances of high-confidence kiCCA PPIs between related cell lines with distinct phenotypic marker gene expression (Figure S2.3B). From our 18-cell line panel, we chose the neuroblastoma line SK-N-SH and its subclone SH-SY5Y as models of cancer cell plasticity. Previous reports showed that the parental SK-N-SH line has mesenchymal stem cell-like characteristics, whereas SH-SY5Y exhibits a noradrenergic neuronal phenotype, suggesting the noradrenergic-mesenchymal plasticity (NMP) of these lines (Figure 2.3A).[110, 111] Our own analysis of mRNA expression data from the Cancer Cell Line Encyclopedia (CCLE)[112] confirmed high expression of mesenchymal and low expression of noradrenergic neuronal markers in SK-N-SH compared with SH-SY5Y cells (Figures S2.3B and S2.3C). Furthermore, our differential expression analysis (DEA) of kinases confirmed that SK-N-SH cells express a kinome profile typical for mesenchymal-like cancer cells, including high expression of the receptor tyrosine kinase UFO (AXL) and the transforming growth factor β receptor TGFBR2,[105] whereas SH-SY5Y cells show high expression of neuronal-specific kinases, such as the anaplastic lymphoma kinase ALK and the β-adrenergic receptor kinase ADRBK2 (Figure 2.3A, Student's t test, Benjamini-Hochberg (BH)-FDR < 0.05, $n = 22$).

Together, these results suggested that neuroblastoma line NMP is associated with widespread changes in kinase expression and a rewiring of kinome-dependent signaling networks.

To clarify if kinome rewiring was accompanied by kinase interactome changes, we next subjected high- confidence kiCCA PPIs in the two neuroblastoma lines to DEA. We discovered that NMP affected interactions between 44 kinase groups and 90 proteins (Figures 2.3B and S2.4), indicating that neuroblastoma cell plasticity caused widespread changes in PPI network topology. The largest rearrangements affected CK2, myosin light-chain kinase (MYLK), and cyclin-dependent kinase (CDK) networks. Unlike alterations in kinase abundance, changes in interactor abundance only weakly correlated with changes in mRNA expression between the two lines (CCLE data, $R^2 = 0.18$, Figure S2.5A), suggesting that changes in kinase PPI networks were caused by post-translational events. For instance, 20 CK2 interactors significantly differed in abundance, half of them showing higher expression in SK-N-SH than SH-SY5Y cells, and vice versa, suggesting that CK2 integrated with distinct pathways in a NMP-dependent manner (Figure 2.3C). Pathway enrichment analysis using STRING 11.5[108] showed that CK2 preferentially integrated into Polycomb repressive complex (PRC1)-like chromatin remodeling complexes in noradrenergic SH-SY5Y cells, whereas it bound more to components of the eukaryotic translation initiation factor 3 (eIF-3) complex in SK-N-SH cells. Notably, the PRC1-like complex also contained the autism susceptibility candidate AUTS2 that together with CK2 has been shown to alleviate transcriptional repression and promote expression of neuronal genes, suggesting that CK2 promotes the neuroblastoma cell NMP program.[113] To validate that kiCCA accurately quantified CK2 interactome rewiring and pathway integration, we used CK2α- and CK2β-targeted antibodies and coIP/MS to quantify abundance changes in CK2 interaction partners between SK-N-SH and SH-SY5Y cells (Figure 3.3D). This analysis showed that 15 CK2 interactions significantly differed in abundance in both kiCCA and coIP/MS, including the NMP-associated CK2-AUTS2 interaction, and that MS intensity ratios between the two analyses were tightly correlated (Pearson's $r = 0.74$). Together, our results showed that kiCCA accurately quantifies plasticity-associated changes in kinase interactomes and their involvement in specific cellular pathways, and that CK2 can switch roles between regulating chromatin structure and translation in neuroblastoma cell NMP.

2.2.4. kiCCA quantifies dynamic changes in kinase interactomes induced by acute signaling events

We next asked if kiCCA can also quantify rapid and transient changes in kinase PPI networks caused by acute signaling events, such as growth factor stimulation. We stimulated HeLa cells with 50 ng/mL epidermal growth factor (EGF) for 15 min, analyzed cell lysates with kiCCA, and identified 163 high-confidence kinase PPIs. To learn which of these PPIs were EGF responsive, we performed DEA of our kiCCA data from unstimulated and EGF-stimulated HeLa cells, identifying 57 high-confidence interactions of 33 kinase groups that significantly changed in abundance (Student's t test, BH-FDR < 0.05, $n = 22$, Figures 2.3E and S2.5B). Members of the EGFR interactome including the signaling adapters GRB2 and SHC1, and the E3 ubiquitin ligases CBL and CBLB, increased in abundance up to ~110-fold (Figures 2.3E, 2.3F, and S2.5B). These results suggested that kiCCA can map acute changes in kinase PPI networks; yet, the overall number of EGF-sensitive PPIs appeared low given that EGFR signaling can affect the phosphorylation states of at least 120 other kinases.[106, 114]

Reasoning that kiCCA, similar to other AP-MS approaches, may miss transient and low affinity PPIs, we repeated the experiment using formaldehyde-mediated protein cross-linking to stabilize kinase signaling complexes. kiCCA with protein cross-linking identified 127 EGF-responsive high- confidence PPIs involving 32 additional kinase groups, more than doubling our coverage of EGF-responsive kinase interactions (Figures 2.3E and S2.5B). These PPIs included additional EGFR interactions, e.g., with the GTP-activating proteins SOS1 and VAV3, and the phosphatidylinositol 3-kinase regulatory subunit PIK3R2, as well as PPIs of several other kinases in the EGFR pathway, including mitogen-activated protein kinases (MAPKs) and the ribosomal S6 kinases (Figures 2.3E, 3F, and S2.5B). These results indicated that cross-linking greatly expands kiCCA's ability to detect transient and weak kinase PPIs. To see if kinase interactome changes were indeed tied to phosphorylation changes triggered by EGFR signaling, we compared kinases with PPI abundance changes to kinases that we previously found differentially phosphorylated upon EGF treatment.[106] This revealed co-regulation of PPI and phosphorylation changes in 44 of 65 kinase groups (Figure 2.3E, hypergeometric test, $p = 1.8E{-}6$), confirming that PPI rewiring was signal-dependent and validating kiCCA's accuracy for quantifying acute kinase interactome changes.

2.2.5. kiCCA PPIs are indicators of kinase functional states and pathway integration

We next asked if changes in kinase interactomes could indicate kinases in distinct functional states. Kinase phosphorylation sites with known regulatory roles[115] were associated with kiCCA PPIs known to affect kinase function; for example, tyrosine phosphorylation of the EGFR recruited its known signaling partners to activate ERK and PI3K-AKT signaling, T-loop S164 and T170 phosphorylation and activation of CDK7 correlated with recruited components of the CDK activating kinase complex, and activating T390 phosphorylation of GSK3B coincided with binding of AXIN1 and the β-catenin destruction complex; in contrast, inhibitory phosphorylation of S9 on GSK3B was accompanied by binding of its inhibitor GSKIP (Figure 2.3F); this confirms that kiCCA PPIs can serve as proxies for phosphorylation events that affect kinase functional states. We also observed changes in PPIs for kinases that are not regulated by phosphorylation, but rather by binding to second messengers or regulatory subunits, such as cAMP-activated protein kinase A (PKA) that bound more of its regulatory subunit following EGF treatment, indicating inactivation.

PKA also switched interactions between the A-kinase anchoring proteins AKAP9 and AKAP7 and AKAP11, indicating cellular re-localization. Similarly, the NF-κB activating kinase B (TBK1) dissociated from the signaling scaffold TANK, marking inactivation (Figure 2.3F). kiCCA PPIs are, therefore, also proxies for phosphorylation-independent signaling events affecting kinase activity and subcellular localization. Searching the 1,154 high-confidence kiCCA PPIs from our interactome knowledgebase in the BioGRID[109] and UniProt[116] databases and associated primary literature, we identified 140 interactions of 85 diverse kinase groups that can affect kinase activation state and/or cellular localization; we hereafter refer to these as functional marker PPIs (fmPPIs) (Figure S2.6A).

Next, to explore if kiCCA PPIs can also indicate the activity of specific cellular pathways, we studied the pathway membership of high-confidence PPIs in our EGF-activated HeLa dataset. Analyzing EGF-sensitive kinase PPIs with STRING pathway enrichment analysis,[108] we found, in addition to the expected EGFR signaling complex, many kinase interactors participating in cellular processes and pathways distinct from canonical EGFR signaling, including G-protein coupled receptor (GPCR)/cAMP signaling, WNT/β-catenin signaling, NF-κB signaling, the cell cycle, and autophagy (Figure 2.3F). Encouraged by these results, we mapped high-confidence kiCCA interactors from our knowledgebase to 32 distinct, disease-relevant signaling pathways and cellular processes using gene ontology – biological process (GOBP) terms (Figure S2.6B). Hypothesizing that an interaction of a kinase with a specific non-kinase pathway member integrates the kinase into the corresponding pathway, we mapped 492 (72%) of kiCCA interactors, and the 169 kinase groups that interact with them, to at least one pathway or process term. Each of the 32 GO terms comprised on average 35 non-kinase interactors, representing an extensive resource for kinase pathway integration (Figure S2.6B). Collectively, using fmPPIs and GOBP term mapping, our kiCCA knowledgebase determined kinase functional states and integrated kinases into cellular pathways through specific PPIs.

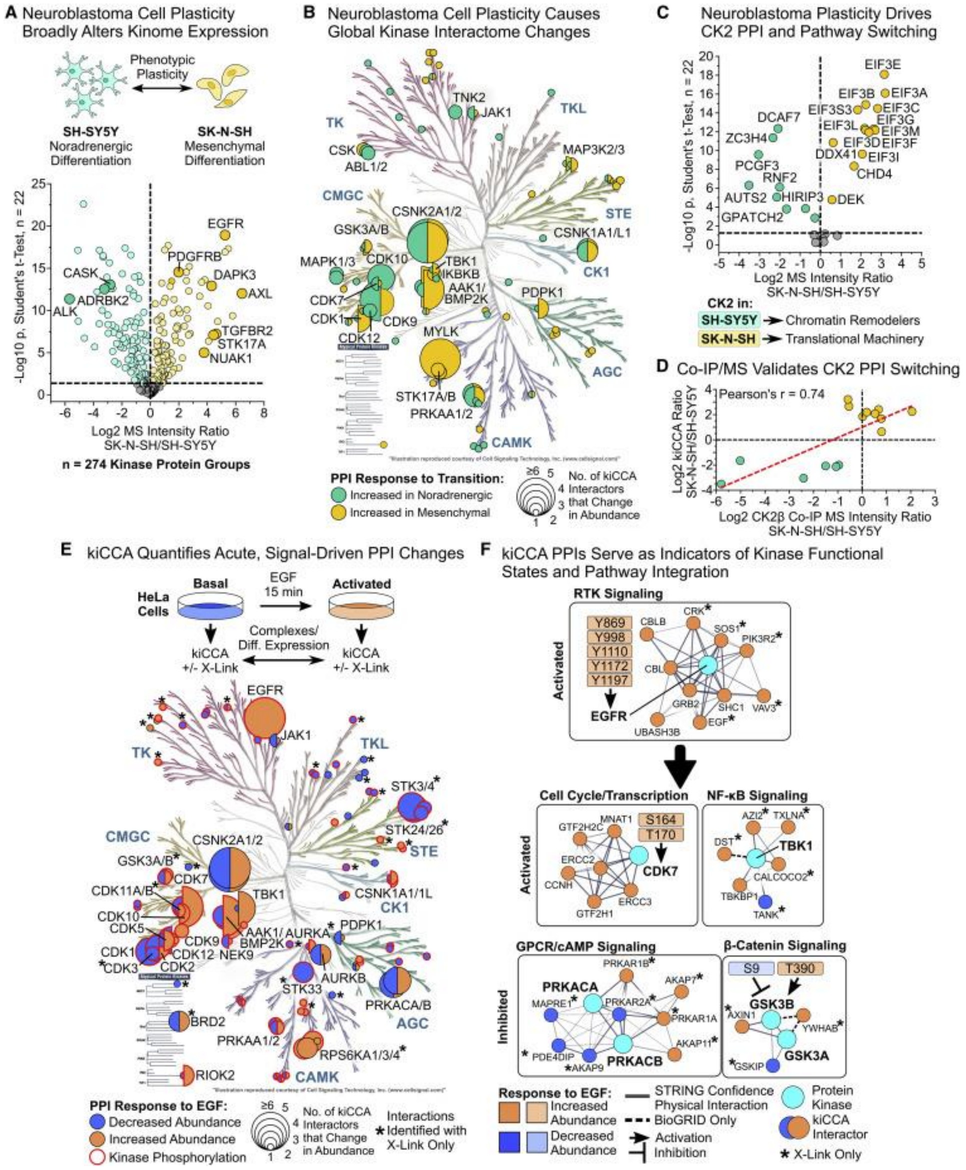

Figure 2.3. kiCCA quantifies kinome interactome changes caused by cancer cell plasticity and acute signaling events. (A) Differential expression analysis (DEA) of kiCCA data revealed that the neuroblastoma lines SK-N-SH and SH-SY5Y have kinome profiles indicative of mesenchymal-noradrenergic plasticity (NMP, Student's t test, Benjamini-Hochberg (BH)-FDR < 0.05, n = 22). Kinases marking the noradrenergic and mesenchymal phenotype are highlighted. (B) Kinases with altered PPI abundance between the SK-N-SH and SH-SY5Y neuroblastoma lines (n = 44 kinase groups, DEA statistics see A). Circle size scales with the number of kinase-binding partners that change in abundance. (C) DEA of high-confidence kiCCA interactions reveals that 20 members of a CK2 interaction network showed an altered abundance between neuroblastoma lines (statistics see A). Pathway enrichment analysis with STRING

11.5[108] showed that differentially abundant CK2 interactors in either cell line participated in distinct signaling pathways. (D) CoIP/MS experiments in the SK-N-SH and SH-SY5Y neuroblastoma lines using specific CK2α/β antibodies confirmed altered abundance of CK2 interaction partners as determined by kiCCA. (E) Overview of kiCCA of EGF-stimulated HeLa cells and annotated kinases with altered PPI abundance upon EGF treatment ($n = 63$ kinase groups, for DEA statistics see A). Kinases with co-regulated changes in phosphorylation and PPIs are highlighted in red. Kinases marked with an asterisk (*) have PPI changes only detected with protein cross-linking. (F) kiCCA of EGF-stimulated HeLa cells revealed that abundance changes of PPIs correlated with changes in kinase functional states, connecting the EGFR to several non-canonical EGFR-signaling pathways. Network models were created using STRING 11.5.[108] See also Figure S2.4.

2.2.6. kiCCA identifies kinase functional states and pathways underlying hepatocellular carcinoma therapy resistance

Hepatocellular carcinoma (HCC) is the most common form of primary liver cancer and the second most deadly malignancy worldwide.[117] HCCs are highly resistant to therapy, which is in part caused by cancer cell EMP.[105, 118] We previously showed that ~50% HCC CCLE cell lines are resistant to KIs of clinically relevant HCC targets such as cell cycle kinases, PI3K/mammalian target of rapamycin (mTOR), and fibroblast growth factor receptors (FGFRs), and that resistance was tightly linked to EMP.[105] To demonstrate the utility of kiCCA in identifying disease mechanisms and drug targets, and to understand how HCC cell EMP rewires the kinome to promote therapy resistance, we compared kiCCA data from the archetypical epithelial-like and drug-sensitive HuH-7 line to the mesenchymal-like and drug-resistant SNU761 line (Figures 2.4A and S2.3B). Applying DEA to the kinases quantified in the two HCC lines, we discovered that 170 kinases significantly differed in abundance (Student’s t test, BH-FDR < 0.05, $n = 22$) and that the changes in the kinome showed a profile typical for HCC cell EMP, including ~1,200-fold increased abundance of AXL in SNU761 cells and increased expression of FGFR isoforms 2, 3, and 4, and various polarity and cell cycle-related kinases in HuH-7 cells (Figure 2.4A). DEA of the 227 high-confidence kiCCA PPIs identified in the two HCC lines showed that 127 PPIs significantly differed in abundance. Similar to our analysis of neuroblastoma lines (Figures 2.3B and S2.5A), abundance changes of kiCCA interactors correlated poorly with CCLE mRNA expression differences, whereas kinase abundance changes were better correlated (Figure S2.6C), suggesting that EMP-associated kinome rewiring was driven by post-translational events. Mapped fmPPIs in the mesenchymal-like SNU761 line indicated elevated activation of the survival-promoting tyrosine kinases SRC, EGFR, and ACK1 (TNK2), the WNT pathway kinases GSK3A and B, and the NF-κB-activating kinase CHUK. Surprisingly, SNU761 cells also showed elevated activation of numerous proliferation suppressor kinases, including the Hippo kinases STK3 and 4 (MST1 and 2) and STK38 (NDR1), and the liver kinase B1 (LKB1 or STK11, Figure 2.4B). These results suggest that mesenchymal-like HCC cells evade therapies by simultaneously activating kinases that promote survival along with kinases that blunt proliferation and the cell cycle, thereby evading drugs that preferentially kill rapidly proliferating cells.

Next, to systematically understand how EMP affects kinase-mediated pathways, we analyzed GOBP terms for kiCCA PPIs differing in abundance between the HuH7 and SNU761 lines (Figure S2.6D). Translation and chromatin remodeling pathways related to cell proliferation were enriched in HuH-7 cells, with mainly CK2 integrating into these pathways. In contrast, SNU761 cells were enriched in endocytosis and vesicle trafficking pathways involving the adapter-associated kinase 1 (AAK1) and the BMP-2-inducible protein kinase (BMP2K), as well as developmental pathways, such as GSK3A and B inactivation-driven canonical WNT/β-catenin signaling, and EGFR and SRC signaling (Figures 2.4C and S2.6D). To validate these findings, we applied gene set enrichment analysis (GSEA) with GOBP terms[119, 120] to our kiCCA data from the HuH7 and SNU761 lines, and our published kinobead/LC-MS profiling data from seven epithelial-like and ten mesenchymal-like HCC lines (Figure S2.6E). We confirmed that endocytosis, vesicle trafficking, survival, and EMP-related pathways were highly enriched in mesenchymal-like HCC cells. Components of the endocytosis and vesicle trafficking machinery have been previously linked to HCC progression[121, 122] and to cancer cell EMP in pancreatic ductal adenocarcinoma cells,[123-125] but whether aberrant endocytosis and vesicle trafficking promotes HCC cell EMP remains unclear. Hypothesizing that dysregulated AAK1/BMP2K interaction networks can promote cancer cell plasticity, we examined abundance changes of AAK1/BMP2K PPIs (Figure 2.4D) in our kiCCA data from HuH-7 and SNU761 HCC models, SK-N-SH and SH-SY5Y models, and our 17 HCC cell line panel.[105] Abundance of the Ral GTPase effectors and endocytic adapters RalBP1-associated Eps domain-containing protein 1 and 2 (REPS1 and 2) were consistently increased in mesenchymal-like cells (up to 16-fold, Figure 2.4E) and the scaffolding protein and known REPS1 and 2 interactor RalA-binding protein 1 (RALBP1, Figure 2.4D) also showed increased abundance in mesenchymal-like cells, albeit with lower ratios (Figure 2.4E), suggesting that the AAK1/BMP2K interaction network may be important for acquiring plasticity.

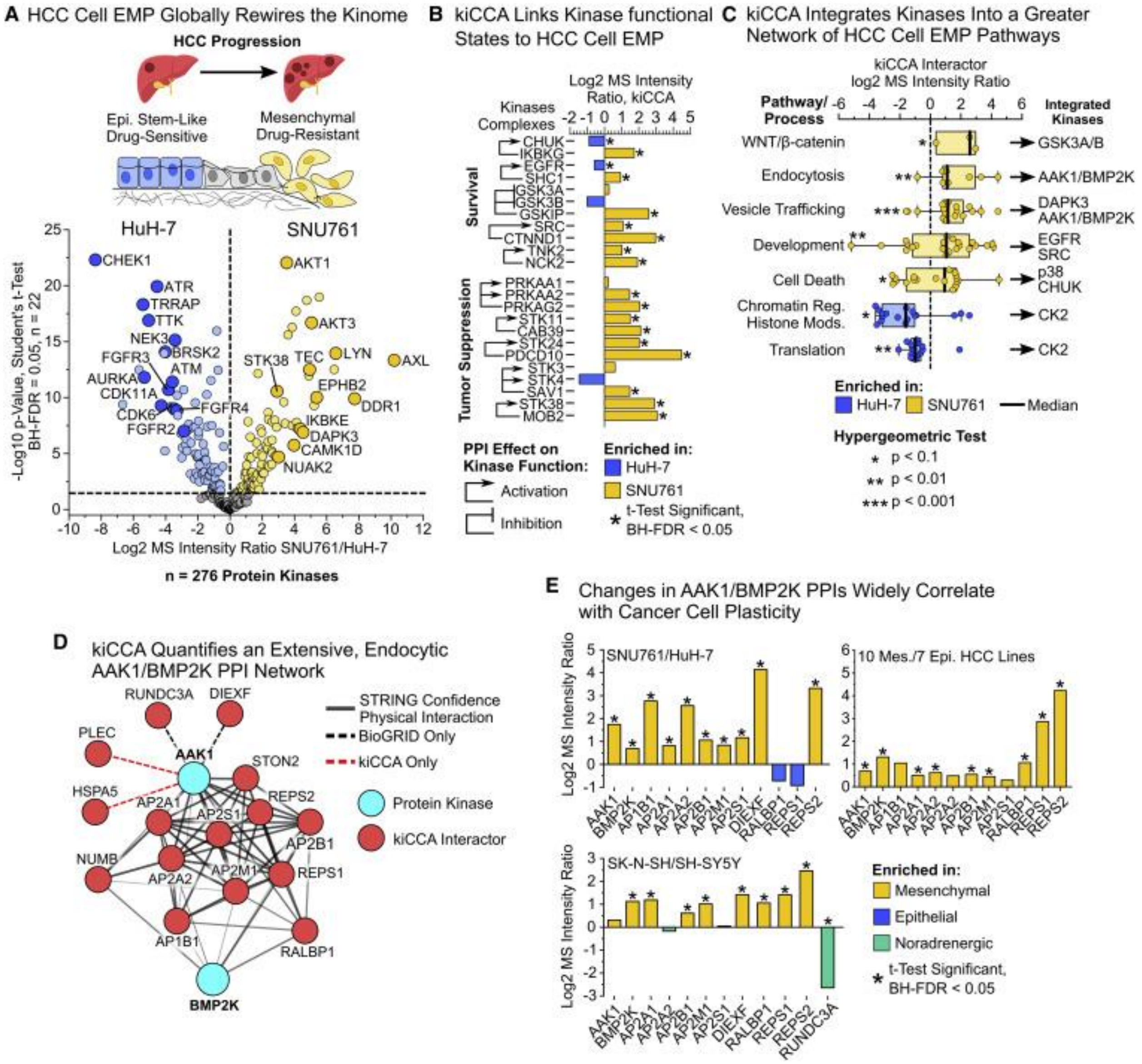

Figure 2.4. kiCCA analysis of hepatocellular carcinoma (HCC) lines identifies changes in kinase functional states and pathways correlating with plasticity and drug resistance. (A) Epithelial-mesenchymal plasticity (EMP) promotes HCC progression, metastatic spread, and therapy resistance. kiCCA DEA data revealed extensive kinome expression changes between epithelial-like HuH-7 cells and mesenchymal-like SNU761 cells in HCC cell EMP (Student's t test, BH-FDR < 0.05, n = 22). (B) kiCCA and DEA analysis of the HCC cell EMP models SNU761 and HuH-7 mapped 127 kinase PPIs that significantly differed in abundance. Cross-referencing our curated set of fmPPIs revealed that kinases involved in cell survival and proliferation suppression are broadly activated in the mesenchymal-like SNU761 line (for DEA statistics see A). (C) Gene ontology-biological process (GOBP) term analysis of kiCCA interactors identifies cellular pathways and processes associated with HCC cell EMP, integrating specific kinases into EMP pathways through their PPIs. GOBP term enrichment was determined by

hypergeometric test ($p < 0.1$). (D) kiCCA quantifies an extensive AAK1/BMP2K interaction network involved in endocytosis and vesicle trafficking across the 18-cancer cell line panel (Created using STRING 11.5[108]). (E) Members of the AAK1/BMP2K PPI network were broadly associated with cancer cell plasticity in the SNU761 and HuH-7 HCC lines and SK-N-SH and SH-SY5Y neuroblastoma lines (for DEA statistics see A), and in the larger 17-member HCC line panel (two sample t test mesenchymal vs. epithelial, BH-FDR < 0.05).[105]

2.2.7. An endocytic AAK1 interaction network promotes HCC cell EMP and therapy resistance

We next sought to clarify if the AAK1/BMP2K PPI network can drive HCC cell EMP and therapy resistance or merely acts as a bystander. AAK1 has been shown to function in clathrin-mediated endocytosis[22] and canonical Notch and Wnt signaling that can both contribute to cancer cell EMP,[33, 41] whereas the function of BMP2K is poorly understood. REPS1 and 2 regulate receptor tyrosine kinase endocytosis and recycling downstream of Ras-related proteins RALA and B,[126] cell migration, and NF-κB pathway activation.[127, 128] Likewise, RALBP1 acts in RALA- and B-mediated receptor endocytosis and serves as a GTPase activating protein (GAP) for CDC42 and RAC.[129, 130] First, to see if RALBP1, REPS1 and 2 interact with AAK1 or BMP2K, we performed a kinobead soluble competition experiment in FOCUS cell lysate using the selective AAK1 inhibitor LP-935509 (Figure 2.5A),[50] revealing that REPS1 and 2, RALBP1, and the four subunits of the adapter protein 2 (AP-2) complex were selectively competed along with AAK1; this was concordant with our kiCCA results from CYC116 competition in FOCUS cell lysates (Figure S2.7A) and strongly suggested that REPS1 and 2, and RALBP1 interacted with AAK1 rather than BMP2K. We further validated these results by coIP/MS using antibodies specific to AAK1, RALBP1, and REPS1 in FOCUS cell lysate (Figure S2.7B), establishing AAK1 as the central kinase of the PPI network.

To test if AAK1 network components promote HCC cell EMP and drug resistance, we stably expressed shRNAs targeting *AAK1*, *RALBP1*, *REPS1*, and *REPS2* or a scrambled sequence in the mesenchymal-like FOCUS, SKHep1, SNU761, and SNU387 cell lines. By quantitative real-time PCR and immunoblotting, we consistently achieved near-complete knockdown of *RALBP1*, *REPS1*, and *REPS2* and reduced *AAK1* expression by 2- to 4-fold (Figures S2.8A and S2.8B). Immunoblot analysis of different EMP markers in our RNAi lines showed reduced expression of the central EMP transcription factor ZEB1 in FOCUS, SNU387, and SNU761 cells and revealed that RNAi also affected the expression of AXL, CD44, E-cadherin CDH1, and the transcriptional repressor Snail (SNAI1), albeit in a cell line-dependent manner (Figures 2.5B and S2.9); this suggested that the AAK1 complex can indeed promote EMP. Hypothesizing that the AAK1 network's function in EMP may be linked to its role in kinase receptor endocytosis and recycling, we profiled the kinome of RNAi lines using kinobead/LC-MS. In addition to validating successful knockdown of AAK1 PPI network components (Figure S2.10A), this revealed that the known EMP driver kinases AXL and TGFBR2, as well as the EGFR, the ephrin receptor A2 (EPHA2), and five additional members of the TGFβ receptor superfamily were consistently downregulated across three of the four HCC lines tested (Figure 2.5C). Applying GSEA to our kinobead profiling data confirmed that AAK1 complex RNAi causes the downregulation of endocytosis-related pathways, HCC cell EMP-related pathways, like cell adhesion and WNT signaling, and survival signaling through protein kinase B and the mTOR (Figure S2.10B). In contrast, pathways related to insulin signaling, chromatin remodeling, and the cell cycle increased in response to RNAi, confirming transition to a more epithelial, hepatocyte-like state. Together, these results suggested that the AAK1-RALBP1-REPS1/2 network can promote HCC cell EMP and drug resistance by stabilizing specific kinase receptors that drive developmental and survival signaling.

To learn if the AAK1 complex could serve as a target to sensitize HCC cells to drug treatment, we conducted a screen for cell viability using ten kinase-targeted drugs and doxorubicin in scramble control vs. AAK1 complex RNAi lines (Figure 2.5D). RNAi lines, particularly

SNU387 and SKHep1, showed up to 18-fold down-shifts in EC_{50}s for inhibitors targeting the cell cycle checkpoint kinases CHEK1 (AZD7762 and CHIR-124), inhibitors that we found previously to be highly effective in killing rapidly proliferating, epithelial-like HCC cells compared with mesenchymal-like cells.[105] To identify pathways mediating the RNAi-dependent increase in drug efficacy, we revisited our kinome profiling data of the most chemosensitized lines, SKHep1 and SNU387 (Figure 2.5E). Cross-referencing fmPPIs in our interactome knowledgebase revealed that these cell lines activated cell cycle-related kinases and their signaling complexes specifically in response to *AAK1* and *REPS1* RNAi, which coincided with the greatest sensitization to CHEK1 inhibitors (Figure 2.5E). This also agreed with our GSEA of knockdown lines, as pathways related to cell cycle progression and DNA repair were upregulated with RNAi of the AAK1 network (Figure S2.10B). Likewise, immunoblot analysis validated that AAK1 and REPS1 RNAi increased the expression of cell cycle-driving proteins (Figures 2.5F and S2.11). These results indicated (1) that AAK1 and REPS1 act as proliferation suppressors in mesenchymal-like HCC cells,[131] and (2) that *AAK1* and *REPS1* RNAi-mediated activation of proliferation exposes a vulnerability of drug resistant HCC cells that can be targeted with cell cycle checkpoint KIs.

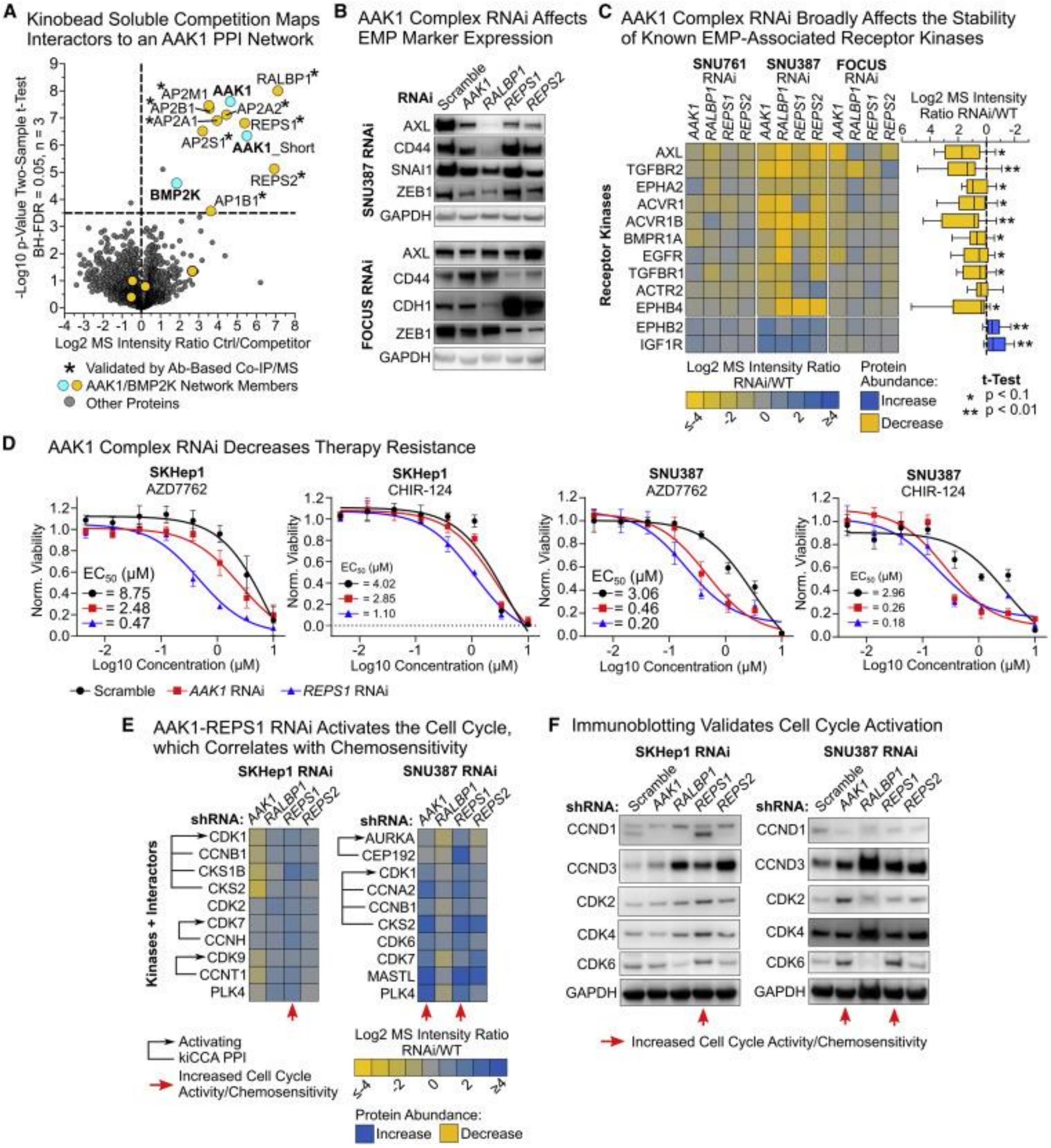

Figure 2.5. An AAK1 interaction network promotes EMP and therapy resistance in HCC and exhibits characteristics of a proliferation suppressor. (A) Kinobead/LC-MS soluble competition experiments using 1 μM of the selective AAK1 inhibitor LP-935509 show that the PPI network is centered on AAK1, not BMP2K. (B) Immunoblotting of EMP markers in SNU387 and FOCUS AAK1 network RNAi lines indicated alterations in EMP state. (C) Heatmap showing EMP-associated receptor kinases that change in abundance in response to AAK1 PPI network RNAi in mesenchymal-like HCC cells. Kinase abundance differences were determined by kinobead/LC-MS

profiling. (D) Drug screen results demonstrating that AAK1 network RNAi lines are up to 18-fold more sensitive to the cell cycle checkpoint kinase (CHEK1) inhibitors AZD-7762 and CHIR-124. (E) Kinobead/LC-MS profiling of SKHep1 and SNU387 lines shows that AAK1 and REPS1 RNAi causes upregulation of cell cycle-related kinases and their activating PPIs specifically in lines with increased sensitivity to CHEK1 inhibitors. (F) Immunoblotting confirmed activation of the cell cycle specifically in AAK1 and REPS1 RNAi lines, suggesting that they act as proliferation suppressors in mesenchymal-like cells. See also Figure S2.9.

2.2.8. Systematic mapping of kinase PPIs in kinome profiling data from clinical tissue specimens

Mapping disease-associated interactome changes in pre-clinical animal models and clinical tissue specimens is a critical milestone in translating PPI network information into biomarkers and drug targets. Studies using kinobead/LC-MS profiling to characterize kinome aberrations in pre-clinical and clinical tissue specimens have transformed our understanding of disease mechanisms (Figure 2.6A)[98, 105, 132-134]; these studies contain valuable kinase interactome data that could greatly expand our understanding of *in vivo* disease biology; yet, computational approaches to accurately interpret this information are lacking.

To explore if our kiCCA interactome data can identify kinome PPIs in kinobead profiling data from clinical tissue specimens, we mapped high-confidence interactions in our knowledgebase to our previously published kinobead profiling dataset of four paired, clinical HCC and non-tumor liver (NTL) tissue samples (Figure 2.6A)[105] and identified the interactions between 133 kinase groups and 275 non-kinase proteins. Because the kiCCA knowledgebase aggregates kinome PPI information across a range of biological contexts and some proteins may have been observed to interact with more than one kinase, we applied our kiCCA score that considers both the kiCCA R value and the frequency of identification across our 18-cancer line panel, to determine the 275 most likely kinase PPIs; 199 of these interactions integrated 75 kinase groups into specific signaling pathways, and 39 fmPPIs specified the functional states of 24 kinase groups (Figures 2.6B and 2.6C).

DEA between tumors and paired NTL tissues showed that 189 of these PPIs showed altered abundance, including several functional PPIs affecting kinases with important roles in HCC progression. For example, we found that the activating CDK12-CCNK interaction[135] and the paxillin (PXN)-PTK2B interaction that directs kinase activity to focal adhesions were upregulated in all four tumor samples compared with NTL,[136] whereas the activating interactions of AMPK (PRKAA1 and 2) with its regulatory subunits were consistently downregulated in all tumors.[137] This provides evidence for the broad relevance of CDK12 activity and focal adhesion signaling in HCC progression, and AMPK's tumor suppressor function in HCC. We also identified functional PPIs specific to individual HCC cases; for instance, activating PPIs of the cell cycle kinases CDK1 and 7, and aurora kinase B (AURKB), and the NF-κB kinase TBK1 were enriched in tumor #4, inhibitory interactions of the WNT/β-catenin kinases GSK3A and B were enriched in tumor #3, and the activating interaction of the EMP and survival kinase AXL and GAS6 was specifically enriched in tumor #2 (Figure 2.6B). These results show that our interactome knowledgebase and kiCCA scoring can identify kinase activities in individual patient's tumors, highlighting kiCCA's utility for precision oncology.

To uncover *in vivo* mechanisms controlling HCC progression, we analyzed the pathways associated with differentially expressed kinase PPIs. This confirmed activation of the cell cycle in tumor #4, and upregulation of protein translation, developmental pathways, and apoptosis in most tumor samples compared with NTL tissue (Figure 2.6C), consistent with a cycle of proliferation and apoptosis in hepatocytes within the inflamed, cirrhotic liver that underlies most HCC cases.[117] Strikingly, our pathway analysis revealed that endocytosis and vesicle transport pathways were highly active in tumors #2 and #4 compared with NTL, the same pathways that we found to be activated in mesenchymal-like and therapy resistant HCC lines. Specifically, REPS1 and REPS2 were significantly increased in abundance in two of four HCC tissues compared with NTL

(Figure 2.6D). These results indicate that dysregulation of an endocytic AAK1 network may contribute to HCC EMP and therapy resistance *in vivo*, and that AAK1 and its interaction partners may serve as novel drug target candidates with high translational potential.

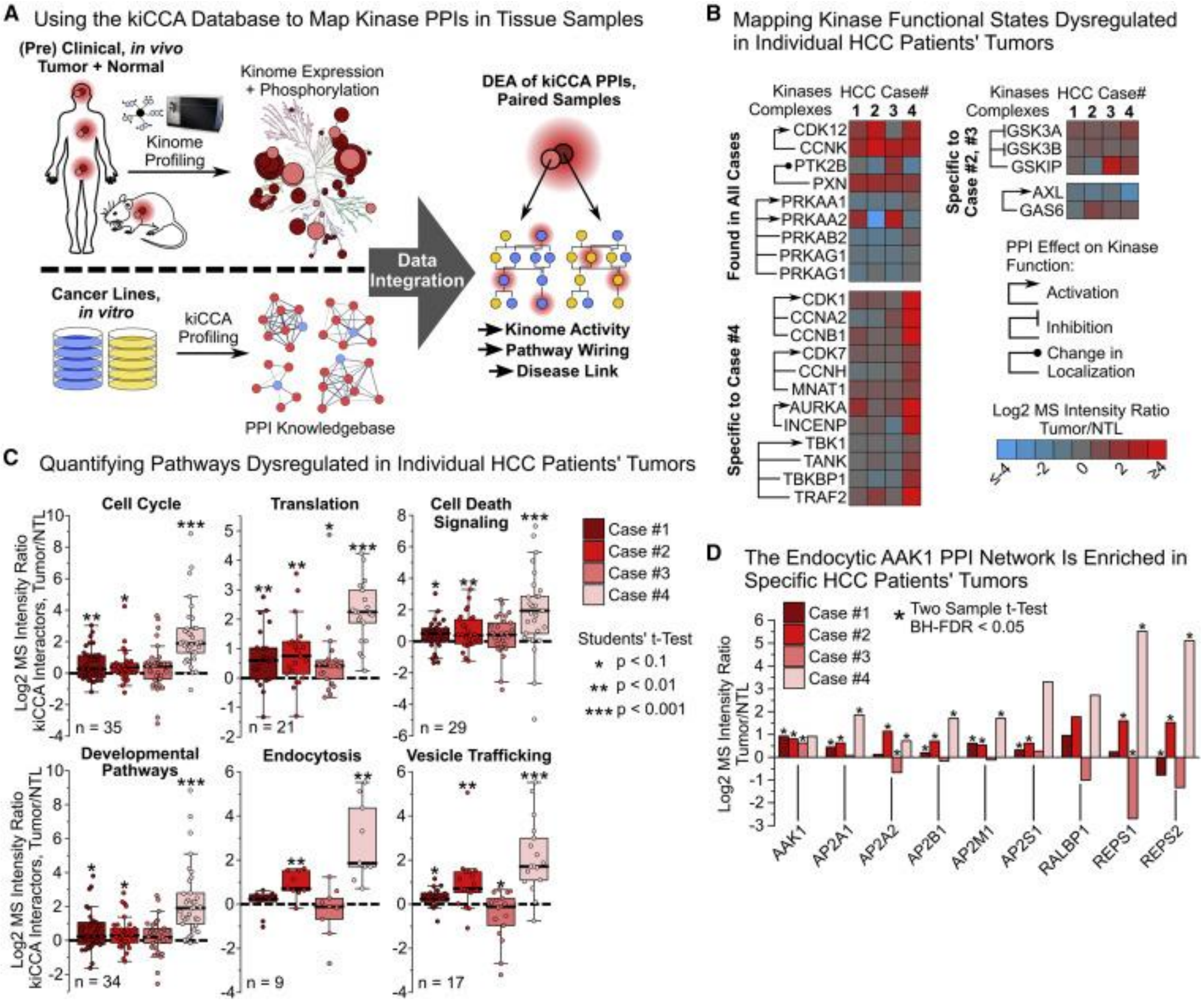

Figure 2.6. Applying our kiCCA interactome Knowledgebase to map kinase PPIs in kinome-centric chemoproteomic datasets from clinical and pre-clinical tissues (A) Workflow for interpreting *in vivo* kinome profiling data from clinical specimens using our kiCCA Knowledgebase. (B) Integrating our kiCCA Knowledgebase with kinobead profiling data from four, paired HCC patients' tumor and non-tumor liver (NTL) samples revealed differential abundance of kinase PPIs, and, thus, aberrations in kinase functional states *in vivo* (two sample t test, BH-FDR = 0.05, n = 5 or 6). (C) Pathway mapping of kinase PPIs altered between HCC patients' tumors and paired NTL tissues revealed dysregulation of cellular pathways (for statistics, see B). Each datapoint is the $\log_2$ MS intensity tumor/NTL ratio of a kiCCA interactor with

significantly different abundance in at least one HCC case; all interactions were then compared across all HCC cases. (D) DEA of the AAK1-mediated PPI network between HCC tumor and NTL tissues revealed frequent upregulation in tumors, suggesting important roles in HCC progression and drug resistance *in vivo* (for statistics, see B). See also Table S3.

2.3. Discussion

We introduced kiCCA, a chemoproteomic approach that exploits KI polypharmacology for highly multiplexed interactome mapping of the kinome. kiCCA allows the high-throughput profiling of various cell states and model systems using native cell and tissue lysates, entirely avoiding the use of antibodies and the expression of genetically tagged bait proteins. We demonstrated that kiCCA is a powerful approach for cell signaling and cancer research as it (1) broadly quantifies kinase interactome changes associated with cancer types, cellular phenotypes, such as neuroblastoma cell NMP and HCC cell EMP and (2) prioritizes kinase complexes for mechanistic studies and drug target discovery, as demonstrated by our identification of an AAK1 complex promoting HCC cell EMP and therapy resistance. We also showed that kiCCA combined with protein cross-linking captured the rapid, kinome-wide rearrangement of transient and low-affinity signaling complexes caused by acute hormone stimuli, highlighting that kiCCA presents a unique tool for cell signaling research. We applied our kinase interactome knowledgebase from 18 diverse cancer lines to identify kinase signaling complexes in kinobead profiling data of clinical tumor samples to gain novel insights into kinase-dependent PPI aberrations in patients' tumors. Although our kinome PPI knowledgebase provides the broadest range of kinome PPIs mapped to date, future kiCCA experiments will increase the diversity of cell and tissue types while additional bespoke kinome PPI databases can be developed from specific cell lines or tissues to match a particular biological context. Our general approach shows the value of PPI network information in studying dysregulated signaling in disease and provides a roadmap for obtaining similar kinobead-based PPI networks for clinical proteomics.

Collectively, we curated an extensive reference set of PPIs that can determine kinase functional states and kinase-pathway integration, thereby allowing us to interpret the biological significance of changes in kinase interactomes. Kinome PPI abundance information derived from biochemical enrichment by kinobeads or other kinome-centric chemoproteomic tools[138] provide quantitative proteomics data that is distinct and complementary to phosphoproteomics data. We expect that the combination of both kinome PPI and phosphorylation site data will provide a more specific and sensitive measurement of kinome activity that would be important for comparing signaling activity between different biological states.

We demonstrated that kiCCA interactome data can identify disease mechanisms and drug targets by characterizing an AAK1-mediated PPI network that links endocytosis and vesicle trafficking pathways to HCC cell EMP and therapy resistance. Knockdown of AAK1 and its interaction partners REPS1 and REPS2, and RALBP1 reduced HCC cell EMP marker expression and decreased drug resistance, showing that kiCCA can identify kinase target candidates as well as non-kinase target candidates, such as REPS1, whose RNAi is better tolerated than AAK1 RNAi, and strongly sensitizes mesenchymal-like cancer cells to targeted therapy. Therefore, inhibiting the AAK1-REPS1 interaction may be a promising strategy to minimize drug cytotoxicity and maximize cancer therapy responses.[82]

The limitations of our kiCCA approach are the same as for any other AP-MS-based method, for instance, difficulties identifying weak and transient PPIs, and the lack of subcellular spatial resolution.[91] Here, we demonstrated that kiCCA with protein cross-linking can increase the coverage of weak and transient PPIs. We speculate that subcellular fractionation, e.g., into cytosolic, membrane, and nuclear fractions, followed by kiCCA could further resolve the localization of kinase signaling complexes and reduce sample complexity to increase the number of identifiable signaling and transcription factor complexes. The throughput of kiCCA can be further increased iteratively by using smaller sets of KIPs and isobaric TMT labeling for analysis of entire interactomes in single LC-MS runs.

In summary, we presented a unique and powerful approach for studying kinase interactome dynamics in virtually any model system that can be broadly implemented in biomedical labs. We collated our kinase interactome data into a knowledgebase that is easily accessible through our supplementary tables and an interactive Shiny web application (https://quantbiology.org/kiCCA), serving as an important resource for cancer and cell signaling researchers.

Limitations of the study

kiCCA enables high-throughput kinome interactomics, however, it currently cannot identify kinase-kinase interactions or determine multiple kinase interactions of a protein in the same sample, thereby missing potentially important signaling events. Future iterations of kiCCA will integrate the kinase binding affinities of KIPs with kinobead competition-binding profiles to distinguish direct probe binding from kinase-kinase co-competition and will utilize improved computational algorithms, such as network propagation methods,[139] to identify multiple kinase interactors of co-precipitating proteins. kiCCA with protein cross-linking identified numerous weak and transient PPIs; yet, kiCCA still requires cell lysis, which dilutes cellular contents ~100-fold, and causes the dissociation of protein complexes. Future iterations of kiCCA will utilize soluble kinome affinity probes to capture kinase interactomes *in situ*. Studying how dysregulated AAK1 PPI network promoted HCC cell EMP and therapy resistance, we showed that RNAi of network components affected the stability of multiple EMP-associated receptor kinases, however, if this is caused by altered transcription or recycling and degradation of receptors, and if the effect can be exploited for pharmacological intervention will have to be clarified in future studies.

Finally, the application of the kiCCA knowledgebase in a new tissue or disease model may not be accurate if there is a new cell/tissue-specific set of kinome PPIs that are not previously captured in the knowledgebase; in such situations, it may be necessary to generate a new model-specific kiCCA database.

2.4. Materials and methods

Cell lines and tissue culture conditions

C3A, SNU398, Hep3B2.1-7, U2-OS, SK-N-SH, SH-SY5Y, JeKo-1, HeLa, Jurkat, A-172, K562, and SNU449 cell lines were purchased from the American Type Culture Collection (ATCC). SNU761 and SNU886 were purchased from the Korean Cell Line Bank (KCLB). JHH6 and HuH-7 cells were purchased from the JRCB Cell Bank. FOCUS WT cells were obtained from the Laboratory of J. Wands, Brown University.[141] FOCUS *AXL* RNAi cells were obtained from Dr. Taranjit Gujral of the Fred Hutchinson Cancer Research Institute, Seattle. All cells were grown at 37°C under 5% CO2, 95% ambient atmosphere. Fifteen cryo-frozen cell stocks were generated from the original vial from the cell bank or from the collaborator's lab (passage 3). Experiments were performed with cells at <10 passages from the original vial. All cell media used were supplemented with 100x penicillin-streptomycin-glutamine (Thermo Fisher Scientific, Waltham, MA). FOCUS and HuH-7 cells were grown in Dulbecco's minimum essential medium (DMEM) supplemented with 10% FBS (VWR Life Science, Seradigm). C3A, SNU398, Hep3B2.1-7, U2-OS, SK-N-SH, SH-SY5Y, JeKo-1, HeLa, Jurkat, A-172, K562, and SNU449 lines were grown in the ATCC-recommended medium. JHH6 cells were grown in William's E medium, and SNU761 and SNU886 lines in RPMI 1640 medium all supplemented with 10% FBS. Cells were harvested when reaching 90% confluency or a density of $1x10^6$ cells/ml.

RNAi knockdown experiments

Three shRNA sequences each targeting *AAK1*, *RALBP1*, *REPS1*, and *REPS2* mRNAs were obtained from The RNAi Consortium (TRC) of the Broad Institute web portal (https://www.broadinstitute.org/rnai-consortium/rnai-consortium-shrna-library, ID Numbers: TRCN0000001943, TRCN0000199939, TRCN0000082348, TRCN0000053363, TRCN0000423162, TRCN0000436095, TRCN0000423057, TRCN0000428939, TRCN0000056210, TRCN0000305689, TRCN0000047918, TRCN0000047920) and cloned into the lentiviral pLKO.1 vector (Plasmid#10878, Dr. David Root's Lab, Addgene, Watertown, MA) as previously described.[147] Lentiviral particles were produced from individual pLKO.1 vectors, the pMD2.G plasmid (envelope, plasmid #12259, Didier Trono, Addgene), and the pCMVR8.74 plasmid (packaging, plasmid #22036, Didier Trono, Addgene) according to the manufacturer's instructions (Addgene). Virus particle-containing cell culture supernatants were sterile filtered over 0.22 µM PES syringe filters (Millex-GP, Sigma Millipore, Burlington, MA), mixed 1:1 with fresh growth medium, 8 µg/mL final polybrene was added and the mixture added to target cells (70-80% confluency). Cells were incubated for 24h, the medium exchanged, and stable cell lines selected using puromycin (FOCUS: 4 µg/mL; SNU387 and SKHep1: 6 µg/mL; SNU761: 8 µg/mL) for 7-14 days. Puromycin-resistant cells were maintained in growth medium containing half of the selection concentration of puromycin. Target knockdown was validated using quantitative real-time PCR, immunoblotting, and kinobead/LC-MS profiling, and the stable cell lines with the highest knockdown among the three shRNAs used for each target were chosen to perform all downstream experiments.

Immunoblot analysis and antibodies

Antibodies used for immunoblotting were anti-E-cadherin (24E10, Cell Signaling Technology, CST, Cat # 3195), anti-AXL (C89E7, CST, Cat # 8661), anti-Snail (C15D3, CST, Cat

3879), anti-ZEB1 (E2G6Y, CST, Cat # 70512), anti-CD44 (E7K2Y, CST, Cat # 37259), anti-GAPDH HRP conjugate (D16H11, CST, Cat # 8884), anti-AAK1 (E8M3P, CST, Cat # 61527), anti-RALBP1 (D87H8, CST, Cat # 5739), anti-REPS1 (D6F4, CST, Cat # 6404), anti-CDK4 (D9G3E, CST Cat # 12790), anti-CDK6 (DCS83, CST, Cat # 3136), anti-CDK2 (78B2, CST, Cat # 2546), anti-Cyclin D1 (92G2, CST, Cat # 2978), and anti-Cyclin D3 (DCS22, CST, Cat # 2936). Cell lysis and immunoblotting experiments were performed using standard procedures. Briefly, cells were rinsed twice with ice-cold phosphate buffered saline (PBS), lysed in modified RIPA buffer V1 (50 mM Tris-HCl, 150 mM NaCl, 1% NP-40 (v/v), 0.25% Na-deoxycholate (w/v), 1 mM EDTA, 10 mM NaF, 5% glycerol (v/v), pH 7.8) supplemented with HALT protease inhibitor (100x, Thermo Fisher Scientific, Waltham, MA), and lysates clarified by centrifugation at 21,000 rcf for 20 minutes at 4°C. Protein concentration was quantified using the Piece 660 nm Protein Assay Reagent (Pierce, Rockford, IL). Lysates were mixed with NuPAGE LDS Sample Buffer (4X, Thermo Fisher Scientific) containing 50 mM DTT and heated for 5 min at 95°C. 20 µg of protein was separated on Bolt 4-12% Bis-Tris Protein Gels (Thermo Fisher Scientific) and electro-transferred onto nitrocellulose membranes. The buffer used for blocking and antibody incubation was 5% BSA in TBS-T (50 mM NaCl, 150 mM Tris-HCl, 1% Tween-20, pH = 7.8). Membranes were incubated with goat anti-rabbit HRP conjugate, and bands visualized using the Clarity Western ECL Substrate (Bio-Rad, Hercules, CA) and the Fluor Chem E imaging system (Protein Simple, San Jose, CA).

Quantitative real-time PCR Analysis of mRNA expression

shRNA-mediated knockdown was validated by quantifying the target's mRNA expression levels using quantitative real-time PCR. Briefly, cells were cultured on 35 mm dishes until reaching 80-90% confluency and total mRNA was isolated using the TRIzol reagent according to manufacturer's instructions (Thermo Fisher Scientific). mRNA quality was controlled by running 1% agarose gels and assessing the presence of sharp, clear 28S and 18S rRNA bands. 0.5 µg of total RNA was used to generate first-strand cDNA using the Protoscript II First Strand cDNA Synthesis Kit (New England Biolabs, Ipswich, MA). The resulting cDNA was subjected to quantitative real-time PCR using human gene-specific primers for *AAK1*, *RALBP1*, *REPS1*, and *REPS2*, and two housekeeping genes, i.e., *PSMB2* and *RAB7A*. The quantitative real-time PCR reaction was performed using QuantStudio 5 Real-Time PCR System (Applied Biosystems, Thermo Fisher Scientific) using the following program:

Step	**Temp (°C)**	**Time (mm.ss)**	**Cycles**
Hold (Enzyme Active)	**50, 95**	**02:00, 10:00**	**1**
PCR (Denature, Anneal, Extend)	**95, 50, 60**	**00:15, 00:15, 01:00**	**50**
Dissociation/Melting Curve	**95, 60, 95**	**00:15, 01:00, 00:15**	**5**

The mRNA levels of each gene were normalized relative to the mean levels of the two housekeeping genes and compared with the data obtained from cell lines carrying a stably incorporated scramble shRNA using the 2-ΔΔCt method. According to this method, the normalized level of a mRNA, X, is determined using the following equation:

$$X = 2^{-Ct(GOI)} / 2^{-Ct(CTL)}$$

where Ct is the threshold cycle (the number of the cycle at which an increase in reporter fluorescence above a baseline signal is detected), GOI refers to the gene of interest, and CTL refers to a control housekeeping gene. This method assumes that Ct is inversely proportional to the initial concentration of mRNA and that the amount of product doubles with every cycle.

Inhibitor treatment of RNAi and scramble lines for the growth inhibition assay

1800 cells/well were seeded onto white flat bottom half area 96-well plates (Greiner Bio-One, Kremsmünster, AT) in 50 µl of growth medium and allowed to attach in an incubator for 24 h. Then the drugs in DMSO and/or DMSO vehicle controls as 11X solutions in growth medium were added to a total volume of 55 µl and 0.1% DMSO final. The cells were grown in an incubator for another 72 h. Then, 55 µl of CellTiter-Glo 2.0 (Promega, Madison, WI) reagent/well were added according to the manufacturer's instructions and luminescence was quantified with a SpectraMax 190 plate reader (Molecular Devices, San Jose, CA). The drugs AZD7762 (CHEK1 inhibitor, Selleckchem, Houston, TX), CHIR-124 (CHEK1 inhibitor, ApexBio, Houston, TX), Selumetinib (MEK1/2 inhibitor, Selleckchem), Dasatinib (SRC inhibitor, Selleckchem), Lenvatinib (FGFR inhibitor, Selleckchem), Sorafenib and Regorafenib (BRAF inhibitors, Selleckchem), Cabozantinib (AXL and MET inhibitor, Selleckchem), and Doxorubicin (Cytotoxic/TopII inhibitor, Selleckchem) were applied at 8 different concentrations between 10 µM and 4.6 nM (3-fold dilution steps). The drugs Dinaciclib (CDK inhibitor, Selleckchem) and Volasertib (PLK1/BRD2 inhibitor, Selleckchem) were applied at 8 different concentrations between 1 µM and 0.46 nM (3-fold dilution steps). Experiments were performed in four biological replicates. Growth inhibition curves were fitted using the GraphPad Prism software package (V5.0a) with a least-squares nonlinear regression model for curve fitting (One site - Fit logIC50 function).

Preparation of optimized kinobead mixture

The seven used kinobead affinity reagents were either synthesized in house or custom synthesized through Bellen Chemistry (Beijing, China), and kinobeads were prepared as previously described.[97, 106, 148] For optimal coverage of the human kinome an optimized mixture of the seven kinobead reagents was prepared as previously described.[106] Briefly, 1 ml of reagent 1, 0.5 ml of reagents 2, 3 and 7, respectively, and 0.25 ml of reagents 4, 5 and 6, respectively, were mixed to yield 3.25 ml of the complete kinobead mixture. All reagents were a 50% slurry in 20% aq. ethanol.

Kinase affinity enrichment, KI competition, and on-bead digestion

Kinase affinity enrichment, KI competition, and on-bead digestion was performed as previously described.[97, 104, 140] Briefly, to 150 µL of cell lysate (5 mg protein per mL) in modified RIPA buffer V1 (50 mM Tris-HCl, 150 mM NaCl, 1% NP-40 (v/v), 0.25% Na-deoxycholate (w/v), 1 mM EDTA, 10 mM NaF, 5% glycerol (v/v), pH 7.8) containing HALT protease inhibitor cocktail (100x, Thermo Fisher Scientific, Waltham, MA) and phosphatase inhibitor cocktail II and III (100x, Sigma-Aldrich, St Louis, MO) 1.5 µL DMSO (vehicle control) or the corresponding inhibitor solution in DMSO (competition) were added to a final concentration 1% DMSO. The lysate was vortexed at intermediate speed intermittently every 5 min for 20 min while being kept on ice. Meanwhile, 40 µl of a 50% slurry of the in-house-made, optimized kinobead mixture in 20% aq. ethanol were prepared for each pulldown experiment. The beads were washed twice with 400 µl modified RIPA buffer and lysates containing DMSO, or inhibitor were added. The mixture was incubated on a tube rotator for 3h at 4°C and then the beads were pelleted rapidly at 2000 Xg on a benchtop centrifuge (5s). After removal of the supernatant, the beads were rapidly washed twice with 400 µl of ice-cold mod. RIPA buffer and three times with 400 µl ice-cold tris-buffered saline (TBS, 50 mM tris, 150 mM NaCl, pH 7.8) to remove detergents. 100 µl of freshly prepared denaturing buffer (8M urea, 100 mM Tris, pH 8.5) containing 5 mM tris(2-carboxyethyl)phosphine hydrochloride (TCEP*HCl) and 10 mM chloroacetamide (CAM), were added and the slurry agitated on a thermomixer at 37°C and 1400 rpm for 30 min. The mixture was diluted 2-fold with 100 mM triethylamine bicarbonate (TEAB), the pH adjusted to 8-9 by addition 1 N aq. NaOH; 2 µg LysC were added, and the mixture agitated on a thermomixer at 1400 rpm at 37°C for 2 h. Then, the mixture was diluted another 2-fold with 100 mM TEAB, 2 µg MS-grade trypsin (Thermo Fisher Scientific, Waltham, MA) were added, and the mixture agitated on a thermomixer at 1400 rpm at 37°C overnight. Then, 6 µL of formic acid (FA) were added (1.5% FA final) to adjust to pH 3 and peptides were extracted and desalted using C18 StageTips according to the published protocol.[149] For kinobead/LC-MS profiling of RNAi cell lines the same protocol was applied except that the lysates were not preincubated with DMSO or inhibitor. The following kinase inhibitors were used as KIPs for competition experiments at the given final concentrations: GSK-690693 (10 µM, MedChemExpress, MCE, Monmouth Junction, NJ), Miliciclib (10 µM, MCE), Rebastinib (10 µM, MCE), AT9283 (10 µM, MCE), TAK-901 (10 µM, MCE), RGB-286638 (10 µM, MCE), Flavopiridol*HCl (10 µM, MCE), PF-562271 besylate (10 µM, MCE), Dabrafenib mesylate (10 µM, MCE), OTSSP167*HCl (10 µM, MCE), CYC-116 (10 µM, MCE), Silmitasertib (10 µM, MCE), SB1317 (10 µM, MCE), XL228 (10 µM, MCE), Sapanisertib (10 µM, MCE), PF-3758309 (10 µM, ApexBio), Staurosporine (replacing the structurally closely related K-252a, 1 µM, LC Labs, Woburn, MA), AZD-7762 (10 µM Selleckchem), Bosutinib (10 µM, Selleckchem), Dasatinib (10 µM, Selleckchem), LP-935509 (1 µM, MCE), and Linsitinib (10 µM, ApexBio).

Kinobead/LC-MS competition with the 21 KIPs and formaldehyde-mediated protein crosslinking

Kinobead competition with formaldehyde-mediated protein crosslinking was performed as described in 'Kinase affinity enrichment, KI competition, and on-bead digestion' above with the following modifications. To 150 µL of cell lysate (5 mg protein per mL) in modified RIPA buffer V2 (50 mM HEPES, 150 mM NaCl, 1% NP-40 (v/v), 0.25% Na-deoxycholate (w/v), 1 mM EDTA, 10 mM NaF, 5% glycerol (v/v), pH 7.8) containing HALT protease inhibitor cocktail (100x, Thermo Fisher Scientific, Waltham, MA) and phosphatase inhibitor cocktail II and III (100x, Sigma-Aldrich, St Louis, MO) 1.5 µL DMSO (vehicle control) or the corresponding inhibitor solution in DMSO (competition) were added to a final concentration 1% DMSO. The lysate was vortexed at intermediate speed intermittently every 5 min for 20 min while being kept on ice. The mixture was added to the kinobeads and incubated on a tube rotator for 3h at 4°C and then 4 µL of 37 wt% aq. Formaldehyde solution was added (1% concentration final). The mixture was incubated on a tube rotator for an additional 30 min at 4°C and then the beads were pelleted rapidly at 2000 rpm on a benchtop centrifuge (5s). After removal of the supernatant, the beads were rapidly washed twice with 400 µl of ice-cold mod. RIPA buffer V2 and three times with 400 µl ice-cold HEPES-buffered saline (HBS, 50 mM HEPES, 150 mM NaCl, pH 7.8) to remove detergents. 100 µl of the denaturing buffer (6M Gdn*HCl, 100 mM Tris-HCl, pH 8.5) containing 5 mM tris(2-carboxyethyl)phosphine hydrochloride (TCEP*HCl) and 10 mM chloroacetamide (CAM), were added and the slurry agitated on a thermomixer at 70°C and 1400 rpm for 30 min to reverse crosslinking. The mixture was then subjected to the same digestion protocol and downstream handling as described above "Kinase affinity enrichment, KI competition, and on-bead digestion."

Co-immunoprecipitation/MS (CoIP/MS) analyses of AAK1 and CK2 PPI networks

200 µl of the corresponding cell lysate in modified RIPA buffer V1 (5 mg/mL protein) containing protease and phosphatase inhibitors (see ‘Kinase affinity enrichment, KI competition and on-bead digestion’) were incubated with antibodies against AAK1, RALBP1, or REPS1 (FOCUS cell lysate, see ‘Immunoblot analysis and antibodies’), CK2α or CK2β (U2-OS cell lysate, Novus Biologicals, CK2α Ab: polyclonal, # NB100-378, CK2β Ab: polyclonal, #NBP1-06515) or GFP (control, clone D5.1, CST, Cat # 2956) at the manufacturer's recommended concentrations, respectively, and agitated overnight on a tube rotator at 4°C. The next day, Pierce Protein A Agarose (Thermo Fisher Scientific) was washed twice with ice-cold modified RIPA buffer V1 and 40 µL aliquots of a 50% bead slurry were added to each lysate/antibody mixture. The slurry was agitated for 3h on a tube rotator at 4°C, the supernatant was aspirated, and then the beads were washed twice with ice-cold modified RIPA buffer V1 and three times with TBS. Proteins were reduced, alkylated, and eluted by adding 100 µL denaturing buffer (8M urea, 5mM TCEP, 10mM CAM, 100 mM Tris pH 7.8) to beads and agitating them on a thermomixer at 1,400 rpm for 30 min at 37°C. The supernatant containing the protein was transferred to a new tube and diluted two-fold with 100 mM TEAB, and the pH was adjusted to 8.5 using 1N NaOH solution. 2 µg of Lys-C (Wako Chemicals) were added, and samples agitated on a thermo mixer at 1,400 rpm for 2 h at 37°C. Then, samples were diluted another two-fold with 100 mM TEAB and 2 µg of MS-grade trypsin (Thermo Fisher Scientific) were added. The mixture was agitated on a thermomixer at 1,400 rpm overnight at 37°C. The resulting peptide solution was acidified with formic acid to achieve pH <3 (1.5% FA final) and desalted using C18 StageTips according to the published protocol.[149] Co-IP/MS experiments were performed in three biological replicates per antibody.

nanoLC-MS/MS analyses

LC-MS analyses were performed as described previously with the following minor modifications.[97, 106] Peptide samples were separated on an EASY-nLC 1200 System (Thermo Fisher Scientific) using 20 cm long fused silica capillary columns (100 µm ID, laser pulled in-house with Sutter P-2000, Novato CA) packed with 3 µm 120 Å reversed phase C18 beads (Dr. Maisch, Ammerbuch, DE). The LC gradient was 120 min long with 5−35% B at 300 nL/min. LC solvent A was 0.1% (v/v) aq. acetic acid and LC solvent B was 20% 0.1% (v/v) acetic acid, 80% acetonitrile. MS data was collected with a Thermo Fisher Scientific Orbitrap Fusion Lumos. Data-dependent analysis was applied using Top15 selection with CID fragmentation.

Computation of MS raw files

Data.raw files were analyzed by MaxQuant/Andromeda[72] version 1.5.2.8 using protein, peptide and site FDRs of 0.01 and a score minimum of 40 for modified peptides, 0 for unmodified peptides; delta score minimum of 17 for modified peptides, 0 for unmodified peptides. MS/MS spectra were searched against the UniProt human database (updated July 22nd, 2015). MaxQuant search parameters: Variable modifications included Oxidation (M) and Phospho (S/T/Y). Carbamidomethyl (C) was a fixed modification. Max. missed cleavages was 2, enzyme was Trypsin/P and max. charge was 7. The MaxQuant “match between runs” feature was enabled. The initial search tolerance for FTMS scans was 20 ppm and 0.5 Da for ITMS MS/MS scans.

MaxQuant output data processing

MaxQuant output files were processed, statistically analyzed and clustered using the Perseus software package v1.5.6.0.[143] Human gene ontology (GO) terms (GOBP, GOCC and GOMF) were loaded from the ‘mainAnnot.homo_sapiens.txt’ file downloaded on 02.03.2020. Expression columns (protein and phosphopeptide intensities) were $\log_2$ transformed and normalized by subtracting the median $\log_2$ expression value from each expression value of the corresponding data column. Potential contaminants, reverse hits and proteins only identified by site were removed. Reproducibility between LC-MS/MS experiments was analyzed by column correlation (Pearson's r) and replicates with a variation of $r > 0.25$ compared to the mean r-values of all replicates of the same experiment (cell line or knockdown experiment) were considered outliers and excluded from the analyses. Data imputation was performed in Perseus using a modeled distribution of MS intensity values downshifted by 1.8 and having a width of 0.2.

Kinobead competition correlation analysis (kiCCA)

For each cell line and condition tested, 21 KIP competition experiments and one DMSO control experiment were performed in biological duplicate, resulting in 44 kinobead pulldown and LC-MS experiments per condition/cell line. We called a kinase or non-kinase protein competed if it showed a $\log_2$ MS intensity ratio of ≥ 0.75 and passed a two-sample t-test $p < 0.1$ with at least one of the 21 KIs used, i.e., comparing the two DMSO control experiments and two corresponding KI competition experiments. We then correlated MS intensity values of all competed kinases and co-competed non-kinase proteins using Pearson moment correlation ($n = 44$). Then, kinases that showed similar competition behavior were combined into groups, and the maximum r-value of members retained for that group. Next, we removed kinase groups that showed very large numbers of PPIs with high positive r-values, which was caused by systemic shifts in MS intensity for certain non-kinase proteins between biological replicates. These kinases show a systematic upshift in PPI r-values that can be recognized by an unusually high median and 3rd quartile (Q3) value for the kiCCA r-value distribution. Accordingly, we calculated the Q3 for each kinase group, determined high, positive outliers of Q3 values using box plots (outlier = 1.5*IQR), and removed kinase groups that appeared as outliers from downstream analysis. Finally, the kinase group which showed the highest r-value for each non-kinase protein was determined, representing the most probably kinase group–protein interaction among all possible interaction for each cell line or condition.

Differential expression analysis (DEA)

To identify differentially expressed proteomic features between cell lines, tissues, and treatment conditions, we applied either a two-sample t-test or a student's t-test against the null hypothesis, applying Benjamini-Hochberg correction for multiple hypothesis testing ($FDR < 0.05$, discovery mode in kinobead profiling and kiCCA data), or we applied a simple $p < 0.05$ (validation mode in kinobead and Co-IP/MS data). Briefly, for two sample t-testing of protein MS intensity differences in kinobead profiling data, we calculated the differences of the mean $\log_2$ MS intensities in each population ($n = 5$ or 6, $\log_2$ MS intensity ratio) and tested for significant differences between the two populations. For Student's t-testing of differential protein expression between the kiCCA datasets of each cell line or condition, we first calculated paired mean differences of $\log_2$ MS intensities for each kinome interactome probe (KIP) or DMSO control ($n = 22$) and then tested the population of ratio values against the null hypothesis, the mean $\log_2$ differences across the probe panel representing protein expression changes.

Determining kinase groups with similar KIP binding profiles

Like kiCCA correlation analysis, kinase MS Intensity values were correlated with one another for each cell line and condition tested to identify kinases with very similar KIP binding profiles. Thus, kinases that show an r-value > 0.9 in at least 7 of 21 tested cell line were combined into kinase groups, defining that the interactors of kinases in these groups cannot be distinguished using kiCCA. Examples are PRKAA1 and 2, AAK1 and BMPK, as well as STK24 and STK26.

Plotting STRING interaction networks

PPI network models were plotted using the STRING web application version 11.5 with the following settings: Edges were scaled with confidence, and only 'physical subnetwork' interactions were considered, i.e., only considering text mining, experiments, and databases.[112]

KS-test analysis and receiver operating characteristic (ROC) plots

Combined PPIs from BioGrid (v.4.4.200, July 25 2021)[108], BioPlex[87], and Buljan et. al. 2020[86] were used to populate the 'known' PPIs in our dataset and used as the binary classifier. The kiCCA Pearson's r-value was used as the discrimination variable. KS plots were generated with the 'ROCit' package in R. ROC p-values were determined with the 'verification' package in R.

Kinome dendrograms

Kinome dendrograms were prepared using the KinMap web application (http://kinhub.org/kinmap/).[146]

Mapping high confidence kiCCA PPIs that determine kinase functional states

High confidence kinase interaction partners identified by kiCCA were searched in the BioGRID[108] and UniProt[116] databases. PubMed IDs were retrieved for publications that previously described the effect of a PPI on kinase function, i.e., activation, inhibition, or a change in cellular localization. Kinase PPIs for which there was evidence from a closely related kinase only, for example the Src-family kinases SRC and FYN, were marked with 'By similarity'.

Mapping high confidence kiCCA interactors to 32 disease relevant GOBP terms

The search strings were used to annotate pathway membership of the 684 high confidence kiCCA interactors in gene ontology-biological process (GOBP) terms. Proteins were annotated using Perseus and the 'mainAnnot.homo_sapiens.txt' file downloaded on 02.03.2020.

Calculating the kiCCA score

To determine the rank order of most likely kinase interactors of non-kinase proteins that can interact with several kinases in our kinase interactome knowledgebase, we introduced a kiCCA score for each kinase PPI that considers both the mean kiCCA r-value and the number of times the interaction was identified in the 21 cancer cell lines and cell states. The kiCCA score can be calculated according to the formula below:

$$kiCCA\ Score = \bar{r}/n$$

Where $\bar{r}$ the mean kiCCA Pearson's r-value across all samples and n is the number of cell lines and states tested (number of samples, in our case 21).

GSEA analysis

For gene set enrichment analysis (GSEA), we used the ssGSEA2.0 script in R together with the Gene Ontology: Biological Process (GOBP) gene set of the MSigDB database ('c5.bp.v7.0.symbols') according to the published protocol with the following minor modifications.[119] To rank gene names, we calculated a compound score using the two sample t-test of Student's t-test $\log_2$ MS intensity ratio multiplied by the $-\log_{10}$ p-value. The parameters used for GSEA were: sample.norm.type = "none", weight = 1, statistic = "area.under.RES", output.score.type = "NES", nperm = 1e3, min.overlap = 10, correl.type = "z.score", par = T, spare.cores = 1, export.signat.gct = T, extended.output = T. To display GSEA results in the heatmap (Figure S2.10B), we calculated an adjusted normalized enrichment score (NES), by multiplying the NES with the $-\log_{10}$ FDR.

Additional resources

An interactive web application of the kinome interactome data is available: https://quantbiology.org/kiCCA.

2.5. Supplemental figures

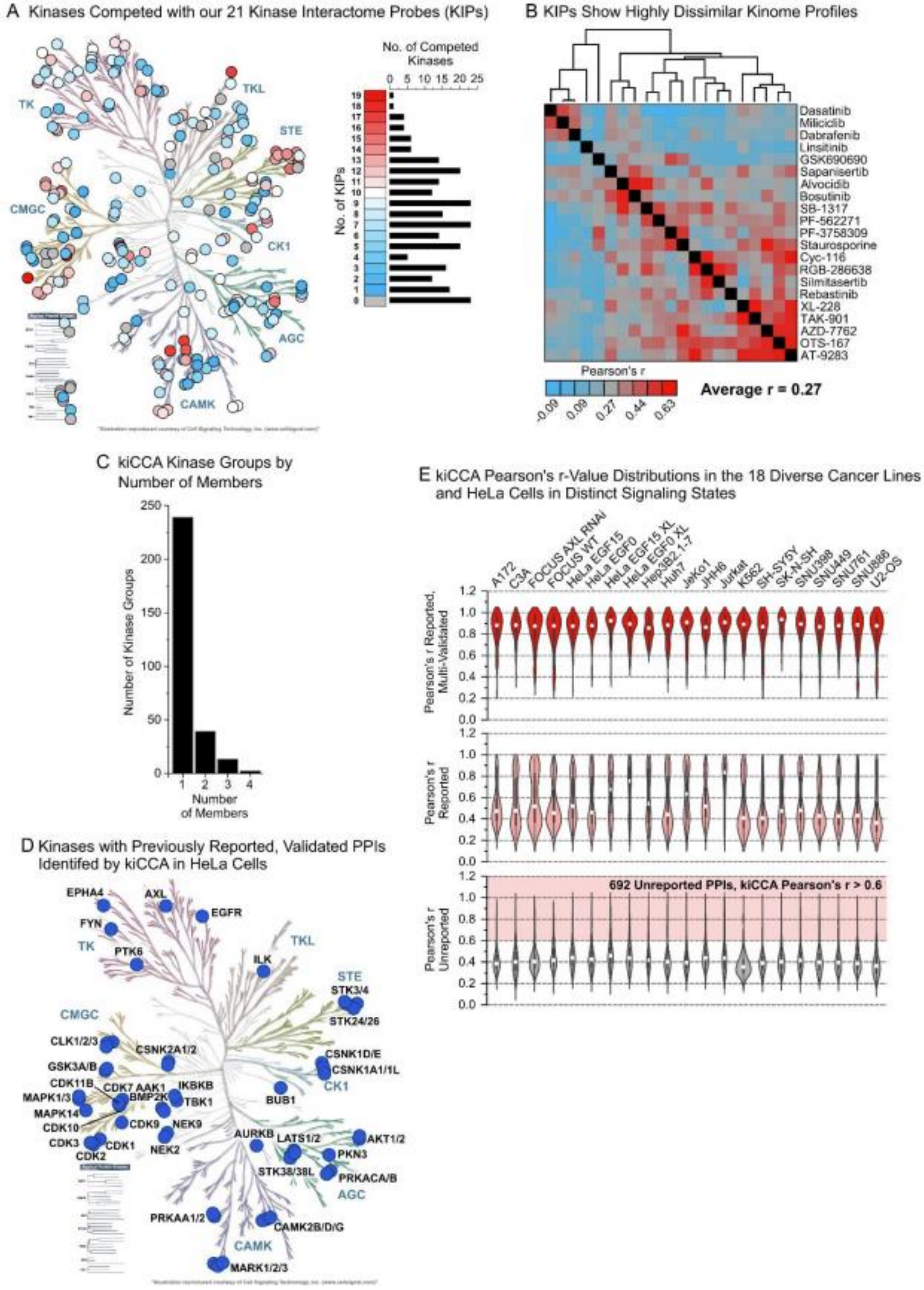

Figure S2.1. Identifying a set of complementary kinome interactome probes (KIPs), pilot kiCCA experiment in HeLa cells, and kiCCA profiling of 18 diverse cancer lines. Related to Figure 2.2. (A) Kinases significantly competed in our kinobead/LC-MS soluble competition assay using our 21 KIP panel (HeLa lysate, log2 MS intensity ratio >0.75 and t-test p-value < 0.1, n = 2). (B) Pairwise Pearson correlation of KIP kinome profiles (kinase log2 MS intensity ratios), followed by unsupervised hierarchical clustering confirms high complementarity. (C) Breakdown of kiCCA kinase groups by number of members. (D) Overlaying kinases for which kiCCA identified previously reported PPIs in HeLa cell lysate with the human kinome dendrogram (n = 37 kinase groups). (E) kiCCA Pearson's r-value distributions for reported and independently validated (BioGRID, top panel), reported but unvalidated (middle panel), and unreported interactions (bottom panel) across 18 diverse cell lines and HeLa cells in different signaling states.

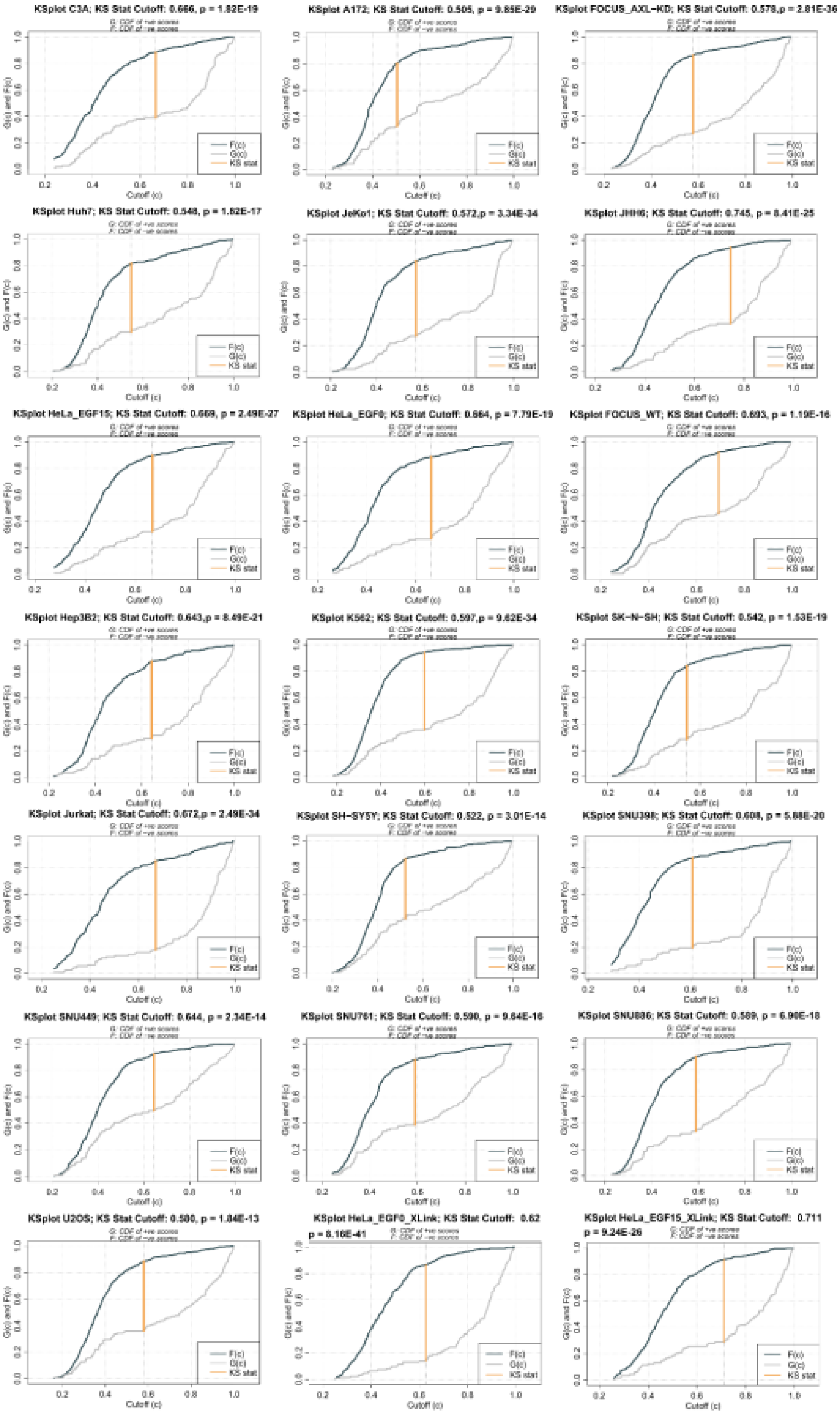

KSplot C3A; KS Stat Cutoff: 0.666, p = 1.82E-19

KSplot A172; KS Stat Cutoff: 0.505, p = 9.85E-29

KSplot FOCUS_AXL−KD; KS Stat Cutoff: 0.578,p = 2.81E-36

KSplot Huh7; KS Stat Cutoff: 0.548, p = 1.82E-17

KSplot JeKo1; KS Stat Cutoff: 0.572,p = 3.34E-34

KSplot JHH6; KS Stat Cutoff: 0.745, p = 8.41E-25

KSplot HeLa_EGF15; KS Stat Cutoff: 0.669, p = 2.49E-27

KSplot HeLa_EGF0; KS Stat Cutoff: 0.664, p = 7.79E-19

KSplot FOCUS_WT; KS Stat Cutoff: 0.693, p = 1.19E-16

KSplot Hep3B2; KS Stat Cutoff: 0.643,p = 8.49E-21

KSplot K562; KS Stat Cutoff: 0.597,p = 9.62E-34

KSplot SK−N−SH; KS Stat Cutoff: 0.542, p = 1.53E-19

KSplot Jurkat; KS Stat Cutoff: 0.672,p = 2.49E-34

KSplot SH−SY5Y; KS Stat Cutoff: 0.522, p = 3.01E-14

KSplot SNU398; KS Stat Cutoff: 0.608, p = 5.88E-20

KSplot SNU449; KS Stat Cutoff: 0.644, p = 2.34E-14

KSplot SNU761; KS Stat Cutoff: 0.590, p = 9.64E-16

KSplot SNU886; KS Stat Cutoff: 0.589, p = 6.90E-18

KSplot U2OS; KS Stat Cutoff: 0.580, p = 1.84E-13

KSplot HeLa_EGF0_XLink; KS Stat Cutoff: 0.62 p = 8.16E-41

KSplot HeLa_EGF15_XLink; KS Stat Cutoff: 0.711 p = 9.24E-26

Figure S2.2. KS statistics for kiCCA profiling results of our 18-cancer cell line panel. Related to Figure 2.2.

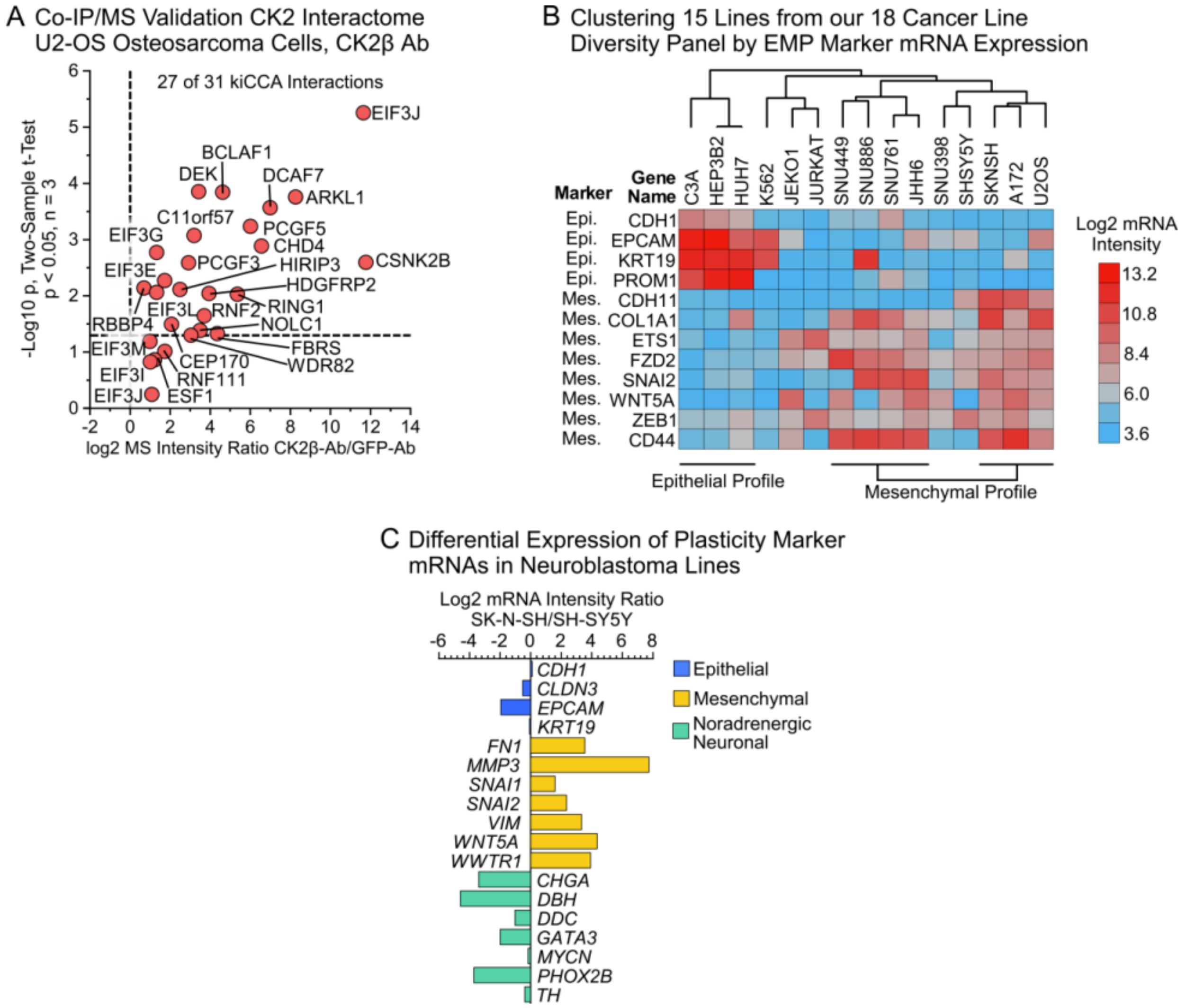

Figure S2.3. Validation of the CK2 interactome and marker mRNA expression in the 18-cancer line panel. Related to Figures 2.3 and 2.4. (A) Co-IP/MS experiment in U2-OS osteosarcoma cells using an antibody specific to the casein kinase 2 regulatory subunit (CK2β) validates a CK2 interaction network identified by kiCCA (GFP antibody was control, two sample t-test, $p < 0.05$, $n = 3$) (B) Clustering of 15 cancer cell lines included in our diversity panel by EMP marker mRNA expression ($n = 52$). Shown are the 12 most characteristic markers for the epithelial-like and mesenchymal-like phenotype. (C) Comparing marker mRNA expression for EMP and noradrenergic neuronal differentiation between the SK-N-SH and SH-SY5Y neuroblastoma lines.

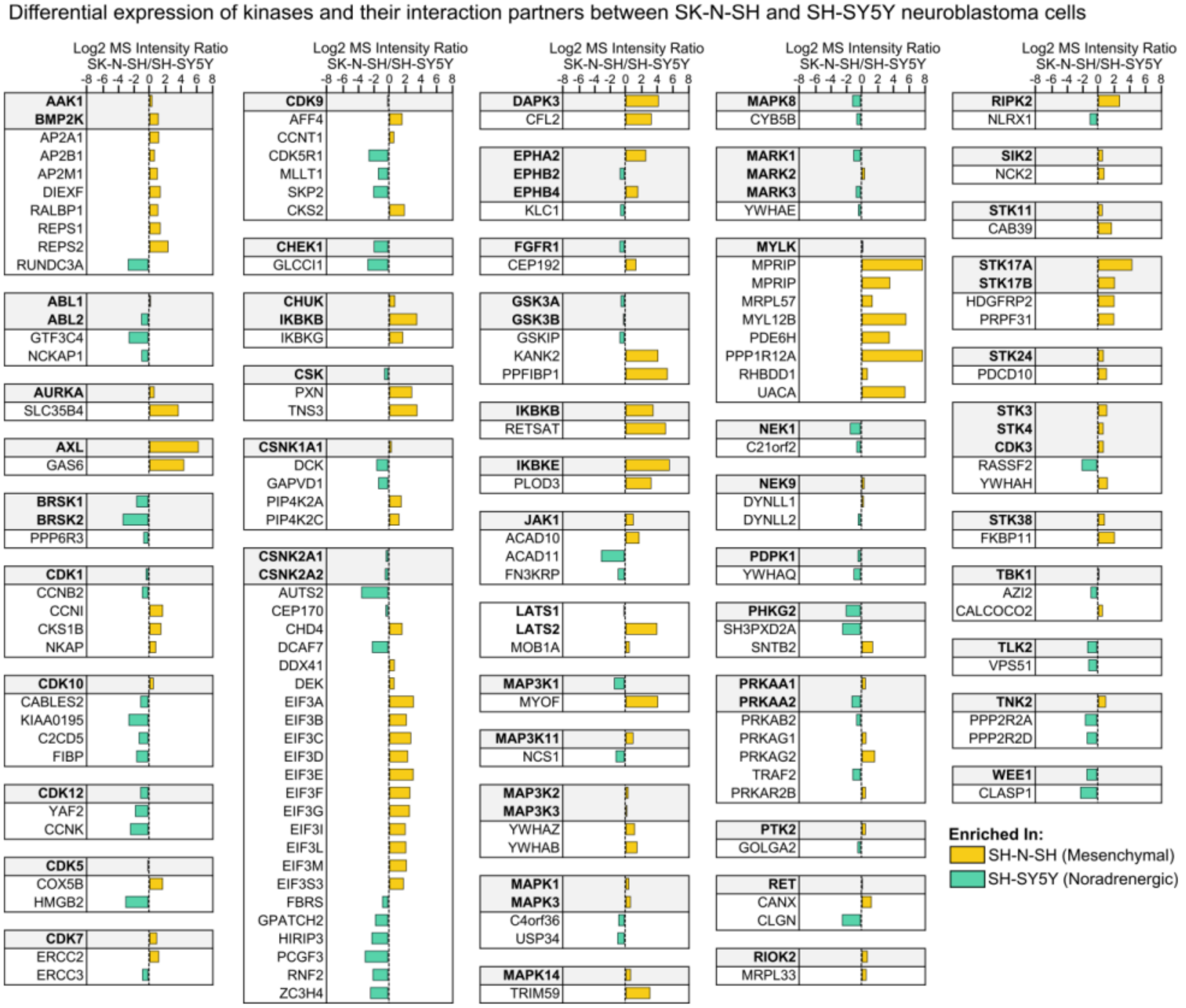
Differential expression of kinases and their interaction partners between SK-N-SH and SH-SY5Y neuroblastoma cells

Figure S2.4. Kinases and their kiCCA interaction partners that were found to be differentially expressed between the mesenchymal-like SK-N-SH and the noradrenergic SH-SY5Y neuroblastoma lines (Student's t-test, BH-FDR = 0.05, n = 22). Related to Figure 2.3.

A Correlation, DEA ratios kinases and their interactors SK-N-SH/SH-SY5Y protein expression (kiCCA) vs mRNA expression (CCLE)

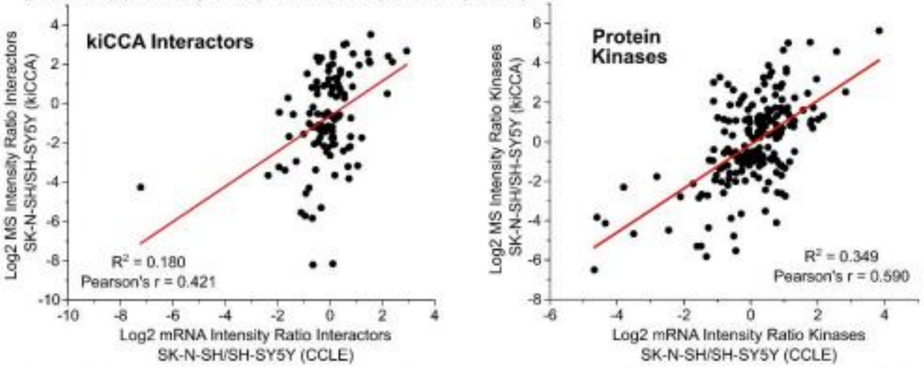

B Kinases whose interaction partners change in abundance in response to EGF treatment, kiCCA ± FA crosslinking

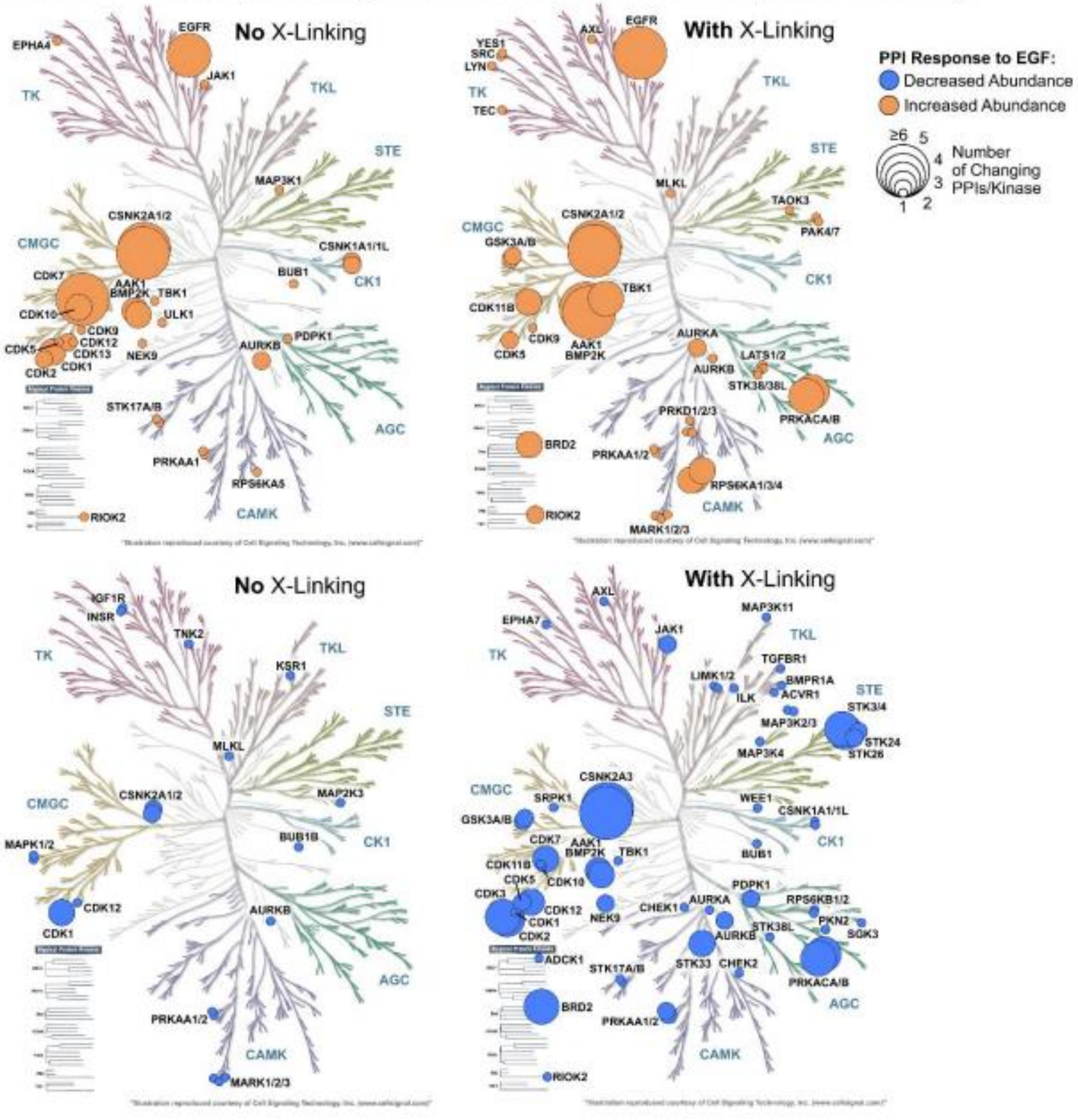

Figure S2.5. Correlation of differentially expressed kiCCA interactors and kinases at the protein and mRNA level, and results from kiCCA profiling of EGF-stimulated HeLa cells. Related to Figure 2.3. (A) Correlation of log2 ratio of mRNA intensity (CCLE data) and log2 ratio of MS intensity differences of high confidence kiCCA interactors and protein kinases between the mesenchymal-like SK-N-SH and the noradrenergic SH-SY5Y neuroblastoma lines. (B) Overlay of the human kinome dendrogram with kinases whose interaction partners show altered abundance in response to EGF treatment (Student's t-test, BH-FDR < 0.05, $n = 22$). Kinase interactions that were identified by kiCCA without protein crosslinking are shown on the left, interactions identified only when using formaldehyde-mediated protein crosslinking are shown on the right.

A Kinases for which kiCCA identified PPIs that inform about their functional state

B Mapping kiCCA interactors to 32 disease-relevant signaling pathways and processes

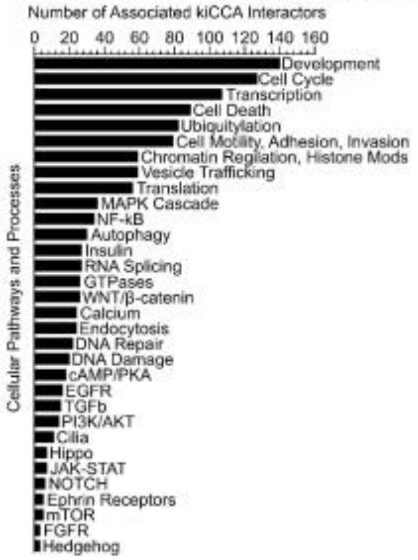

C Correlation, differential expression kinases and their interactors HuH7 and SNU761protein expression (kiCCA) vs mRNA expression (CCLE)

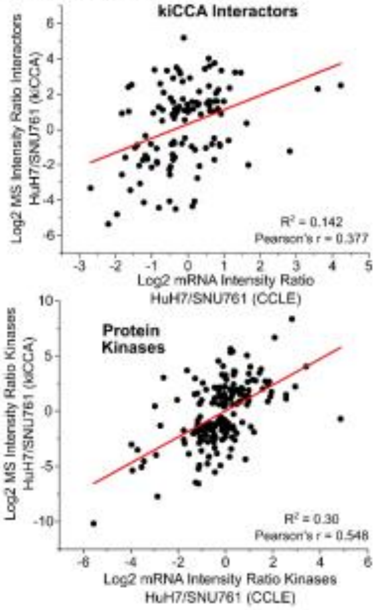

D kiCCA Pathway Analysis of HuH-7 and SNU761Cells Identifies HCC cell EMP pathways

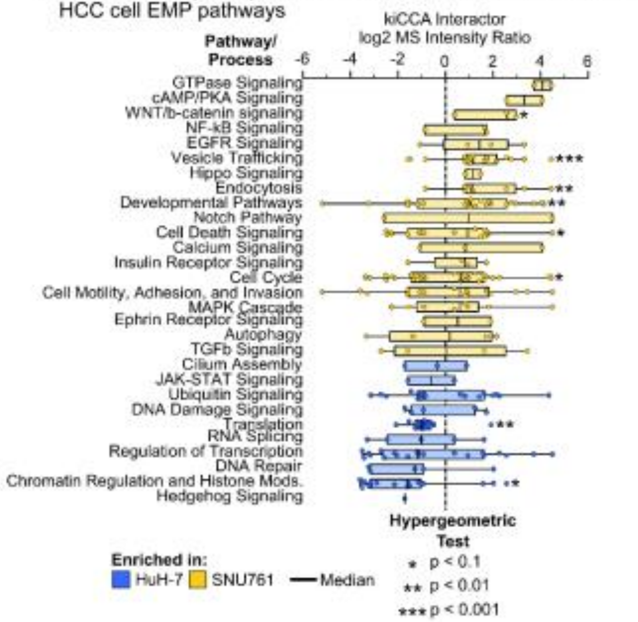

E GSEA analysis validates enrichment of endocytosis pathways in mesenchymal HCC cells

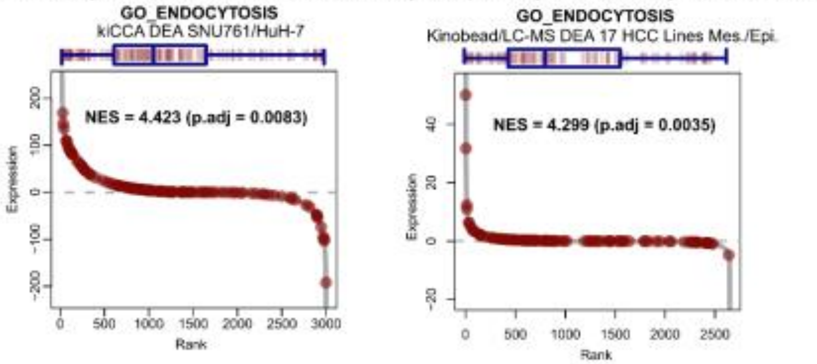

Figure S2.6. Defining functional kiCCA PPIs and pathway associations, correlation of differentially expressed kiCCA interactors and kinases at the protein and mRNA level, and kiCCA and GSEA signaling pathway analysis of the HuH-7 and SNU761 HCC lines. Related to Figure 2.4. (A) Kinases with identified PPIs indicating kinase activation states and/or localization, i.e., functional marker PPIs (fmPPIs), in the human kinome dendrogram (n = 82 kinase groups). (B) The 32 pathway and process terms that we associated with high confidence kiCCA interactors, including the number of members. (C) Correlation of log2 mRNA intensity (CCLE data) and log2 MS intensity differences of high confidence kiCCA interactors and protein kinases between the mesenchymal-like SNU761 and the epithelial-like HuH-7 hepatocellular carcinoma (HCC) lines. (D) Box plots of MS intensity ratios of high confidence kiCCA interactors with significant abundance differences between SNU761 and HuH-7 cells (Student's t-test BH-FDR < 0.05, n = 22). Every dot represents a kiCCA interactor, and interactors were grouped by their association with 32 representative gene ontology-biological process (GOBP) terms (see Table S3, Tabs 'Pathway Associations' and 'GOBP Search Strings'). Significant enrichment of interactor associated GOBP terms in either cell line was determined using a hypergeometric test and significant terms marked with an asterisk (* p < 0.1, ** p < 0.01, *** p < 0.001). The 29 of 32 plotted GOBP terms had interactors which changed in abundance. (E) Gene set enrichment analysis (GSEA) of proteins expressed in SNU761 compared to HuH-7 cells using our kiCCA Student's t-test data (see (D) and Methods).

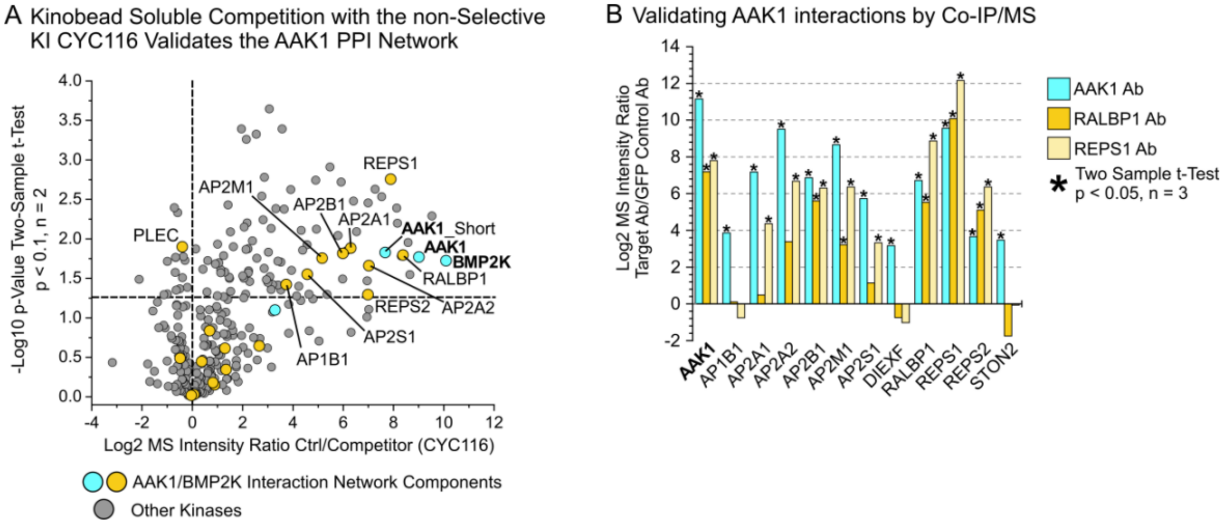

Figure S2.7. Validating the composition of the AAK1 interactome. Related to Figure 2.5. (A) Kinobead competition data using the KIP CYC116 in FOCUS cell lysate, showing competition of AAK1 and BMP2K and their putative interaction partners, as well as dozens of unrelated kinases (two sample t-test, p < 2, n = 2) (B) Co-IP/MS experiments in FOCUS cell lysate using specific antibodies targeting AAK1, RALBP1, and REPS1, validating the composition of an AAK1 interaction network identified by kiCCA (two sample t-test, p < 0.05, n = 3).

A Validating RNAi mediated knockdown of AAK1 complex components using qPCR analysis of target transcripts

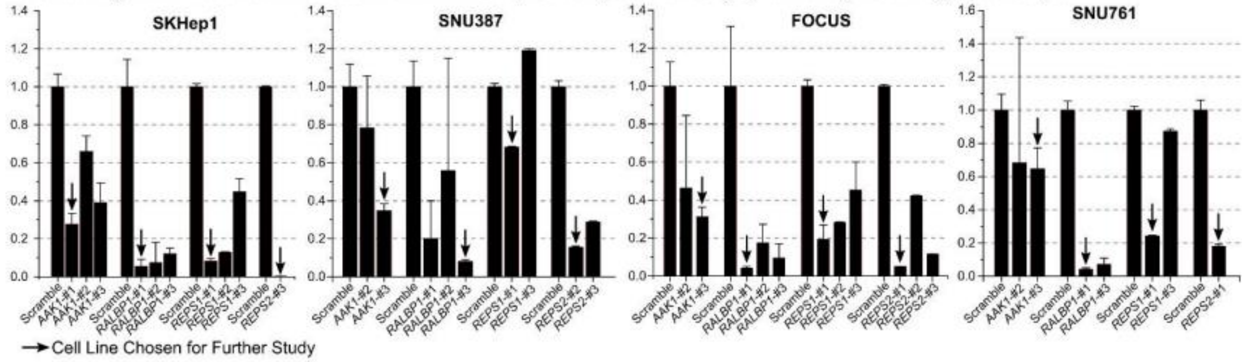

B Validating RNAi of AAK1 complex components using immunoblot analysis

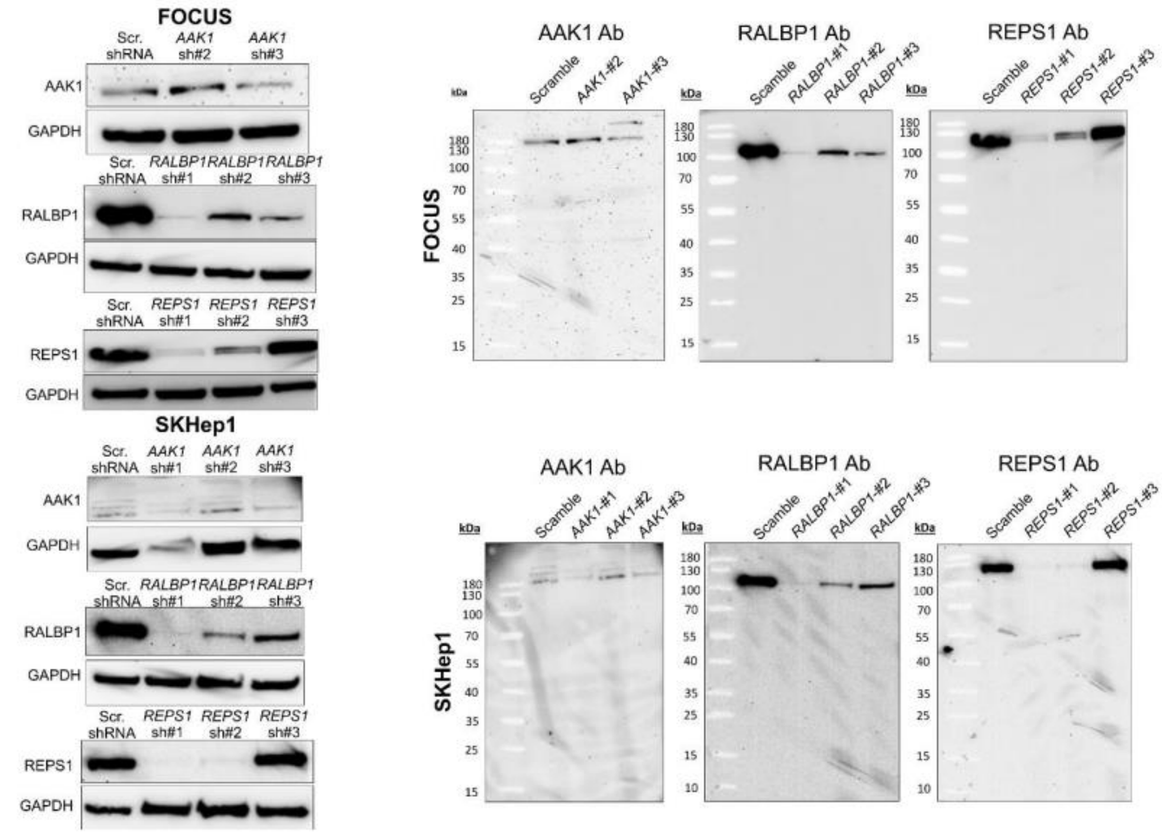

Figure S2.8. Validating AAK1 complex RNAi knockdown in FOCUS, SKHep1, SNU761, and SNU387. Related to Figure 2.5. (A) qPCR analysis of AAK1 complex RNAi lines, validating successful knockdown. (B) Immunoblot analysis of AAK1 complex RNAi lines, validating successful knockdown. REPS2 blots are not shown because the antibody used is likely not specific.

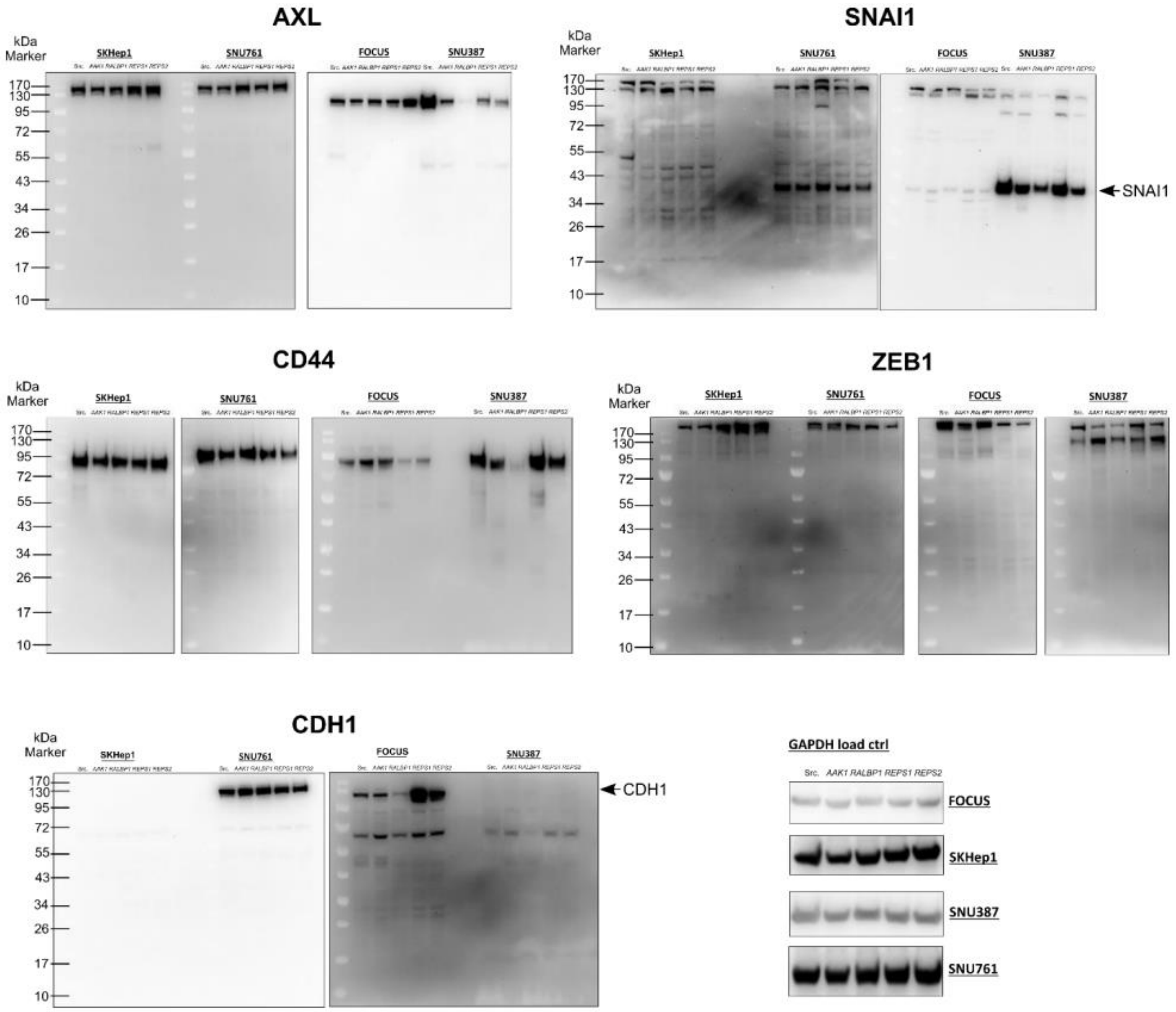

Figure S2.9. Immunoblot analysis of EMP marker expression in AAK1 complex RNAi cell lines. Related to Figure 2.5.

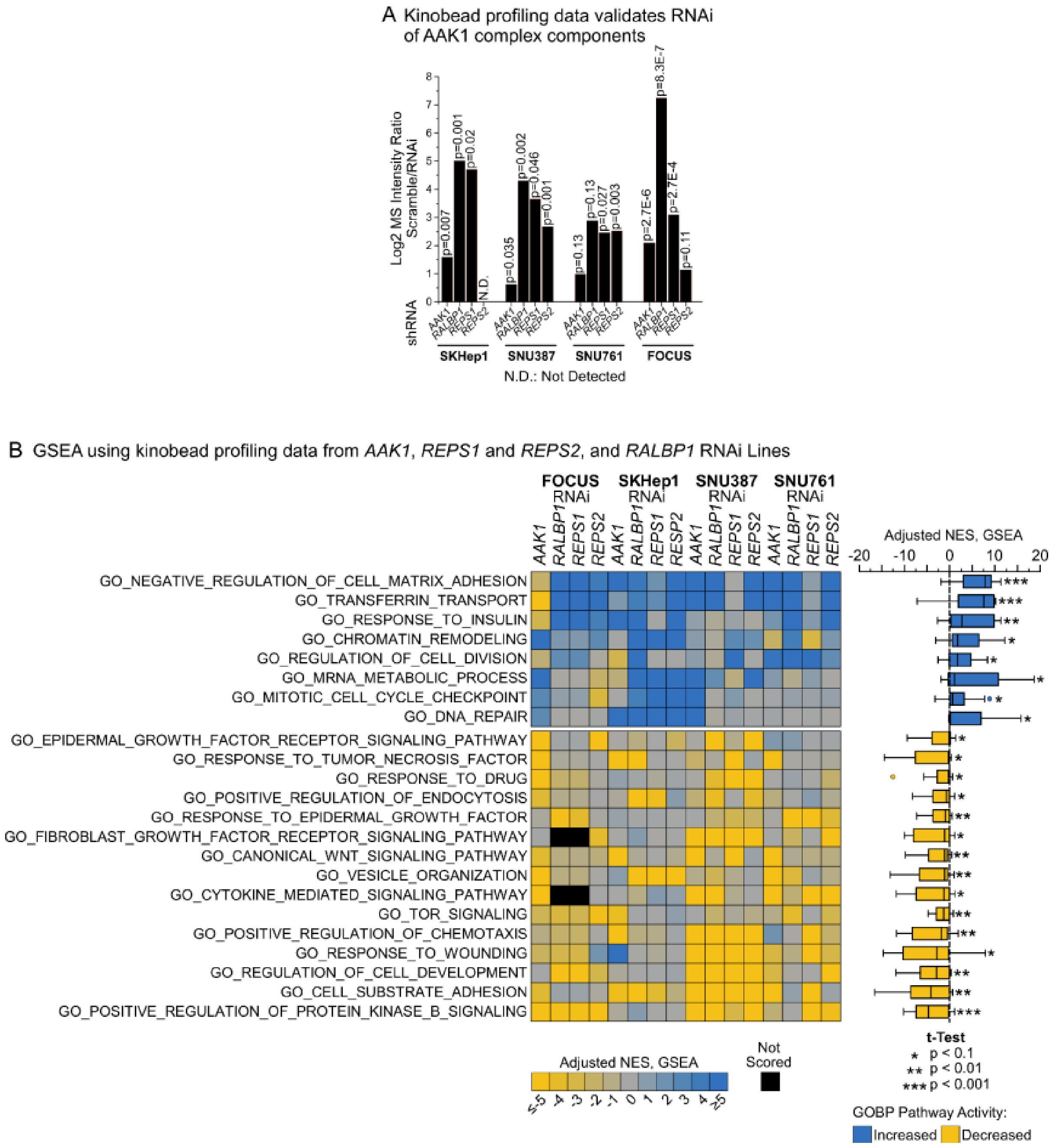

Figure S2.10. Kinobead/LC-MS analysis of AAK1 complex RNAi lines validates target knockdown, following GSEA identifies signaling pathways associated with each RNAi target. Related to Figure 2.5. (A) Kinobead/LC-MS analysis of AAK1 complex RNAi lines, validating successful knockdown. (B) GSEA pathway analysis of AAK1 complex RNAi lines using GOBP terms (Methods).

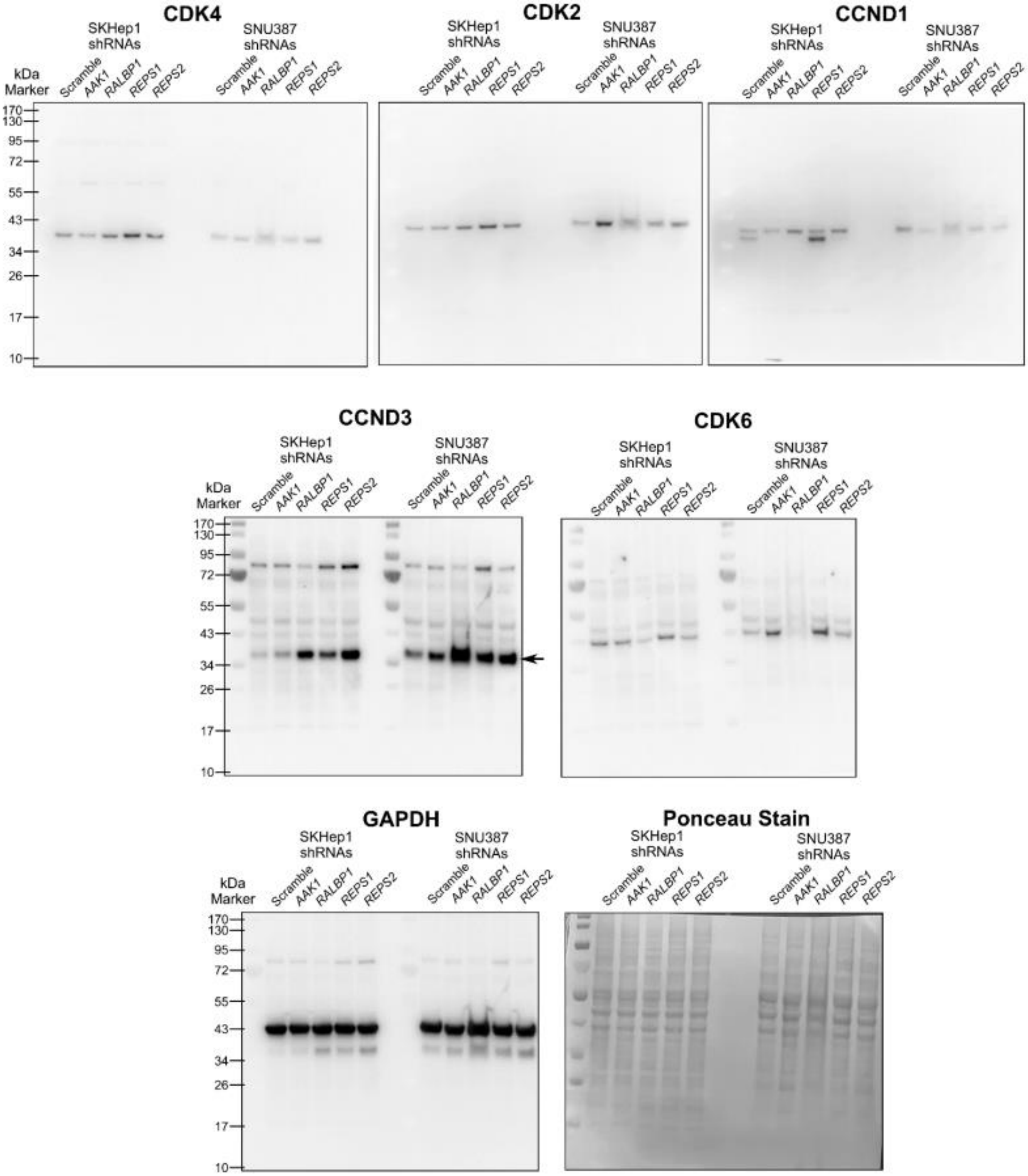

Figure S2.11. Immunoblot analysis of cell cycle marker expression in AAK1 complex RNAi cell lines. Related to Figure 2.5.

Chapter Three: Nuclear AAK1 promotes epithelial-mesenchymal transition in hepatocellular carcinoma

3.1. Introduction

Epithelial-mesenchymal transition (EMT) is a reversible process in which cells lose epithelial phenotypes, such as a cobblestone-like appearance, apical-basal polarity, fast proliferation and low migratory capacity, and gain mesenchymal phenotypes, such as a spindly appearance, front-to-back polarity, slow proliferation and high migratory capacity. EMT is known to be involved in normal processes in the cell, such as embryogenesis and wound healing, and the development of pathological conditions such as fibrosis and cancer. Multiple studies have linked EMT to therapeutic resistance and metastatic tendency, the hallmarks of cancer malignancy.[2, 7] Both drug resistance and metastasis are common in hepatocellular carcinoma (HCC), the most common type of liver cancer and a leading cause of cancer deaths worldwide. Thus, targeting EMT may overcome key challenges in improving HCC patient prognoses.

We previously used a mass spectrometry (MS)-based proteomics approach to comprehensively characterize protein kinases pathways that are associated with EMT in HCC cell lines.[105] We showed that high expression of well-known EMT markers, such as *SNAI2*, typically correspond to poor response to drugs and high migratory capacity in HCC cell lines, which are metrics for cancer drug resistance and metastasis, respectively. Based on these phenotypes, we classified HCC cell lines as being more mesenchymal- or epithelial-like.[63, 105] More recently, we developed an MS-based chemoproteomics method to characterize protein-protein interaction (PPI) networks of protein kinases in native cells and tissues, which we called kinobead competition and correlation analysis (kiCCA).[63] Using kiCCA, we compared PPI networks between mesenchymal- and epithelial-like HCC lines based on the classification that we had previously established and found that the adaptor-associated kinase 1 (AAK1) and its interaction partners are highly enriched in mesenchymal-like HCC cell lines.[63]

In the literature, AAK1 has a well characterized role in Clathrin-mediated endocytosis (CME) through the phosphorylation of the adaptor protein 2 (AP2) protein complex subunits. In fact, all known Ark1/Prk1 kinases (also known as Numb-associated kinases, or NAKs), the protein family in which AAK1 is a member, are involved in endocytosis.[24] Interestingly, AAK1 knockdown was previously shown not to affect AP2 phosphorylation or endocytosis.[30] In contrast, we showed that the knockdown of AAK1 reversed EMT in mesenchymal-like HCC cell lines, which suggests that AAK1's role in HCC EMT may be unique and not shared with other members of its family.[63] Here, we reported additional cellular phenotypes that are affected by the knockdown of AAK1 and showed that these changes are mirrored by the knockdown of the nuclear protein U3 small nucleolar RNA-associated protein 25 homolog (UTP25), one of AAK1's putative interaction partners. Moreover, our investigation of AAK1's relationship with UTP25 led to the discovery of an uncharacterized AAK1 isoform in the nucleus, which has never been reported and possibly underlies AAK1's role in HCC EMT.

3.2. Results

3.2.1. Proteomics experiments reveal UTP25 as a putative AAK1 interactor

UTP25 is an understudied nucleolar protein. In the literature, it has been connected to the maturation of the ribosome small subunit (SSU) processome and the stability of the tumor suppressor p53.[68-70, 73, 74] We first identified UTP25 as a putative AAK1 interactor in several HCC cell lines using kiCCA.[63] Before this, AAK1 was identified as UTP25's interactor on the PPI database BioGRID, in which epitope-tagged UTP25 was used as bait in an immunoprecipitation-mass spectrometry (IP-MS) experiment in 293T cells.[87] To validate the relationship between AAK1 and UTP25 in an endogenous context, we performed an IP-MS experiment in FOCUS, a mesenchymal-like HCC cell line, using endogenous AAK1 antibody. We showed that UTP25 was significantly enriched by AAK1 antibody, relative to control (Figure 3.1A).

As orthogonal validation, we also performed a kinobead competition experiment in the presence of the specific AAK1 inhibitor LP-935509 in SNU761, another mesenchymal-like HCC cell line. Kinobeads are kinase affinity reagents that are made of kinase inhibitors immobilized on sepharose beads. This reagent can enrich kinases, which are typically underrepresented in proteomics studies, along with their interactors. A specific kinase inhibitor competes for the binding of its target kinase and its interactors to kinobeads, and this de-enrichment can be detected using MS analysis. We showed that UTP25 was significantly de-enriched from kinobeads in the presence of 1uM LP-935509 compared to DMSO control, further supporting the relationship between AAK1 and UTP25 (Figure 3.1B). On the other hand, UTP25 was not detected in an IP-MS experiment using antibody against other AAK1 PPIs, RalA binding protein 1 (RALBP1) and RalBP1-associated Eps domain-containing protein 1 (REPS1) (Figure S2.7).[63]

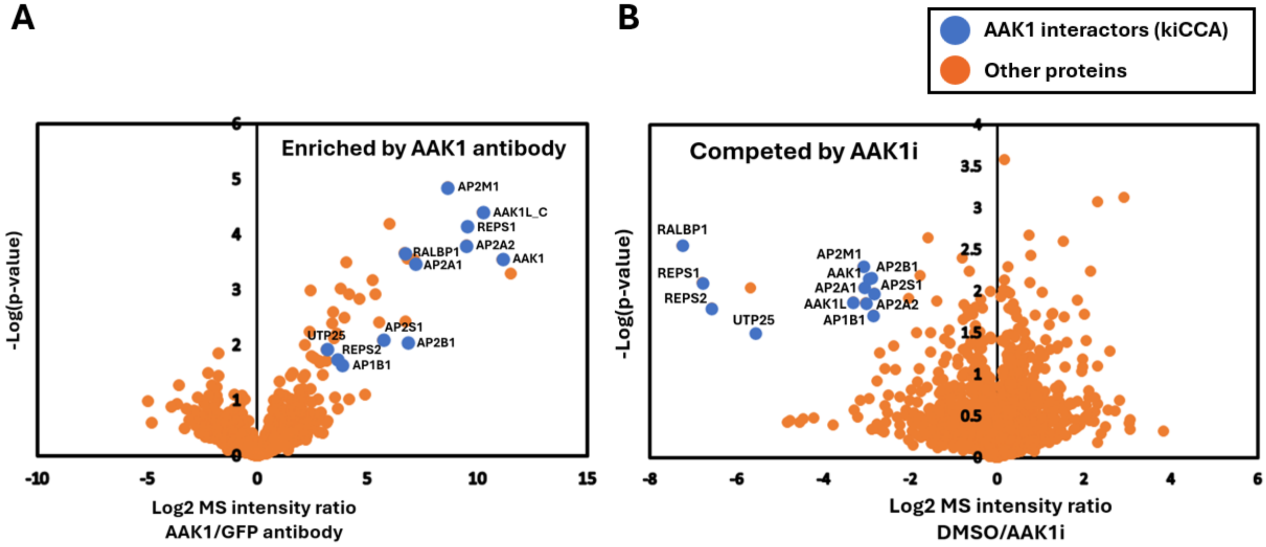

Figure 3.1. UTP25 is a putative AAK1 interactor. A) UTP25 was significantly enriched from FOCUS cell lysates in an IP-MS experiment using endogenous AAK1 antibody. GFP antibody was

used as negative control. B) UTP25 was significantly de-enriched from SNU761 lysates in the presence of 1uM of specific AAK1 inhibitor, LP-935509 (IC_{50} = 3.3 nM; K_i = 0.9 nM). DMSO was used as negative control. p-values were determined using Student's t test, and statistically significant hits are represented by y-axis values > 1.30.

3.2.2. AAK1 and UTP25 knockdown dramatically altered various cellular phenotypes

To investigate UTP25's role in HCC EMT, we stably expressed UTP25 shRNA knockdown in FOCUS (Figure S3.1). The FOCUS cell line with stable expression of AAK1 shRNA knockdown was previously generated (Figure S3.1).[63] We observed that both AAK1 and UTP25 knockdowns dramatically altered cell morphology, which further suggested a relationship between the two proteins (Figure 3.2A). To figure out if knockdown of UTP25, like AAK1, affected EMT phenotypes, we quantified changes in the expression of mesenchymal and epithelial marker genes upon knockdown, compared to a Scramble shRNA control, using real-time PCR (qPCR) analysis. We showed that both knockdowns of AAK1 and UTP25 significantly decreased the expression of mesenchymal marker genes, such as *SNAI2* and *MMP2* (Figure 3.2B, *top*), and significantly increased the expression of epithelial marker genes, such as *CDH1* and *EPCAM* (Figure 3.2B, *bottom*).

We also observed that both AAK1 and UTP25 knockdowns significantly increased cell proliferation, which we quantified using the CyQUANT™ Cell Proliferation Assay, a fluorescence-based assay that used a non-toxic, cell membrane permeant DNA dye (Figure 3.2C, *top*). Next, we asked if the increase in proliferation corresponds to any particular stage of the cell cycle. To do this, we fixed cells and added the FxCycle™ Violet Stain, then performed flow cytometry to compare the proportion of cells in different cell cycle stages based on their DNA content. We showed that there was a significant decrease in the proportion of cells in the G0/G1 phase (Figure 3.2C, *bottom*). This is consistent with our previous finding that cyclin D and the cyclin dependent kinases 2 and 6 (CDK2 and CDK6, respectively) were upregulated upon AAK1 knockdown, as these proteins are known to regulate cells' transition from G1 to S phase of the cell cycle.[63]

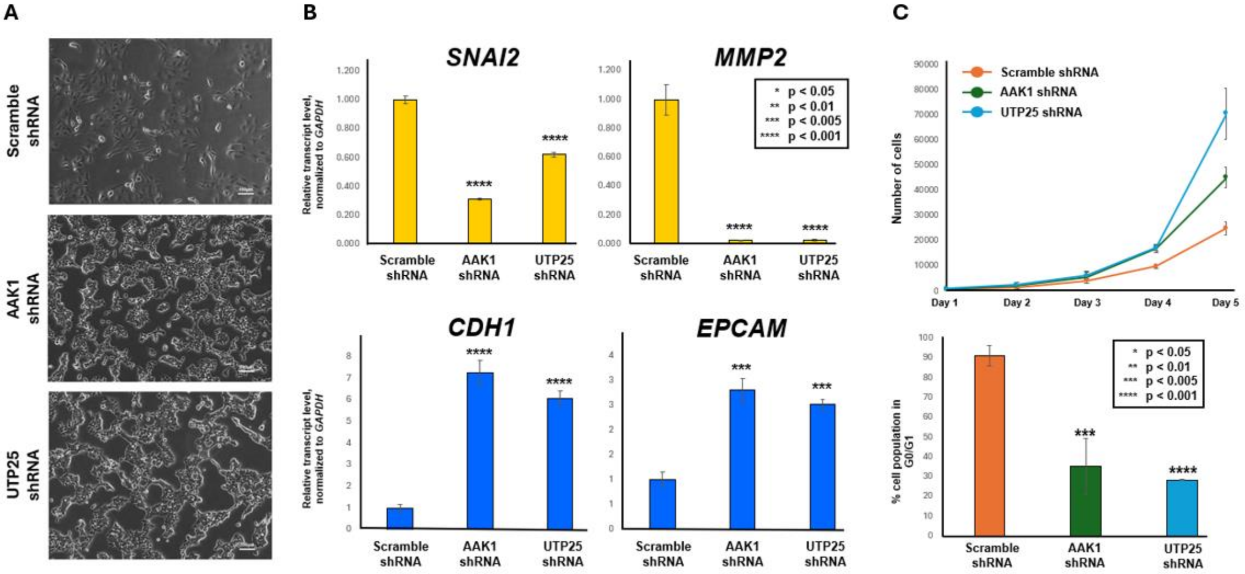

Figure 3.2. Knockdowns of AAK1 and UTP25 promote EMT reversal. (A) AAK1 and UTP25 knockdown dramatically altered cell morphology. Phase contrast images were taken using a widefield microscope at 10X objective magnification. Scale bar represents 100 µm. (B) AAK1 and UTP25 knockdowns significantly decreased the expression of mesenchymal markers (*top*) and epithelial markers (*bottom*). *GAPDH* was used as housekeeping control gene. Reported values are averages from three biological and two technical replicates, and error bars represent standard error. (C) AAK1 and UTP25 knockdowns significantly increased cell proliferation (*top*) and decreased the population of cells in the G0/G1 phase of the cell cycle (*bottom*). For cell proliferation assay, standard curves were generated for each cell line to determine number of cells. Measurements were taken every 24 hours. Reported values are averages from three biological and three technical replicates, and error bars represent standard deviation. For cell cycle assay, reported values are averages from three biological replicates and two technical replicates, and error bars represent standard deviation. *$p < 0.05$, **$p < 0.01$, ***$p < 0.005$, ****$p < 0.001$ by Student's t test.

We previously showed that knockdowns of AAK1 and REPS1 reduced cells' resistance to treatment with cell cycle checkpoint inhibitor drugs and led to the upregulation of cell cycle proteins that regulate the G1-to-S transition (Figure 2.5F).[63] However, unlike the AAK1 and UTP25 knockdown lines, the REPS1 knockdown line had similar proliferation rate relative to Scramble control (Figure S3.2A). Thus, we sought possible explanation for why cell proliferation dramatically increased upon knockdowns of AAK1 and UTP25, but not AAK1's other interaction partners.

In the literature, UTP25's is known to mediate p53's degradation in a ubiquitin-proteasome pathway-independent manner.[73, 74] Consistent with these reports, we found that the knockdown of UTP25 increased p53 expression, both on the protein and mRNA transcript levels (Figure 3.3A). Interestingly, we showed that knockdown of AAK1 also affected p53 levels similarly—AAK1's relationship with p53 has never been described (Figure 3.3A). Moreover, like the increase in cell proliferation, the effect of AAK1 and UTP25 knockdowns on p53 level was not observed upon knockdowns of other AAK1 interactors (Figure S3.2B). In addition to p53, we also showed that the expression of other tumor suppressors, such as ataxia-telangiectasia mutated (*ATM*) and checkpoint kinase 2 (*CHEK2*), were significantly upregulated upon AAK1 and DIEXF knockdowns (Figure 3.3B).

p53 can promote apoptosis, and apoptosis-induced proliferation (AiP), a compensatory increase in proliferation due to apoptosis, is known to occur in HCC.[150] Thus, we considered AiP as an alternative explanation for the observed increase in proliferation upon AAK1 and UTP25 knockdowns. To quantify the proportion of apoptotic cells, we performed annexin V staining followed by flow cytometry analysis. Annexin V binds to phosphatidyl serine that has translocated from the inner to the outer leaflet of the plasma membrane—this translocation occurs in cells that are undergoing apoptosis. Fluorophore-conjugated annexin V allows populations of apoptotic cells to be detected using flow cytometry analysis. Using this assay, we showed that knockdowns of AAK1 and UTP25 significantly reduced the proportion of apoptotic cells relative to scrambled shRNA control (Figure 3.3C). This indicated that the increase in cell proliferation upon AAK1 and UTP25 knockdowns did not occur through AiP. Rather, these results suggest that upon AAK1 and

UTP25 knockdowns, cells gain better control of the cell cycle and undergo significantly less apoptosis, and these ultimately lead to higher cell proliferation rate.

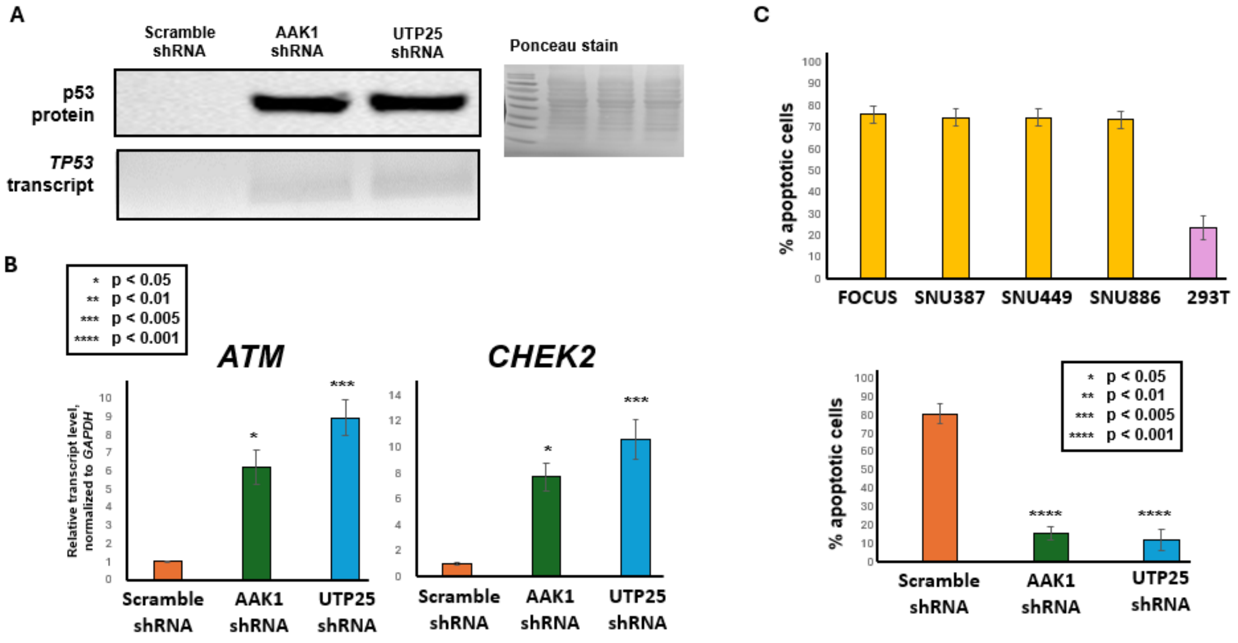

Figure 3.3. Knockdowns of AAK1 and UTP25 increased cell cycle control and reduced apoptosis. (A) AAK1 and UTP25 knockdowns increased p53 protein (Western Blot, *top*) and mRNA transcript levels (1% agarose gel, *bottom*). *TP53* transcript was amplified using primers flanking exons 5 and 8. (B) AAK1 and UTP25 knockdowns significantly increased mRNA transcript levels of tumor suppressor genes *ATM* and *CHEK2*. *GAPDH* was used as housekeeping control gene. Reported values are averages from three biological and two technical replicates, and error bars represent standard error. (C) AAK1 and UTP25 knockdowns significantly decreased annexin V-positive cells, which indicate apoptosis. Top panel showed that apoptosis rates are high in HCC cell lines, which is known, compared to 293T cells, for instance. Reported values are averages from three biological and two technical replicates, and error bars represent standard deviation. *$p < 0.05$, **$p < 0.01$, ***$p < 0.005$, ****$p < 0.001$ by Student's t test.

3.2.3. An AAK1 isoform is found in the nucleus

The possibility of AAK1 and UTP25 sharing a biological role is even more intriguing given the distinction in their known cellular localizations: the cytosol versus the nucleus, respectively. We showed that AAK1 may be involved in the cell cycle and affect the stability of tumor suppressors; thus, we wanted to know if AAK1 could be present in the nucleus. We performed immunofluorescence (IF) microscopy using endogenous AAK1 antibody. Unfortunately, we were unable to obtain robust images due to the quality of the commercially available antibody (Figure S3.3A). To circumvent this, we performed subcellular fractionation followed by Western blotting, comparing the FOCUS AAK1 shRNA knockdown line to the Scramble shRNA control. We showed that AAK1 was not only present in the cytosol, as expected, but also in the nucleus (Figure 3.4B).

We used GRB2, the Na/K ATPase, Lamin A/C and Histone H3 as subcellular markers for the cytosolic, plasma membrane, nucleoplasmic and chromatin-bound fractions, respectively, to indicate the successful enrichment for each compartment. Surprisingly, although we didn't not any visible defect or abnormality on the nuclear structure, we found that the level of Lamin A/C in cells was dramatically reduced upon AAK1 knockdown (Figure 3.4B). This dramatic reduction of Lamin A/C was similarly observed upon UTP25 knockdown (Figure 3.4C).

We observed the presence of three different isoforms of AAK1 at 863-, 961- and 1131-amino acid lengths, or the short ("AAK1S"), medium ("AAK1M") and long ("AAK1L") isoforms, respectively. Both AAK1S and AAK1M have been reported in the literature,[22, 65] and we previously detected AAK1L in several MS proteomics experiments. We showed that AAK1K is the predominantly expressed form in FOCUS, and there seemed to be a strong isoform-specific preference for nuclear localization (Figure 3.4B). We also showed that upon knockdown, the amount of AAK1 is notably reduced in both the cytosol and the nucleus (Figure 3.4B). Furthermore, this reduction was near-complete in the nucleus, suggesting that nuclear AAK1L may be responsible for the strong EMT phenotypes in HCC (Figure 3.4B). We observed the strong preference for AAK1L to reside in the nucleus, compared to other isoforms, even when extra lysate was loaded (Figure S3.4).

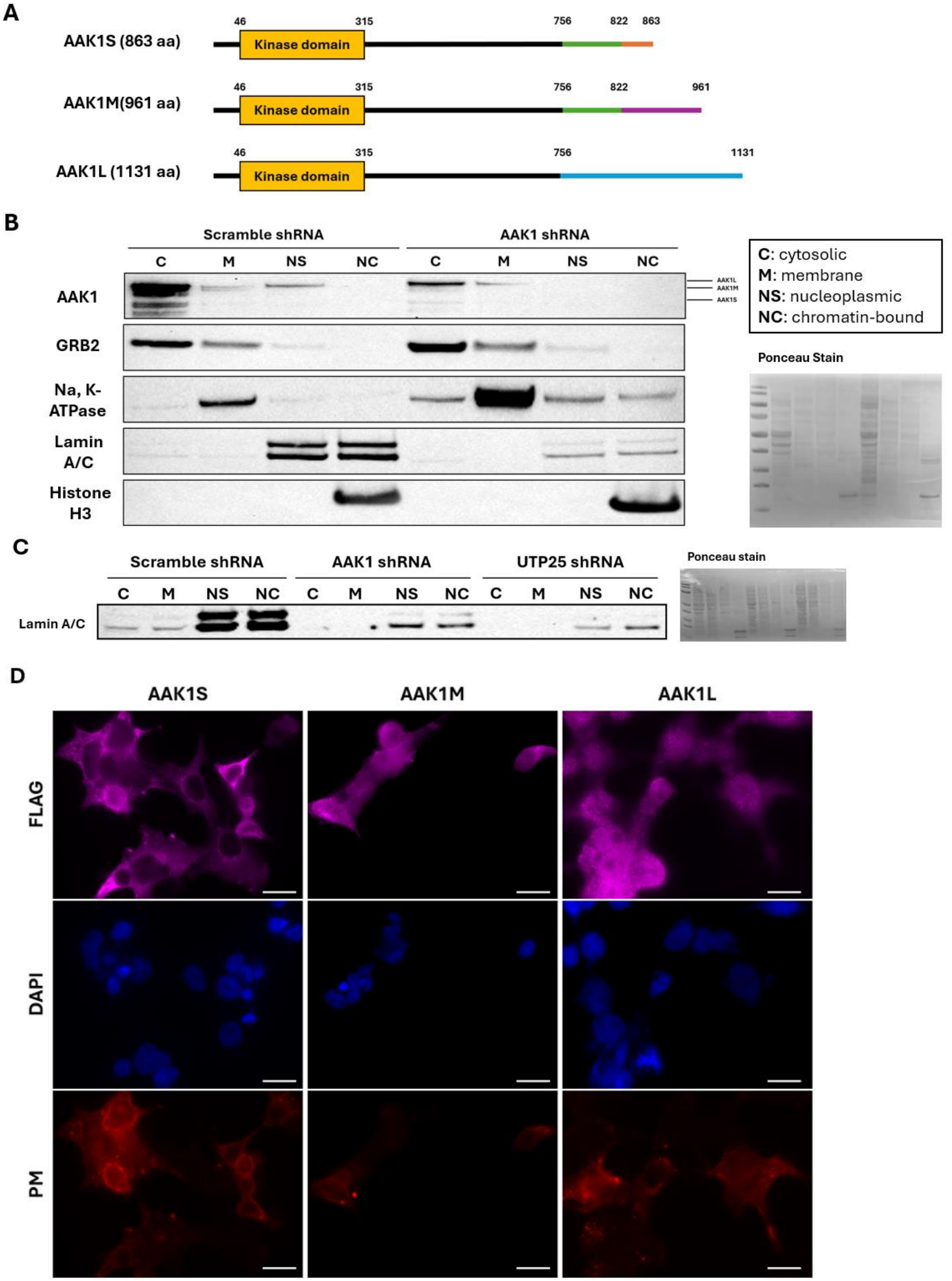
A
AAK1S (863 aa)
46
315
756
822
863
Kinase domain
AAK1M(961 aa)
46
315
756
822
961
Kinase domain
AAK1L (1131 aa)
46
315
756
1131
Kinase domain
B
Scramble shRNA
AAK1 shRNA
C
M
NS
NC
C
M
NS
NC
AAK1
AAK1L
AAK1M
AAK1S
GRB2
Na, K-ATPase
Lamin A/C
Histone H3
C: cytosolic
M: membrane
NS: nucleoplasmic
NC: chromatin-bound
Ponceau Stain
C
Scramble shRNA
AAK1 shRNA
UTP25 shRNA
C
M
NS
NC
C
M
NS
NC
C
M
NS
NC
Lamin A/C
Ponceau stain
D
AAK1S
AAK1M
AAK1L
FLAG
DAPI
PM

Figure 3.4. AAK1 is present in the nucleus. (A) Simplified diagram of AAK1 isoforms. (B) Subcellular fractionation experiment separated cells into cytosolic (C), membrane (M), nucleoplasmic (NS) and chromatin-bound (NC) fractions. Protein concentrations were determined by generating standard curves using extraction buffers for each corresponding fraction, and 15ug of protein was loaded onto each lane. Growth factor receptor-bound Protein 2 (GRB2), Na,K-ATPase, lamin A/C and histone H3 proteins were used as C, M, NS and NC fraction markers to indicate successful enrichment. (C) Subcellular fractionation experiment was performed in FOCUS Scramble, AAK1 and UTP25 shRNA lines as described in (B). Lamin A/C levels were reduced upon AAK1 and UTP25 knockdown. (D) Immunofluorescence (IF) microscopy image of HEK293T cells transiently transfected with FLAG-tagged AAK1 isoforms. Cells were stained with anti-FLAG antibody, and images were obtained using 1,000X oil objective magnification. Scale bar represents 10um.

To further confirm the isoform specificity of AAK1 nuclear localization while circumventing the issue with antibody targeting endogenous AAK1, we transiently overexpressed FLAG-tagged AAK1S, AAK1M and AAK1L in 293T cells and performed IF microscopy using anti-FLAG antibody. We showed that AAK1S was largely excluded in the nucleus, while the longer isoforms, especially AAK1L, were present throughout the cell, including the nucleus, which was consistent with our findings in the endogenous context.

3.3. Discussion

We showed that RNAi knockdown of AAK1 and UTP25 in a mesenchymal-like HCC cell line produced similar phenotypes, and these phenotypes that are consistent with the reversal of EMT, or mesenchymal-epithelial transition (MET). We observed knockdown of AAK1 and UTP25 notably upregulated the expression of tumor suppressor proteins such as P53, ATM, and CHEK2. In addition, we demonstrated that these knockdowns significantly reduced apoptosis—apoptosis rate is known to be high in HCC.[117] We showed that these promoted a G1-to-S progression in the cell cycle and an increase in cell proliferation rate.

We found that many of the phenotypes that resulted from AAK1 and UTP25 knockdown were not observed when we knockdown other AAK1 PPIs. Furthermore, through affinity purification-mass spectrometry (AP-MS) analysis, we found that UTP25 was only enriched when cell lysates were pulled down using antibody against AAK1, but not other AAK1 PPIs like RALBP1 or REPS1.[63] Furthermore, we showed that knockdowns of AAK1 and UTP25 affected the mRNA transcript level expression of other AAK1 PPIs, particularly RALBP1, REPS1 and AP2M1, but not the other way around. AAK1 knockdown also significantly decreased the transcript level expression of UTP25, and vice versa. We thought that this could explain, at least partially, the strong phenotypic connection that they shared.

We hypothesized that the distinction between AAK1's relationship with UTP25 and the other PPIs may be regulated spatially, so we tested whether AAK1 was present in the nucleus. While investigating AAK1's nuclear localization, we unexpectedly observed that the expression level of the nuclear structural protein lamin A/C was dramatically reduced upon AAK1 and UTP25 knockdown. Although we did not observe a visible nuclear structure defect or abnormality in our model cell line, with or without knockdown, we thought that this dramatic effect on lamin A/C could explain some of the phenotypic effects of AAK1 and UTP25 knockdown.

For instance, we showed that AAK1 and UTP25 knockdown significantly upregulated cell proliferation. These knockdowns also significantly affected the transcript level expression of different proteins, including other AAK1 PPIs and EMT marker proteins. As structural proteins in the nucleus, lamins have been implicated in various nuclear functions, such as cell proliferation and gene transcription.[151-154] Lamin has also been linked to EMT in other cancers, such as prostate and lung cancer.[155-157] This further our hypothesis that AAK1 and UTP25 role in promote EMT, and that their depletion could drive MET.

We also observed that AAK1's nuclear localization may be isoform-specific, as we saw that only AAK1L, and possibly AAK1M, but not AAK1S, resides in the nucleus. Both AAK1S and AAK1M have been previously characterized in the literature, and both isoforms reportedly play comparable roles in CME.[22, 65] Interestingly, searching the isoforms' sequences onto cNLS mapper, an online tool used to predict and map putative nuclear localization signals (NLS) revealed the most high-scoring putative NLS at amino acid residues 367-396, which were shared between all isoforms.[158-160] However, cNLS mapper also revealed another high-scoring putative NLS at amino acid residues 1058-1091 on AAK1L, which is not shared with the other isoforms.[158-160] This could be a starting point in future explorations of AAK1's isoform-specific nuclear localization. Another possibility is that AAK1L, and possibly AAK1M, relies on another protein to shuttle it to the nucleus, in which case their interaction with this protein, like their nuclear localization, will also show a similar isoform-specific preference.

The three AAK1 isoforms we reported in this study share an identical kinase domain, between amino acid residues 46 and 315. AAK1's N-terminal kinase domain is also known to be relatively well conserved among all NAKs and is important for the regulation of CME.[24] For this reason, we believe that AAK1's isoform-specific differences, such as its nuclear localization, may be independent from its kinase activity and functionally distinct from its established role in CME. Future studies will characterize functional distinctions between the AAK1 isoforms with regards to its role in EMT, relationship with UTP25, nuclear localization and beyond.

3.4. Materials and methods

Cell lines and tissue culture conditions

SNU761 was purchased from the Korean Cell Line Bank (KCLB). FOCUS WT cells were obtained from the Laboratory of J. Wands, Brown University.[121] All cells were grown at 37°C under 5% CO2, 95% ambient atmosphere. Fifteen cryo-frozen cell stocks were generated from the original vial from the cell bank or from the collaborator's lab (passage 3). Experiments were performed with cells at <10 passages from the original vial. All cell media used were supplemented with 100x penicillin-streptomycin-glutamine (Thermo Fisher Scientific, Waltham, MA). FOCUS cell lines were grown in Dulbecco's minimum essential medium (DMEM) supplemented with 10% FBS (VWR Life Science, Seradigm). SNU761 was grown in RPMI 1640 medium supplemented with 10% FBS. SH-SY5Y were cultured in DMEM supplemented with 10% FBS. Cells were harvested when reaching 90% confluency.

RNA interference (RNAi) knockdown experiments

Three short hairpin RNA (shRNA) sequences targeting *UTP25* mRNAs were obtained from The RNAi Consortium (TRC) of the Broad Institute web portal (https://www.broadinstitute.org/rnai-consortium/rnai-consortium-shrna-library, ID Numbers: TRCN0000271511, TRCN0000271465, TRCN0000271513) and cloned into the lentiviral pLKO.1 vector (Plasmid#10878, Dr. David Root's Lab, Addgene, Watertown, MA) as previously described.[147] Lentiviral particles were produced from individual pLKO.1 vectors, the pMD2.G plasmid (envelope, plasmid #12259, Didier Trono, Addgene), and the pCMVR8.74 plasmid (packaging, plasmid #22036, Didier Trono, Addgene) according to the manufacturer's instructions (Addgene). Virus particle-containing cell culture supernatants were sterile filtered over 0.22 µM PES syringe filters (Millex-GP, Sigma Millipore, Burlington, MA), mixed 1:1 with fresh growth medium, 8 µg/mL final polybrene was added and the mixture added to target cells (70–80% confluency). Cells were incubated for 24h, the medium exchanged, and stable cell lines selected using puromycin (1 µg/mL) 5-7 days. Puromycin-resistant cells were maintained in growth medium containing half of the selection concentration of puromycin. Target knockdown was validated using quantitative real-time PCR (qPCR) and the stable cell line with the highest knockdown among the three shRNAs was chosen to perform all downstream experiments.

Real-time PCR (qPCR) analysis of mRNA expression

qPCR analysis was performed to validate and quantify 1) target mRNA expression upon shRNA knockdown and 2) changes in the mRNA expression of EMT marker and tumor suppressor genes. Briefly, cells were cultured on 35mm dishes until reaching 80–90% confluency and total mRNA was isolated using the TRIzol reagent according to manufacturer's instructions (Thermo Fisher Scientific). 0.5 µg of total RNA was used to generate first-strand cDNA using the Protoscript II First Strand cDNA Synthesis Kit (New England Biolabs, Ipswich, MA). The resulting cDNA was subjected to qPCR using human gene-specific primers for *UTP25*, *SNAI2*, *MMP2*, *CDH1*, *EPCAM*, *ATM* and *CHEK2*, and *GAPDH* as housekeeping control gene. The qPCR reaction was performed using QuantStudio 5 Real-Time PCR System (Applied Biosystems, Thermo Fisher Scientific) using the following program:

Step	**Temp (°C)**	**Time (mm:ss)**	**Cycles**
Hold (enzyme active)	50, 95	02:00, 10:00	1
PCR (denature, anneal, extend)	95, 50, 60	00:15, 00:15, 01:00	50
Dissociation / melting curve	95, 60, 95	00:15, 01:00, 00:15	5

The mRNA levels of each gene were normalized relative to the mean levels of the housekeeping gene and compared with the data obtained from cell lines carrying a stably incorporated scrambled shRNA control using the $2^{-\Delta\Delta Ct}$ method. According to this method, the normalized level of a mRNA, X, is determined using the following equation:

$$X = 2^{-Ct(GOI)}/2^{-Ct(CTL)}$$

where Ct is the threshold cycle (the number of the cycle at which an increase in reporter fluorescence above a baseline signal is detected), GOI refers to the gene of interest, and CTL refers to a control housekeeping gene. This method assumes that Ct is inversely proportional to the initial concentration of mRNA and that the amount of product doubles with every cycle.

Immunoprecipitation-mass spectrometry (IP-MS) analysis sample preparation

Cells grown in 60mm dishes (90% confluency) were lysed in 200 µL of cell lysate in modified RIPA buffer V1 (50 mM Tris-HCl, 150 mM NaCl, 1% NP-40 (v/v), 0.25% Na-deoxycholate (w/v), 1 mM EDTA, 10 mM NaF, 5% glycerol (v/v), pH 7.8) containing HALT protease inhibitor cocktail (100x, Thermo Fisher Scientific, Waltham, MA) and phosphatase inhibitor cocktail II and III (100x, Sigma-Aldrich, St Louis, MO).). Protein concentration was quantified using the Piece 660 nm Protein Assay Reagent (Pierce, Rockford, IL), and all cell lysates were brought to 2mg/ml protein concentration. Lysates were incubated with antibody against AAK1 (CST, Cat #79832) or GFP (control, clone D5.1, CST, Cat #2956) at the manufacturer's recommended concentrations, respectively, and agitated overnight on a tube rotator at 4°C. The next day, Pierce Protein A Agarose (Thermo Fisher Scientific) was washed twice with ice-cold modified RIPA buffer V1 and 40 µL aliquots of a 50% bead slurry were added to each lysate/antibody mixture. The slurry was agitated for 3h on a tube rotator at 4°C, the supernatant was aspirated, and then the beads were washed twice with ice-cold modified RIPA buffer V1 and three times with TBS. Proteins were reduced, alkylated, and eluted by adding 100 µL denaturing buffer (8M urea, 5mM TCEP, 10mM CAM, 100 mM Tris pH 7.8) to beads and agitating them on a thermomixer at 1,400 rpm for 30 min at 37°C. The supernatant containing the protein was transferred to a new tube and diluted two-fold with 100 mM TEAB, and the pH was adjusted to 8.5 using 1N NaOH solution. 2 µg of Lys-C (Wako Chemicals) were added, and samples agitated on a thermo mixer at 1,400 rpm for 2 h at 37°C. Then, samples were diluted another two-fold with 100 mM TEAB and 2 µg of MS-grade trypsin (Thermo Fisher Scientific) were added. The mixture was agitated on a thermomixer at 1,400 rpm overnight at 37°C. The resulting peptide solution was acidified with formic acid to achieve pH <3 (1.5% FA final) and desalted using C18 StageTips according to the published protocol.[19] The experiments were performed using three biological replicates per antibody.

Kinobead soluble competition

Cells grown in 60mm dishes (90% confluency) were lysed in 150 µL of cell lysate in modified RIPA buffer V1 containing HALT protease inhibitor cocktail (100x, Thermo Fisher Scientific, Waltham, MA) and phosphatase inhibitor cocktail II and III (100x, Sigma-Aldrich, St Louis, MO). Protein concentration was quantified using the Piece 660 nm Protein Assay Reagent (Pierce, Rockford, IL), and all cell lysates were brought to 2mg/ml protein concentration. 1.5 µL DMSO (vehicle control) or 1µM of LP-935509 (AAK1 inhibitor) solution in DMSO (competition) were added to a final concentration 1% DMSO.[50] The lysates were vortexed at intermediate speed intermittently every 5 min for 20 min while being kept on ice. Meanwhile, 40 µl of a 50% slurry of the in-house-made, optimized kinobead mixture in 20% aq. ethanol were prepared for each pulldown experiment. The beads were washed twice with 400 µl modified RIPA buffer and lysates containing DMSO, or inhibitor were added. The mixture was incubated on a tube rotator for 3h at 4°C and then the beads were pelleted rapidly at 2000xg on a benchtop centrifuge (5s). After removal of the supernatant, the beads were rapidly washed twice with 400 µl of ice-cold mod. RIPA buffer and three times with 400 µl ice-cold tris-buffered saline (TBS, 50 mM tris, 150 mM NaCl, pH 7.8) to remove detergents. 100 µl of freshly prepared denaturing buffer (8M urea, 100 mM Tris, pH 8.5) containing 5 mM tris(2-carboxyethyl)phosphine hydrochloride (TCEP*HCl) and 10 mM chloroacetamide (CAM), were added and the slurry agitated on a thermomixer at 37°C and 1400 rpm for 30 min. The mixture was diluted 2-fold with 100 mM triethylamine bicarbonate (TEAB), the pH adjusted to 8–9 by addition 1 N aq. NaOH; 2 µg LysC were added, and the mixture agitated on a thermomixer at 1400 rpm at 37°C for 2 h. Then, the mixture was diluted another 2-fold with 100 mM TEAB, 2 µg MS-grade trypsin (Thermo Fisher Scientific, Waltham, MA) were added, and the mixture agitated on a thermomixer at 1400 rpm at 37°C overnight. Then, 6 µL of formic acid (FA) were added (1.5% FA final) to adjust to pH 3 and peptides were extracted and desalted using C18 StageTips according to the published protocol.[149] The experiments were performed using three biological replicates per condition.

nano liquid chromatography (LC)-MS analysis

LC-MS analyses were performed as described previously with the following minor modifications.[97, 106] Peptide samples were separated on an EASY-nLC 1200 System (Thermo Fisher Scientific) using 20 cm long fused silica capillary columns (100 µm ID, laser pulled in-house with Sutter P-2000, Novato CA) packed with 3 µm 120 Å reversed phase C18 beads (Dr. Maisch, Ammerbuch, DE). The LC gradient was 120 min long with 5–35% B at 300 nL/min. LC solvent A was 0.1% (v/v) aq. acetic acid and LC solvent B was 20% 0.1% (v/v) acetic acid, 80% acetonitrile. MS data was collected with a Thermo Fisher Scientific Orbitrap Fusion Lumos. Data-dependent analysis was applied using Top15 selection with CID fragmentation.

Computation of MS raw files

Data .raw files were analyzed by MaxQuant/Andromeda73 version 1.5.2.8 using protein, peptide and site FDRs of 0.01 and a score minimum of 40 for modified peptides, 0 for unmodified peptides; delta score minimum of 17 for modified peptides, 0 for unmodified peptides. MS/MS spectra were searched against the UniProt human database. MaxQuant search parameters: Variable modifications included Oxidation (M) and Phospho (S/T/Y). Carbamidomethyl (C) was a fixed modification. Max. missed cleavages was 2, enzyme was Trypsin/P and max. charge was 7. The MaxQuant “match between runs” feature was enabled. The initial search tolerance for FTMS scans was 20 ppm and 0.5 Da for ITMS MS/MS scans.

MaxQuant output data processing

MaxQuant output files were processed, statistically analyzed and clustered using the Perseus software package v1.5.6.0.[143] Human gene ontology (GO) terms (GOBP, GOCC and GOMF) were loaded from the 'mainAnnot.homo_sapiens.txt' file downloaded on 02.03.2020. Expression columns (protein intensities) were log2 transformed and normalized by subtracting the median log2 expression value from each expression value of the corresponding data column. Potential contaminants, reverse hits and proteins only identified by site were removed. Reproducibility between LC-MS/MS experiments was analyzed by column correlation (Pearson's r) and replicates with a variation of $r > 0.25$ compared to the mean r-values of all replicates of the same experiment (cell line or knockdown experiment) were considered outliers and excluded from the analyses. Data imputation was performed in Perseus using a modeled distribution of MS intensity values downshifted by 1.8 and having a width of 0.2.

Brightfield phase-contrast microscopy

100,000 cells were seeded onto each well of a 12-well plate and imaged using an inverted fluorescence phase contrast microscope (Keyence BZ-X710) at 10X objective magnification. The experiment was performed on three biological replicates.

Cell proliferation assay

CyQUANT™ NF Cell Proliferation Assay (Thermo Fisher Scientific) was used using the manufacturer's protocol. Briefly, for the time course, 1,000 cells were seeded into each well of a 96-well plate, and measurements were taken every 24 hours for 5 days. A separate plate was prepared for each measurement point on the time course. Standard curve measurements were taken at the same time as the first day measurements for the time course, after allowing cells to attach for several hours. Before measurements were made, growth medium was removed from each well and replaced with 100ul of 1X dye binding solution. Cells were incubated with the reagent for 1 hour at 37°C, protected from light. Fluorescence was quantified with a SpectraMax 190 plate reader (Molecular Devices, San Jose, CA) at 485nm excitation and 520nm emission. Six-point standard curves were generated for each cell line using two-fold serial dilutions starting from 20,000 cells. The experiment was performed using three biological and two technical replicates.

Cell cycle stage analysis

FxCycle™ Violet Stain (Thermo Fisher Scientific) was used using the manufacturer's protocol for flow cytometric analysis of DNA content in fixed cells and quantify the population of cells in different stages of the cell cycle. Briefly, 48 hours prior to the experiment, cells were starved by changing growth media supplemented with 10% FBS to media supplemented with 0.1% FBS in order to synchronize their cell cycle stages. Then, 24 hours later, the media was changed back to that supplemented with 10% FBS, and the cells were allowed to grow for 24 hours. For harvest, cells were trypsinized, then resuspended in growth medium supplemented with 10% FBS and counted. Next, the cell suspensions were centrifuged at 600xg for 5 minutes. The supernatants were removed, and pellets were re-suspended in PBS to 2E6 cells/ml concentration. 500µl of cells in PBS was pipetted into 1.2ml of cold 100% ethanol, then incubated at -20°C overnight. The next day, the ethanol-fixed cells were pelleted at 600xg for 5 minutes, washed twice with cold PBS, then resuspended in cold PBS to 1E6 cells/ml concentration. 1µl of FxCycle™ Violet Stain was added to 1ml of cell suspension, then cells were analyzed using flow cytometry. Flow rate was set to low, gates were set for singlets and 10,000 events were recorded per sample. The Watson pragmatic model on FlowJo was used to determine the populations of cells at different stages of the cell cycle. The experiment was performed on three biological replicates.

Immunoblot analysis and antibodies

Antibodies used for immunoblotting were anti-p53 (7F5, CST, Cat #2527), AAK1 (E8M3P, CST, Cat #61527), GRB2 (CST, Cat #3972), Na,K-ATPase (CST, Cat #3010), lamin A/C (4C11, CST, Cat #4777) and histone H3 (D1H2, CST, Cat #4499). Cell lysis and immunoblotting experiments were performed using standard procedures. Briefly, cells were rinsed twice with ice-cold phosphate buffered saline (PBS), lysed in modified RIPA buffer V1 (50 mM Tris-HCl, 150 mM NaCl, 1% NP-40 (v/v), 0.25% Na-deoxycholate (w/v), 1 mM EDTA, 10 mM NaF, 5% glycerol (v/v), pH 7.8) supplemented with HALT protease inhibitor (100x, Thermo Fisher Scientific, Waltham, MA), and lysates clarified by centrifugation at 21,000 rcf for 20 minutes at 4°C. Protein concentration was quantified using the Piece 660 nm Protein Assay Reagent (Pierce, Rockford, IL). Lysates were mixed with NuPAGE LDS Sample Buffer (4X, Thermo Fisher Scientific) containing 50 mM DTT and heated for 5 min at 95°C. 20 µg of protein was loaded onto each lane, and 5µl of Fisher BioReagents™ EZ-Run™ Prestained Rec Protein Ladder (Fisher Scientific) was used as molecular weight marker. Proteins were separated on Bolt 4–12% Bis-Tris Protein Gels (Thermo Fisher Scientific) and electro-transferred onto nitrocellulose membranes. Membranes were blocked with 5% BSA in TBS-T (50 mM NaCl, 150 mM Tris-HCl, 1% Tween-20, pH = 7.8) for 1 hour at room temperature, washed 4 times with TBS-T, then incubated with primary antibodies, diluted to the manufacturers' recommended concentrations in blocking buffer, overnight at 4°C. The next day, membranes were washed 4 times with TBS-T (50 mM NaCl, 150 mM Tris-HCl, 1% Tween-20, pH = 7.8), then incubated with anti-rabbit HRP conjugate, diluted 1:4000 in blocking buffer, for 1 hour at room temperature. Following secondary incubation, membranes were washed 4 times in TBS-T, and bands were visualized using the Clarity Western ECL Substrate (Bio-Rad, Hercules, CA) and the iBrightCL1000 imager (Life Technologies, A23749).

Annexin V apoptosis assay

Fluorochrome-conjugated annexin V stain (Thermo Fisher Scientific) was used following the manufacturer's protocol to quantify the population of cells undergoing apoptosis using flow cytometry analysis. Briefly, cells were grown to 80% confluency in 60mm dishes. For harvest, cells were trypsinized, then resuspended in growth medium supplemented with 10% FBS and counted. Cells were washed once in 1X PBS and once in 1X binding buffer, then resuspended in 1X binding buffer to 2E6 cells/ml concentration. 5µl of fluorochrome-conjugated annexin V was added to 100µl of cell suspension, then incubated for 15 minutes at room temperature, protected from light. 2mL of 1X binding buffer was added, then the suspension was centrifuged at 500xg for 5 minutes at room temperature. Supernatants were discarded, and pellets resuspended in 200ul of 1X binding buffer, and cells were analyzed using flow cytometry. Flow rate was set to medium, gates were set for singlets and 10,000 events were recorded per sample. The experiment was performed on three biological replicates.

Subcellular fractionation

The Subcellular Protein Fractionation Kit for Cultured Cells (Thermo Fisher Scientific) was used following the manufacturer's protocol to perform stepwise lysis of cells into cytoplasmic, membrane, nuclear soluble, chromatin-bound and cytoskeletal protein fractions.

Cloning and transfection of AAK1 isoforms

AAK1S was cloned from p667-UBC-AAK1-V5-miniTurbo_IDG-K, a gift from Ben Major (Addgene plasmid # 135255 ; http://n2t.net/addgene:135255 ; RRID:Addgene_135255) into pcDNA3.0 parent plasmid. AAK1M and AAK1L were cloned from SH-SY5Y cells. TRIzol/chloroform extraction was performed to lyse cells and partially clarify nucleic acids. Complete RNA was extracted using silica membrane columns according to manufacturer's recommended protocol (RNEasy, Qiagen). Purified RNA was eluted with nuclease-free water and quantified using A260/A280 spectra acquired on an Epoch spectrophotometer (Agilent). cDNA synthesis was performed using 1ug of RNA following the manufacturer's recommended protocol (Protoscript II, NEB). AAK1M and AAK1L isoforms were amplified using isoform-specific primers with flanking regions designed for either Gibson Assembly (AAK1M) or restriction digest cloning (AAK1L). pcDNA3.0 parent plasmid was either PCR-linearized or digested with EcoRI and NotI. Linearized plasmids were extracted from 1% agarose gel in Tris-acetate-EDTA (TAE) buffer following the manufacturer's recommended protocol (Nucleospin, Macherey-Nagel). For AAK1M, Gibson Assembly was performed following the manufacturer's protocol for 1h at 50ºC (Gibson Assembly Master Mix, New England Biolabs). For AAK1L, the insert amplicon was ligated into EcoRI/NotI-digested pcDNA3.0 overnight at 14 ºC. 2ul of Gibson Assembly or 5ul of ligation reaction were used to transform E. coli HST08 (dam-/dcm-) chemically competent lab stock (Stellar Cells, Takarabio). Plasmids from respective colonies were isolated following manufacturer's protocols (GeneJet, Invitrogen). BamHI or EcoRI/NotI restriction digest was used to screen for successful AAK1M or AAK1L integration, respectively. Positive clones were confirmed by long-read sequencing (Plasmidsaurus). pcDNA3.0 containing AAK1S, AAK1M, or AAK1L sequences were transfected into 293T cells using Lipofectamine™ 3000 Transfection Reagent following the manufacturer's recommended protocol (Thermo Fisher Scientific) for 48 hours.

Immunofluorescence microscopy of AAK1 isoforms in HEK293T cells

Cells were transfected with AAK1S-, AAK1M- or AAK1L-FLAG in pcDNA3.0 for 48 hours and imaged using an inverted fluorescence phase contrast microscope (Keyence BZ-X710) at 1,000X oil objective magnification. The experiment was performed on two biological replicates.

3.5. Supplemental figures

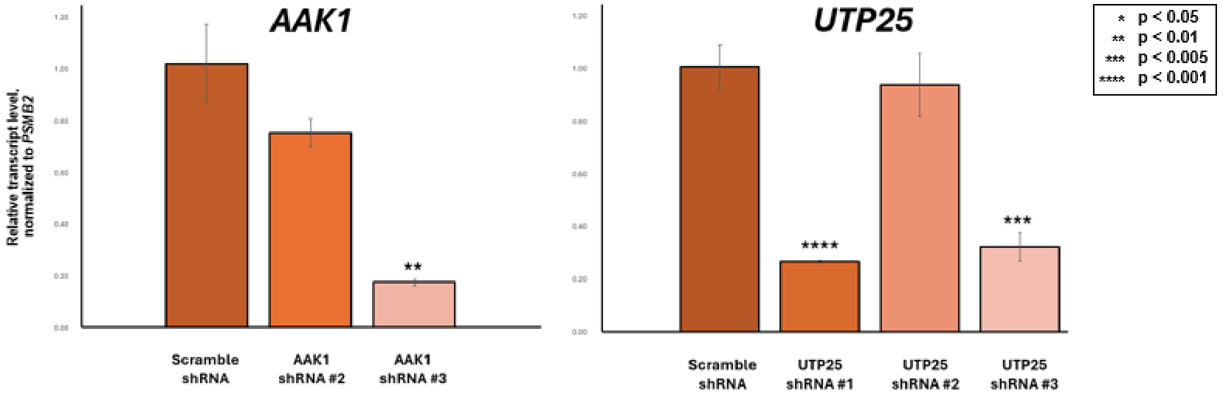

Figure S3.1. Validation of RNAi mediated knockdowns of AAK1 (from Golkowski et al. 2023) and UTP25 in FOCUS using qPCR. Cell lines with the most knockdown of each target (AAK1 shRNA #3 and UTP25 shRNA #1) were chosen for downstream experiments. Proteasome subunit beta type-2 (*PSMB2*) was used as housekeeping control gene.

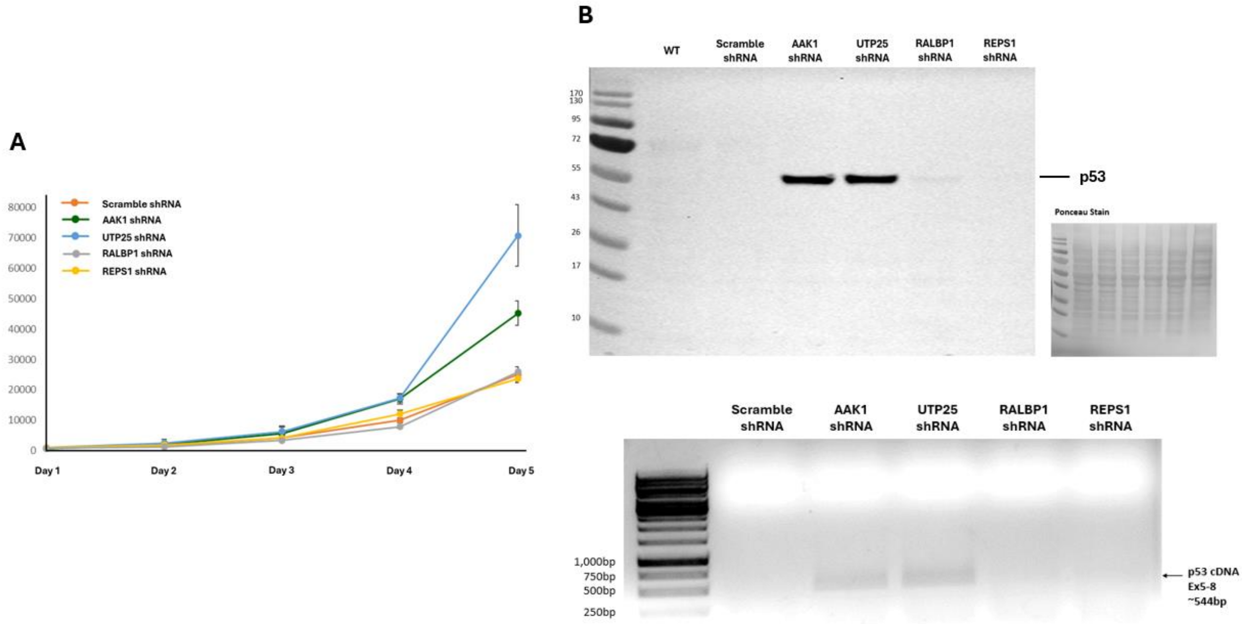

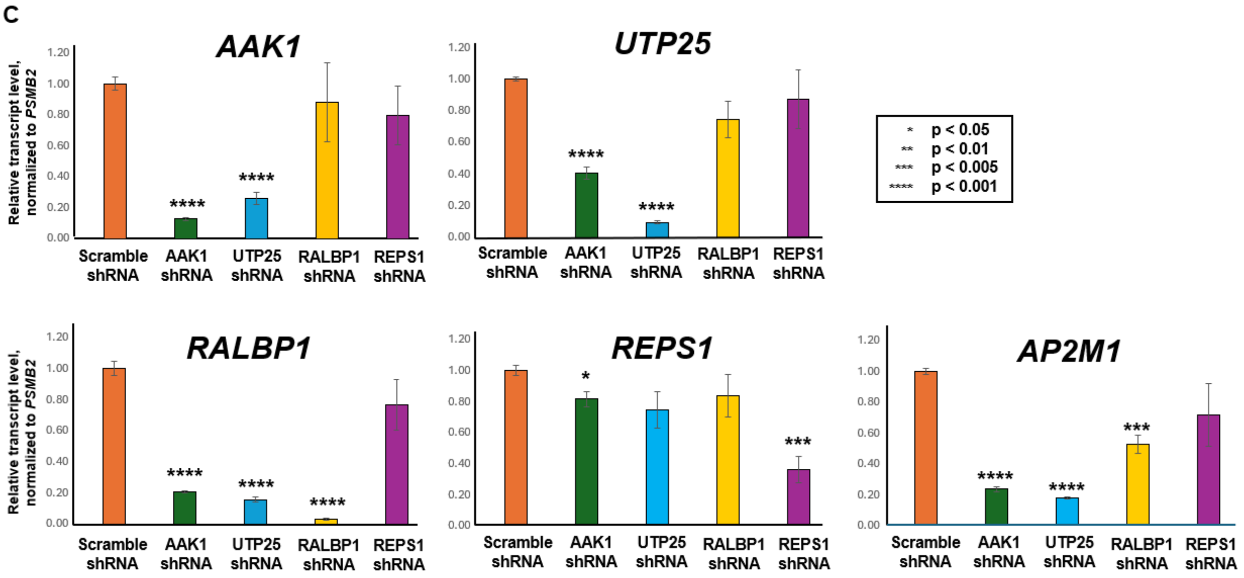

Figure S3.2. Knockdowns of AAK1 and UTP25, but not other interactors, affected A) cell proliferation rate, B) p53 stability on protein (*top*) and mRNA transcript (*bottom*) levels, and C) mRNA transcript-level expression of AAK1's interaction partners. For B, PCR-amplified cDNA was run on 1% agarose gel. GeneRuler 1kb DNA ladder (Thermo Fisher Scientific) was used as a molecular weight marker.

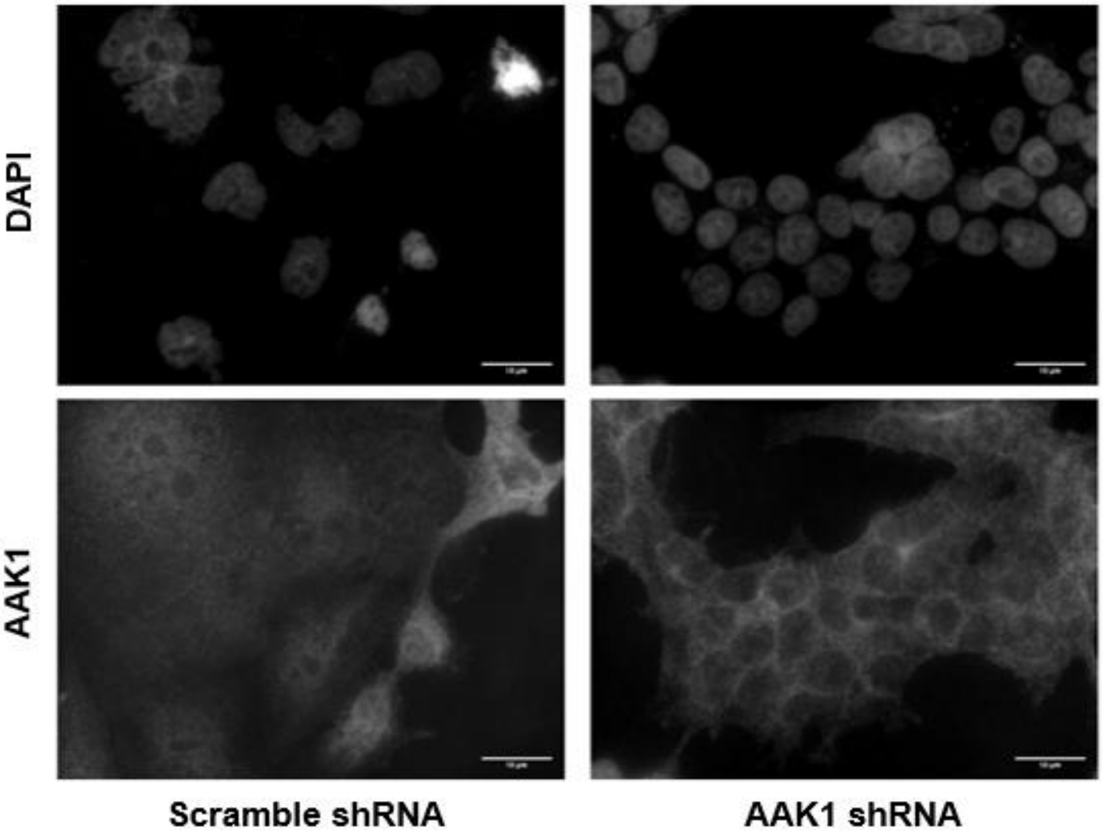

Figure S3.3. Immunofluorescence (IF) microscopy image of FOCUS Scramble and AAK1 shRNA cells. Cells were stained with IF-grade antibody against endogenous AAK1 (Thermo Fisher Scientific, PA5-82606), and images were obtained using 1,000X oil objective magnification. Scale bar represents 10um. Related to Figure 3.4.

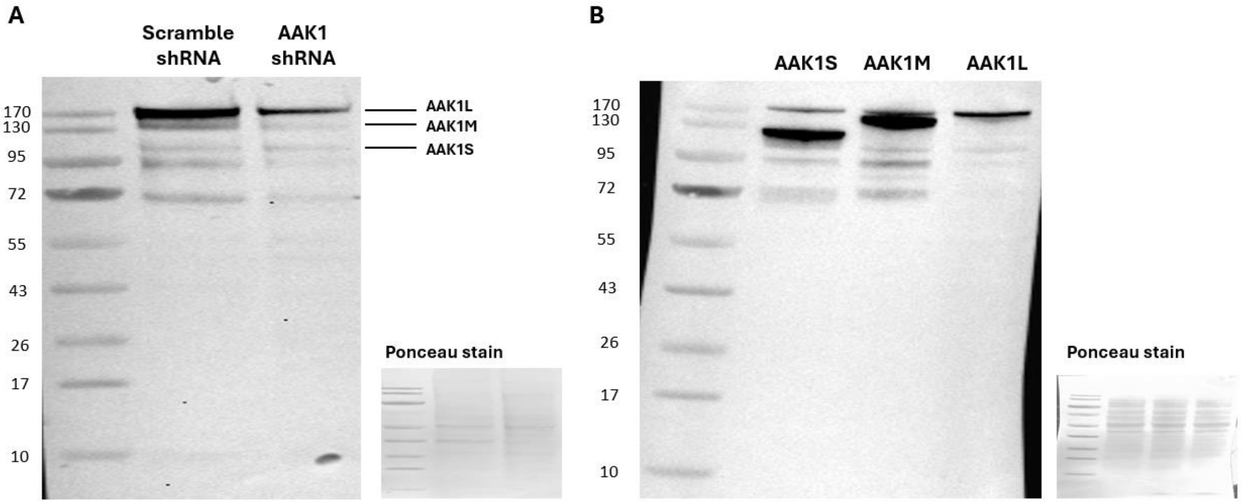

Figure S3.4. Immuoblot analysis of AAK1 isoforms in (A) FOCUS and (B) 293T cells. (A) Nucleoplasmic fractions of FOCUS Scramble and AAK1 shRNA lines using antibody against AAK1 (monoclonal, E8M3P, CST, Cat #61527). 30µg of protein (twice the usual amount) was loaded onto each lane. (B) AAK1 isoforms (AAK1S, AAK1M and AAK1L) were transiently overexpressed in 293T cells. Whole cells were lysed, and lysates were immunoblotted using antibody against AAK1 (monoclonal, E8M3P, CST, Cat #61527). Related to Figure 3.4.

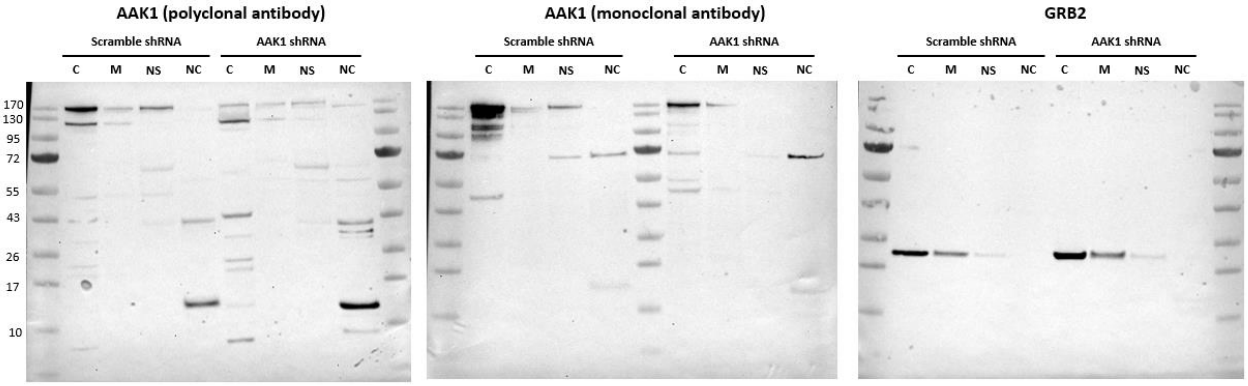

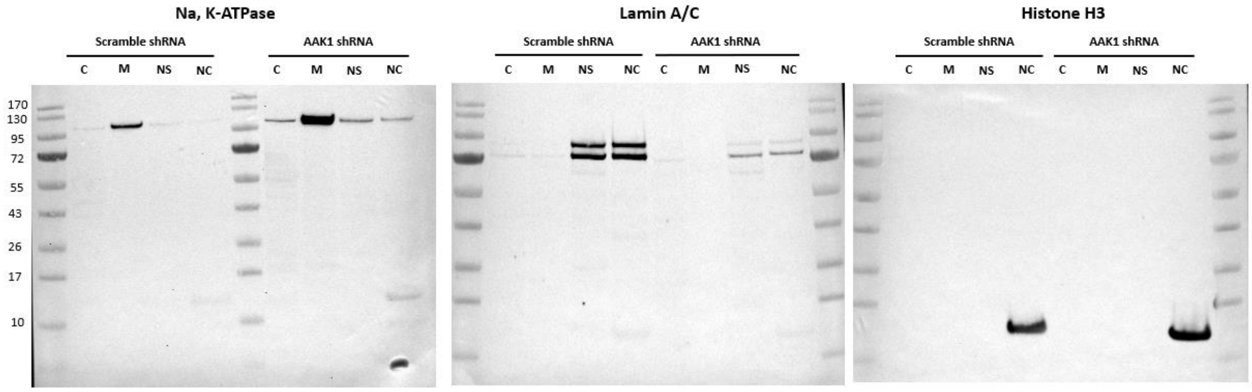

Figure S3.5. Immunoblot analysis of subcellular fractionation experiment in FOCUS Scramble and AAK1 shRNA cells using antibodies against A) AAK1 (polyclonal, CST, Cat #79832), B) AAK1 (monoclonal, E8M3P, CST, Cat #61527), C) GRB2 (CST, Cat #3972), D) Na, K-ATPase (CST, Cat #3010), E) Lamin A/C (4C11, CST, Cat #4777) and F) Histone H3 (D1H2, CST, Cat #4499). Related to Figure 3.4.

References

1. Hay, E. D. in *Epithelial–Mesenchymal Interactions: 18th Hahnemann Symposium* (eds R. Fleischmajer & Billingham, R. E.) 31–35 (Williams and Wilkins, 1968).
2. Yang, J., Antin, P., Berx, G., Blanpain, C., Brabletz, T., Bronner, M., Campbell, K., Cano, A., Casanova, J., Christofori, G., Dedhar, S., Derynck, R., Ford, H. L., Fuxe, J., García de Herreros, A., Goodall, G. J., Hadjantonakis, A. K., Huang, R. Y. J., Kalcheim, C., Kalluri, R., … EMT International Association (TEMTIA) (2020). Guidelines and definitions for research on epithelial-mesenchymal transition. *Nature reviews. Molecular cell biology*, *21*(6), 341–352. https://doi.org/10.1038/s41580-020-0237-9
3. Batlle, E., Sancho, E., Francí, C., Domínguez, D., Monfar, M., Baulida, J., & García De Herreros, A. (2000). The transcription factor snail is a repressor of E-cadherin gene expression in epithelial tumour cells. *Nature cell biology*, *2*(2), 84–89. https://doi.org/10.1038/35000034
4. Stoker, M., & Perryman, M. (1985). An epithelial scatter factor released by embryo fibroblasts. *Journal of cell science*, *77*, 209–223. https://doi.org/10.1242/jcs.77.1.209
5. Vallés, A. M., Boyer, B., Badet, J., Tucker, G. C., Barritault, D., & Thiery, J. P. (1990). Acidic fibroblast growth factor is a modulator of epithelial plasticity in a rat bladder carcinoma cell line. *Proceedings of the National Academy of Sciences of the United States of America*, *87*(3), 1124–1128. https://doi.org/10.1073/pnas.87.3.1124
6. Miettinen, P. J., Ebner, R., Lopez, A. R., & Derynck, R. (1994). TGF-beta induced transdifferentiation of mammary epithelial cells to mesenchymal cells: involvement of type I receptors. *The Journal of cell biology*, *127*(6 Pt 2), 2021–2036. https://doi.org/10.1083/jcb.127.6.2021

7. Dongre, A., & Weinberg, R. A. (2019). New insights into the mechanisms of epithelial-mesenchymal transition and implications for cancer. *Nature reviews. Molecular cell biology*, *20*(2), 69–84. https://doi.org/10.1038/s41580-018-0080-4

8. Akhmetkaliyev, A., Alibrahim, N., Shafiee, D., & Tulchinsky, E. (2023). EMT/MET plasticity in cancer and Go-or-Grow decisions in quiescence: the two sides of the same coin?. *Molecular cancer*, *22*(1), 90. https://doi.org/10.1186/s12943-023-01793-z

9. Tammela, T., Sanchez-Rivera, F. J., Cetinbas, N. M., Wu, K., Joshi, N. S., Helenius, K., Park, Y., Azimi, R., Kerper, N. R., Wesselhoeft, R. A., Gu, X., Schmidt, L., Cornwall-Brady, M., Yilmaz, Ö. H., Xue, W., Katajisto, P., Bhutkar, A., & Jacks, T. (2017). A Wnt-producing niche drives proliferative potential and progression in lung adenocarcinoma. *Nature*, *545*(7654), 355–359. https://doi.org/10.1038/nature22334

10. de Sousa e Melo, F., Kurtova, A. V., Harnoss, J. M., Kljavin, N., Hoeck, J. D., Hung, J., Anderson, J. E., Storm, E. E., Modrusan, Z., Koeppen, H., Dijkgraaf, G. J., Piskol, R., & de Sauvage, F. J. (2017). A distinct role for Lgr5$^+$ stem cells in primary and metastatic colon cancer. *Nature*, *543*(7647), 676–680. https://doi.org/10.1038/nature21713

11. Stemmer, V., de Craene, B., Berx, G., & Behrens, J. (2008). Snail promotes Wnt target gene expression and interacts with beta-catenin. *Oncogene*, *27*(37), 5075–5080. https://doi.org/10.1038/onc.2008.140

12. Sánchez-Tilló, E., Lázaro, A., Torrent, R., Cuatrecasas, M., Vaquero, E. C., Castells, A., Engel, P., & Postigo, A. (2010). ZEB1 represses E-cadherin and induces an EMT by recruiting the SWI/SNF chromatin-remodeling protein BRG1. Oncogene, 29(24), 3490–3500. https://doi.org/10.1038/onc.2010.102

13. Hoover, L. L., & Kubalak, S. W. (2008). Holding their own: the noncanonical roles of Smad proteins. *Science signaling*, *1*(46), pe48. https://doi.org/10.1126/scisignal.146pe48

14. Tang, Y., Liu, Z., Zhao, L., Clemens, T. L., & Cao, X. (2008). Smad7 stabilizes beta-catenin binding to E-cadherin complex and promotes cell-cell adhesion. *The Journal of biological chemistry*, *283*(35), 23956–23963. https://doi.org/10.1074/jbc.M800351200

15. Scheel, C., Eaton, E. N., Li, S. H., Chaffer, C. L., Reinhardt, F., Kah, K. J., Bell, G., Guo, W., Rubin, J., Richardson, A. L., & Weinberg, R. A. (2011). Paracrine and autocrine signals induce and maintain mesenchymal and stem cell states in the breast. *Cell*, *145*(6), 926–940. https://doi.org/10.1016/j.cell.2011.04.029

16. Zhang, J., Shao, X., Sun, H., Liu, K., Ding, Z., Chen, J., Fang, L., Su, W., Hong, Y., Li, H., & Li, H. (2016). NUMB negatively regulates the epithelial-mesenchymal transition of triple-negative breast cancer by antagonizing Notch signaling. *Oncotarget*, *7*(38), 61036–61053. https://doi.org/10.18632/oncotarget.11062

17. Yuan, X., Wu, H., Han, N., Xu, H., Chu, Q., Yu, S., Chen, Y., & Wu, K. (2014). Notch signaling and EMT in non-small cell lung cancer: biological significance and therapeutic application. *Journal of hematology & oncology*, *7*, 87. https://doi.org/10.1186/s13045-014-0087-z

18. Tang, Y., Tang, Y., & Cheng, Y. S. (2017). miR-34a inhibits pancreatic cancer progression through Snail1-mediated epithelial-mesenchymal transition and the Notch signaling pathway. *Scientific reports*, *7*, 38232. https://doi.org/10.1038/srep38232

19. Natsuizaka, M., Whelan, K. A., Kagawa, S., Tanaka, K., Giroux, V., Chandramouleeswaran, P. M., Long, A., Sahu, V., Darling, D. S., Que, J., Yang, Y., Katz, J. P., Wileyto, E. P., Basu, D., Kita, Y., Natsugoe, S., Naganuma, S., Klein-Szanto, A. J., Diehl, J. A., Bass, A. J., … Nakagawa, H. (2017). Interplay between Notch1 and Notch3 promotes EMT and tumor initiation in squamous cell carcinoma. *Nature communications*, *8*(1), 1758. https://doi.org/10.1038/s41467-017-01500-9

20. Matsuno, Y., Coelho, A. L., Jarai, G., Westwick, J., & Hogaboam, C. M. (2012). Notch signaling mediates TGF-β1-induced epithelial-mesenchymal transition through the induction of Snai1. *The international journal of biochemistry & cell biology*, *44*(5), 776–789. https://doi.org/10.1016/j.biocel.2012.01.021

21. Shao, S., Zhao, X., Zhang, X., Luo, M., Zuo, X., Huang, S., Wang, Y., Gu, S., & Zhao, X. (2015). Notch1 signaling regulates the epithelial-mesenchymal transition and invasion of breast cancer in a Slug-dependent manner. *Molecular cancer*, *14*(1), 28. https://doi.org/10.1186/s12943-015-0295-3

22. Conner, S. D., & Schmid, S. L. (2002). Identification of an adaptor-associated kinase, AAK1, as a regulator of clathrin-mediated endocytosis. The Journal of cell biology, 156(5), 921–929. https://doi.org/10.1083/jcb.200108123

23. Sorrell, F. J., Szklarz, M., Abdul Azeez, K. R., Elkins, J. M., & Knapp, S. (2016). Family-wide Structural Analysis of Human Numb-Associated Protein Kinases. *Structure (London, England : 1993)*, *24*(3), 401–411. https://doi.org/10.1016/j.str.2015.12.015

24. Smythe, E., & Ayscough, K. R. (2003). The Ark1/Prk1 family of protein kinases. Regulators of endocytosis and the actin skeleton. *EMBO reports*, *4*(3), 246–251. https://doi.org/10.1038/sj.embor.embor776

25. Conner, S. D., Schröter, T., & Schmid, S. L. (2003). AAK1-mediated micro2 phosphorylation is stimulated by assembled clathrin. *Traffic (Copenhagen, Denmark)*, *4*(12), 885–890. https://doi.org/10.1046/j.1398-9219.2003.0142.x

26. Pauloin, A., & Thurieau, C. (1993). The 50 kDa protein subunit of assembly polypeptide (AP) AP-2 adaptor from clathrin-coated vesicles is phosphorylated on threonine-156 by AP-1 and a soluble AP50 kinase which co-purifies with the assembly polypeptides. *The Biochemical journal*, *296 (Pt 2)*(Pt 2), 409–415. https://doi.org/10.1042/bj2960409

27. Olusanya, O., Andrews, P. D., Swedlow, J. R., & Smythe, E. (2001). Phosphorylation of threonine 156 of the mu2 subunit of the AP2 complex is essential for endocytosis in vitro and in vivo. *Current biology : CB*, *11*(11), 896–900. https://doi.org/10.1016/s0960-9822(01)00240-8

28. Ricotta, D., Conner, S. D., Schmid, S. L., von Figura, K., & Honing, S. (2002). Phosphorylation of the AP2 mu subunit by AAK1 mediates high affinity binding to membrane protein sorting signals. *The Journal of cell biology*, *156*(5), 791–795. https://doi.org/10.1083/jcb.200111068

29. Umeda, A., Meyerholz, A., & Ungewickell, E. (2000). Identification of the universal cofactor (auxilin 2) in clathrin coat dissociation. *European journal of cell biology*, *79*(5), 336–342. https://doi.org/10.1078/S0171-9335(04)70037-0

30. Conner, S. D., & Schmid, S. L. (2003). Differential requirements for AP-2 in clathrin-mediated endocytosis. *The Journal of cell biology*, *162*(5), 773–779. https://doi.org/10.1083/jcb.200304069

31. Huang, C., Ji, C., & Wang, J. (2023). Current thoughts on cellular functions of numb-associated kinases. *Molecular biology reports*, *50*(5), 4645–4652. https://doi.org/10.1007/s11033-023-08372-x

32. Groenendyk, J., & Michalak, M. (2011). A genome-wide siRNA screen identifies novel phospho-enzymes affecting Wnt/β-catenin signaling in mouse embryonic stem cells. *Stem cell reviews and reports*, *7*(4), 910–926. https://doi.org/10.1007/s12015-011-9265-3

33. Agajanian, M. J., Walker, M. P., Axtman, A. D., Ruela-de-Sousa, R. R., Serafin, D. S., Rabinowitz, A. D., Graham, D. M., Ryan, M. B., Tamir, T., Nakamichi, Y., Gammons, M. V., Bennett, J. M., Couñago, R. M., Drewry, D. H., Elkins, J. M., Gileadi, C., Gileadi, O., Godoi, P. H., Kapadia, N., Müller, S., … Major, M. B. (2019). WNT Activates the AAK1 Kinase to

Promote Clathrin-Mediated Endocytosis of LRP6 and Establish a Negative Feedback Loop. *Cell reports*, *26*(1), 79–93.e8. https://doi.org/10.1016/j.celrep.2018.12.023

34. Berdnik, D., Török, T., González-Gaitán, M., & Knoblich, J. A. (2002). The endocytic protein alpha-Adaptin is required for numb-mediated asymmetric cell division in Drosophila. *Developmental cell*, *3*(2), 221–231. https://doi.org/10.1016/s1534-5807(02)00215-0
35. Chien, C. T., Wang, S., Rothenberg, M., Jan, L. Y., & Jan, Y. N. (1998). Numb-associated kinase interacts with the phosphotyrosine binding domain of Numb and antagonizes the function of Numb in vivo. *Molecular and cellular biology*, *18*(1), 598–607. https://doi.org/10.1128/MCB.18.1.598
36. Sorensen, E. B., & Conner, S. D. (2008). AAK1 regulates Numb function at an early step in clathrin-mediated endocytosis. *Traffic (Copenhagen, Denmark)*, *9*(10), 1791–1800. https://doi.org/10.1111/j.1600-0854.2008.00790.x
37. Tokumitsu, H., Hatano, N., Yokokura, S., Sueyoshi, Y., Nozaki, N., & Kobayashi, R. (2006). Phosphorylation of Numb regulates its interaction with the clathrin-associated adaptor AP-2. *FEBS letters*, *580*(24), 5797–5801. https://doi.org/10.1016/j.febslet.2006.09.043
38. Smith, C. A., Lau, K. M., Rahmani, Z., Dho, S. E., Brothers, G., She, Y. M., Berry, D. M., Bonneil, E., Thibault, P., Schweisguth, F., Le Borgne, R., & McGlade, C. J. (2007). aPKC-mediated phosphorylation regulates asymmetric membrane localization of the cell fate determinant Numb. *The EMBO journal*, *26*(2), 468–480. https://doi.org/10.1038/sj.emboj.7601495
39. Santolini, E., Puri, C., Salcini, A. E., Gagliani, M. C., Pelicci, P. G., Tacchetti, C., & Di Fiore, P. P. (2000). Numb is an endocytic protein. *The Journal of cell biology*, *151*(6), 1345–1352. https://doi.org/10.1083/jcb.151.6.1345

40. Nie, J., McGill, M. A., Dermer, M., Dho, S. E., Wolting, C. D., & McGlade, C. J. (2002). LNX functions as a RING type E3 ubiquitin ligase that targets the cell fate determinant Numb for ubiquitin-dependent degradation. *The EMBO journal*, *21*(1-2), 93–102. https://doi.org/10.1093/emboj/21.1.93

41. Gupta-Rossi, N., Ortica, S., Meas-Yedid, V., Heuss, S., Moretti, J., Olivo-Marin, J. C., & Israël, A. (2011). The adaptor-associated kinase 1, AAK1, is a positive regulator of the Notch pathway. *The Journal of biological chemistry*, *286*(21), 18720–18730. https://doi.org/10.1074/jbc.M110.190769

42. Gupta-Rossi, N., Six, E., LeBail, O., Logeat, F., Chastagner, P., Olry, A., Israël, A., & Brou, C. (2004). Monoubiquitination and endocytosis direct gamma-secretase cleavage of activated Notch receptor. *The Journal of cell biology*, *166*(1), 73–83. https://doi.org/10.1083/jcb.200310098

43. Karim, M., Saul, S., Ghita, L., Sahoo, M. K., Ye, C., Bhalla, N., Lo, C. W., Jin, J., Park, J. G., Martinez-Gualda, B., East, M. P., Johnson, G. L., Pinsky, B. A., Martinez-Sobrido, L., Asquith, C. R. M., Narayanan, A., De Jonghe, S., & Einav, S. (2022). Numb-associated kinases are required for SARS-CoV-2 infection and are cellular targets for antiviral strategies. *Antiviral research*, *204*, 105367. https://doi.org/10.1016/j.antiviral.2022.105367

44. Neveu, G., Ziv-Av, A., Barouch-Bentov, R., Berkerman, E., Mulholland, J., & Einav, S. (2015). AP-2-associated protein kinase 1 and cyclin G-associated kinase regulate hepatitis C virus entry and are potential drug targets. *Journal of virology*, *89*(8), 4387–4404. https://doi.org/10.1128/JVI.02705-14

45. Wang, C., Wang, J., Shuai, L., Ma, X., Zhang, H., Liu, R., Chen, W., Wang, X., Ge, J., Wen, Z., & Bu, Z. (2019). The Serine/Threonine Kinase AP2-Associated Kinase 1 Plays an Important Role in Rabies Virus Entry. *Viruses*, *12*(1), 45. https://doi.org/10.3390/v12010045

46. Tongmuang, N., Yasamut, U., Noisakran, S., Sreekanth, G. P., Yenchitsomanus, P. T., & Limjindaporn, T. (2020). Suppression of μ1 subunit of the adaptor protein complex 2 reduces dengue virus release. *Virus genes*, *56*(1), 27–36. https://doi.org/10.1007/s11262-019-01710-x

47. Fu, X., Ke, M., Yu, W., Wang, X., Xiao, Q., Gu, M., & Lü, Y. (2018). Periodic Variation of AAK1 in an $A\beta_{1-42}$-Induced Mouse Model of Alzheimer's Disease. *Journal of molecular neuroscience : MN*, *65*(2), 179–189. https://doi.org/10.1007/s12031-018-1085-3

48. Latourelle, J. C., Pankratz, N., Dumitriu, A., Wilk, J. B., Goldwurm, S., Pezzoli, G., Mariani, C. B., DeStefano, A. L., Halter, C., Gusella, J. F., Nichols, W. C., Myers, R. H., Foroud, T., PROGENI Investigators, Coordinators and Molecular Genetic Laboratories, & GenePD Investigators, Coordinators and Molecular Genetic Laboratories (2009). Genomewide association study for onset age in Parkinson disease. *BMC medical genetics*, *10*, 98. https://doi.org/10.1186/1471-2350-10-98

49. Shi, B., Conner, S. D., & Liu, J. (2014). Dysfunction of endocytic kinase AAK1 in ALS. *International journal of molecular sciences*, *15*(12), 22918–22932. https://doi.org/10.3390/ijms151222918

50. Kostich, W., Hamman, B. D., Li, Y. W., Naidu, S., Dandapani, K., Feng, J., Easton, A., Bourin, C., Baker, K., Allen, J., Savelieva, K., Louis, J. V., Dokania, M., Elavazhagan, S., Vattikundala, P., Sharma, V., Das, M. L., Shankar, G., Kumar, A., Holenarsipur, V. K., … Albright, C. F. (2016). Inhibition of AAK1 Kinase as a Novel Therapeutic Approach to Treat Neuropathic Pain. *The Journal of pharmacology and experimental therapeutics*, *358*(3), 371–386. https://doi.org/10.1124/jpet.116.235333

51. Shehata, S. N., Deak, M., Collodet, C., Spiegl, S. F., Geley, S., Sumpton, D., & Sakamoto, K. (2019). Identification of novel PCTAIRE-1/CDK16 substrates using a chemical genetic screen. *Cellular signalling*, *59*, 53–61. https://doi.org/10.1016/j.cellsig.2019.03.012

52. Ultanir, S. K., Hertz, N. T., Li, G., Ge, W. P., Burlingame, A. L., Pleasure, S. J., Shokat, K. M., Jan, L. Y., & Jan, Y. N. (2012). Chemical genetic identification of NDR1/2 kinase substrates AAK1 and Rabin8 Uncovers their roles in dendrite arborization and spine development. *Neuron*, *73*(6), 1127–1142. https://doi.org/10.1016/j.neuron.2012.01.019

53. Loi, M., Müller, A., Steinbach, K., Niven, J., Barreira da Silva, R., Paul, P., Ligeon, L. A., Caruso, A., Albrecht, R. A., Becker, A. C., Annaheim, N., Nowag, H., Dengjel, J., García-Sastre, A., Merkler, D., Münz, C., & Gannagé, M. (2016). Macroautophagy Proteins Control MHC Class I Levels on Dendritic Cells and Shape Anti-viral CD8(+) T Cell Responses. *Cell reports*, *15*(5), 1076–1087. https://doi.org/10.1016/j.celrep.2016.04.002

54. Yuan, C., Ai, K., Xiang, M., Xie, C., Zhao, M., Wu, M., Li, H., Wu, Y., Cao, Y., Li, C., Zhong, Y., Pei, X., Law, H. K. W., Gao, L., Xiao, Q., & Yang, X. (2022). Novel 1-hydroxy phenothiazinium-based derivative protects against bacterial sepsis by inhibiting AAK1-mediated LPS internalization and caspase-11 signaling. *Cell death & disease*, *13*(8), 722. https://doi.org/10.1038/s41419-022-05151-7

55. Rogers, L. M., Wang, Z., Mott, S. L., Dupuy, A. J., & Weiner, G. J. (2020). A Genetic Screen to Identify Gain- and Loss-of-Function Modifications that Enhance T-cell Infiltration into Tumors. *Cancer immunology research*, *8*(9), 1206–1214. https://doi.org/10.1158/2326-6066.CIR-20-0056

56. Bekerman, E., Neveu, G., Shulla, A., Brannan, J., Pu, S. Y., Wang, S., Xiao, F., Barouch-Bentov, R., Bakken, R. R., Mateo, R., Govero, J., Nagamine, C. M., Diamond, M. S., De Jonghe, S., Herdewijn, P., Dye, J. M., Randall, G., & Einav, S. (2017). Anticancer kinase inhibitors impair intracellular viral trafficking and exert broad-spectrum antiviral effects. *The Journal of clinical investigation*, *127*(4), 1338–1352. https://doi.org/10.1172/JCI89857

57. Tang, B., Zhu, J., Cong, Y., Yang, W., Kong, C., Chen, W., Wang, Y., Zeng, Y., & Ji, J. (2020). The Landscape of Coronavirus Disease 2019 (COVID-19) and Integrated Analysis SARS-CoV-2 Receptors and Potential Inhibitors in Lung Adenocarcinoma Patients. *Frontiers in cell and developmental biology*, *8*, 577032. https://doi.org/10.3389/fcell.2020.577032

58. Moreno-González, G., Mussetti, A., Albasanz-Puig, A., Salvador, I., Sureda, A., Gudiol, C., Salazar, R., Marin, M., Garcia, M., Navarro, V., de la Haba Vaca, I., Coma, E., Sanz-Linares, G., Dura, X., Fontanals, S., Serrano, G., Cruz, C., & Mañez, R. (2021). A Phase I/II Clinical Trial to evaluate the efficacy of baricitinib to prevent respiratory insufficiency progression in onco-hematological patients affected with COVID19: A structured summary of a study protocol for a randomised controlled trial. *Trials*, *22*(1), 116. https://doi.org/10.1186/s13063-021-05072-4

59. Singh, S., Parthasarathi, K. T. S., Bhat, M. Y., Gopal, C., Sharma, J., & Pandey, A. (2024). Profiling Kinase Activities for Precision Oncology in Diffuse Gastric Cancer. *Omics : a journal of integrative biology*, *28*(2), 76–89. https://doi.org/10.1089/omi.2023.0173

60. Pan, T., He, Y., Chen, H., Pei, J., Li, Y., Zeng, R., Xia, J., Zuo, Y., Qin, L., Chen, S., Xiao, L., & Zhou, H. (2021). Identification and Validation of a Prognostic Gene Signature for Diffuse Large B-Cell Lymphoma Based on Tumor Microenvironment-Related Genes. *Frontiers in oncology*, *11*, 614211. https://doi.org/10.3389/fonc.2021.614211

61. Jia, E., Ren, N., Zhang, R., Zhou, C., & Xue, J. (2020). Circulating miR-17 as a promising diagnostic biomarker for lung adenocarcinoma: evidence from the Gene Expression Omnibus. *Translational cancer research*, *9*(9), 5544–5554. https://doi.org/10.21037/tcr-19-3025

62. Testa, U., Castelli, G., & Pelosi, E. (2024). Alk-rearranged lung adenocarcinoma: From molecular genetics to therapeutic targeting. *Tumori*, *110*(2), 88–95. https://doi.org/10.1177/03008916231202149

63. Golkowski, M., Lius, A., Sapre, T., Lau, H. T., Moreno, T., Maly, D. J., & Ong, S. E. (2023). Multiplexed kinase interactome profiling quantifies cellular network activity and plasticity. *Molecular cell*, *83*(5), 803–818.e8. https://doi.org/10.1016/j.molcel.2023.01.015

64. Zhang, Z., Huang, Y., Li, S., & Hong, L. (2024). Comprehensive analysis based on glycolytic and glutaminolytic pathways signature for predicting prognosis and immunotherapy in ovarian cancer. *Journal of Cancer*, *15*(2), 383–400. https://doi.org/10.7150/jca.88359

65. Henderson, D. M., & Conner, S. D. (2007). A novel AAK1 splice variant functions at multiple steps of the endocytic pathway. Molecular biology of the cell, 18(7), 2698–2706. https://doi.org/10.1091/mbc.e06-09-0831

66. Knop, F., Zounarová, A., Šabata, V., Middelkoop, T. C., & Macůrková, M. (2024). *Caenorhabditis elegans* SEL-5/AAK1 regulates cell migration and cell outgrowth independently of its kinase activity. *eLife*, *13*, e91054. https://doi.org/10.7554/eLife.91054

67. Chen, J., Ruan, H., Ng, S. M., Gao, C., Soo, H. M., Wu, W., Zhang, Z., Wen, Z., Lane, D. P., & Peng, J. (2005). Loss of function of def selectively up-regulates Delta113p53 expression to arrest expansion growth of digestive organs in zebrafish. Genes & development, 19(23), 2900–2911. https://doi.org/10.1101/gad.1366405

68. Charette, J. M., & Baserga, S. J. (2010). The DEAD-box RNA helicase-like Utp25 is an SSU processome component. *RNA (New York, N.Y.)*, *16*(11), 2156–2169. https://doi.org/10.1261/rna.2359810

69. Goldfeder, M. B., & Oliveira, C. C. (2010). Utp25p, a nucleolar Saccharomyces cerevisiae protein, interacts with U3 snoRNP subunits and affects processing of the 35S pre-rRNA. *The FEBS journal*, *277*(13), 2838–2852. https://doi.org/10.1111/j.1742-4658.2010.07701.x

70. Bao, J., Su, B., Chen, Z., Sun, Z., Peng, J., & Zhao, S. (2024). A UTP3-dependent nucleolar translocation pathway facilitates pre-rRNA 5'ETS processing. *Nucleic acids research*, *52*(16), 9671–9694. https://doi.org/10.1093/nar/gkae631

71. Tao, T., Sondalle, S. B., Shi, H., Zhu, S., Perez-Atayde, A. R., Peng, J., Baserga, S. J., & Look, A. T. (2017). The pre-rRNA processing factor DEF is rate limiting for the pathogenesis of MYCN-driven neuroblastoma. *Oncogene*, *36*(27), 3852–3867. https://doi.org/10.1038/onc.2016.527

72. Huang, W., Chen, F., Ma, Q., Xin, J., Li, J., Chen, J., Zhou, B., Chen, M., Li, J., & Peng, J. (2020). Ribosome biogenesis gene DEF/UTP25 is essential for liver homeostasis and regeneration. *Science China. Life sciences*, *63*(11), 1651–1664. https://doi.org/10.1007/s11427-019-1635-2

73. Tao, T., Shi, H., Guan, Y., Huang, D., Chen, Y., Lane, D. P., Chen, J., & Peng, J. (2013). Def defines a conserved nucleolar pathway that leads p53 to proteasome-independent degradation. Cell research, 23(5), 620–634. https://doi.org/10.1038/cr.2013.16

74. Guan, Y., Huang, D., Chen, F., Gao, C., Tao, T., Shi, H., Zhao, S., Liao, Z., Lo, L. J., Wang, Y., Chen, J., & Peng, J. (2016). Phosphorylation of Def Regulates Nucleolar p53 Turnover and Cell Cycle Progression through Def Recruitment of Calpain3. PLoS biology, 14(9), e1002555. https://doi.org/10.1371/journal.pbio.1002555

75. Vidal, M., Cusick, M.E., and Baraba´ si, A.L. (2011). Interactome networks and human disease. Cell 144, 986–998. https://doi.org/10.1016/j.cell. 2011.02.016

76. Nussinov, R. (2013). The spatial structure of cell signaling systems. Phys. Biol. 10, 045004. https://doi.org/10.1088/1478-3975/10/4/045004

77. Cheng, F., Zhao, J., Wang, Y., Lu, W., Liu, Z., Zhou, Y., Martin, W.R., Wang, R., Huang, J., Hao, T., et al. (2021). Comprehensive characterization of protein-protein interactions perturbed by disease mutations. Nat. Genet. 53, 342–353. https://doi.org/10.1038/s41588-020-00774-y

78. Huttlin, E.L., Bruckner, R.J., Paulo, J.A., Cannon, J.R., Ting, L., Baltier, K., Colby, G., Gebreab, F., Gygi, M.P., Parzen, H., et al. (2017). Architecture of the human interactome defines protein communities and disease networks. Nature 545, 505–509. https://doi.org/10.1038/nature22366

79. Taylor, I.W., and Wrana, J.L. (2012). Protein interaction networks in medicine and disease. Proteomics 12, 1706–1716. https://doi.org/10.1002/ pmic.201100594

80. Duan, G., and Walther, D. (2015). The roles of post-translational modifications in the context of protein interaction networks. PLoS Comput. Biol. 11, e1004049. https://doi.org/10.1371/journal.pcbi.1004049

81. Manning, G., Whyte, D.B., Martinez, R., Hunter, T., and Sudarsanam, S. (2002). The protein kinase complement of the human genome. Science 298, 1912–1934. https://doi.org/10.1126/science.1075762

82. Ferguson, F.M., and Gray, N.S. (2018). Kinase inhibitors: the road ahead. Nat. Rev. Drug Discov. 17, 353–377. https://doi.org/10.1038/nrd.2018.21

83. Fleuren, E.D., Zhang, L., Wu, J., and Daly, R.J. (2016). The kinome ’at large’ in cancer. Nat. Rev. Cancer 16, 83–98. https://doi.org/10.1038/ nrc.2015.18

84. Moret, N., Liu, C., Gyori, B.M., Bachman, J.A., Steppi, A., Hug, C., Taujale, R., Huang, L.-C., Berginski, M.E., Gomez, S.M., et al. (2021). A resource for exploring the understudied human kinome for research and therapeutic opportunities. bioRxiv. https://doi.org/10.1101/2020.04.02.022277

85. Lu, H., Zhou, Q., He, J., Jiang, Z., Peng, C., Tong, R., and Shi, J. (2020). Recent advances in the development of protein-protein interactions modulators: mechanisms and clinical trials. Signal Transduct. Target. Ther. 5, 213. https://doi.org/10.1038/s41392-020-00315-3

86. Buljan, M., Ciuffa, R., van Drogen, A., Vichalkovski, A., Mehnert, M., Rosenberger, G., Lee, S., Varjosalo, M., Pernas, L.E., Spegg, V., et al. (2020). Kinase interaction network expands functional and disease roles of human kinases. Mol. Cell 79, 504–520.e9. https://doi.org/10.1016/j. molcel.2020.07.001

87. Huttlin, E.L., Bruckner, R.J., Navarrete-Perea, J., Cannon, J.R., Baltier, K., Gebreab, F., Gygi, M.P., Thornock, A., Zarraga, G., Tam, S., et al. (2021). Dual proteome-scale networks reveal cell-specific remodeling of the human interactome. Cell 184, 3022–3040.e28. https://doi.org/10.1016/j. cell.2021.04.011

88. Roux, K.J., Kim, D.I., Raida, M., and Burke, B. (2012). A promiscuous biotin ligase fusion protein identifies proximal and interacting proteins in mammalian cells. J. Cell Biol. 196, 801–810. https://doi.org/10.1083/jcb. 201112098

89. Go¨ o¨ s, H., Kinnunen, M., Salokas, K., Tan, Z., Liu, X., Yadav, L., Zhang, Q., Wei, G.H., and Varjosalo, M. (2022). Human transcription factor protein interaction networks. Nat. Commun. 13, 766. https://doi.org/10.1038/ s41467-022-28341-5

90. Rhee, H.W., Zou, P., Udeshi, N.D., Martell, J.D., Mootha, V.K., Carr, S.A., and Ting, A.Y. (2013). Proteomic mapping of mitochondria in living cells via spatially restricted enzymatic tagging. Science 339, 1328–1331. https:// doi.org/10.1126/science.1230593

91. Richards, A.L., Eckhardt, M., and Krogan, N.J. (2021). Mass spectrometry-based protein-protein interaction networks for the study of human diseases. Mol. Syst. Biol. 17, e8792. https://doi.org/10.15252/msb. 20188792

92. Qin, W., Cho, K.F., Cavanagh, P.E., and Ting, A.Y. (2021). Deciphering molecular interactions by proximity labeling. Nat. Methods 18, 133–143. https://doi.org/10.1038/s41592-020-01010-5

93. Kristensen, A.R., Gsponer, J., and Foster, L.J. (2012). A high-throughput approach for measuring temporal changes in the interactome. Nat. Methods 9, 907–909. https://doi.org/10.1038/nmeth.2131

94. O'Reilly, F.J., and Rappsilber, J. (2018). Cross-linking mass spectrometry: methods and applications in structural, molecular and systems biology. ll Resource 816 Molecular Cell 83, 803–818, March 2, 2023 Nat. Struct. Mol. Biol. 25, 1000–1008. https://doi.org/10.1038/s41594- 018-0147-0

95. Bantscheff, M., Eberhard, D., Abraham, Y., Bastuck, S., Boesche, M., Hobson, S., Mathieson, T., Perrin, J., Raida, M., Rau, C., et al. (2007). Quantitative chemical proteomics reveals mechanisms of action of clinical ABL kinase inhibitors. Nat. Biotechnol. 25, 1035–1044. https://doi.org/10. 1038/nbt1328

96. Klaeger, S., Heinzlmeir, S., Wilhelm, M., Polzer, H., Vick, B., Koenig, P.A., Reinecke, M., Ruprecht, B., Petzoldt, S., Meng, C., et al. (2017). The target landscape of clinical kinase drugs. Science 358, eaan4368. https://doi. org/10.1126/science.aan4368

97. Golkowski, M., Vidadala, R.S., Lombard, C.K., Suh, H.W., Maly, D.J., and Ong, S.E. (2017). Kinobead and single-shot LC-MS profiling identifies selective PKD inhibitors. J. Proteome Res. 16, 1216–1227. https://doi.org/ 10.1021/acs.jproteome.6b00817

98. Duncan, J.S., Whittle, M.C., Nakamura, K., Abell, A.N., Midland, A.A., Zawistowski, J.S., Johnson, N.L., Granger, D.A., Jordan, N.V., Darr, D.B., et al. (2012). Dynamic reprogramming of the kinome in response to targeted MEK inhibition in triple-negative breast cancer. Cell 149, 307–321. https://doi.org/10.1016/j.cell.2012.02.053

99. Daub, H., Olsen, J.V., Bairlein, M., Gnad, F., Oppermann, F.S., Ko¨ rner, R., Greff, Z., Ke´ri, G., Stemmann, O., and Mann, M. (2008). Kinase-selective enrichment enables quantitative phosphoproteomics of the kinome across the cell cycle. Mol. Cell 31, 438–448. https://doi.org/10.1016/j.molcel.2008.07.007

100. Shibue, T., and Weinberg, R.A. (2017). EMT, CSCS, and drug resistance: the mechanistic link and clinical implications. Nat. Rev. Clin. Oncol. 14, 611–629. https://doi.org/10.1038/nrclinonc.2017.44

101. Lamouille, S., Xu, J., and Derynck, R. (2014). Molecular mechanisms of epithelial-mesenchymal transition. Nat. Rev. Mol. Cell Biol. 15, 178–196. https://doi.org/10.1038/nrm3758

102. Boumahdi, S., and de Sauvage, F.J. (2020). The great escape: tumour cell plasticity in resistance to targeted therapy. Nat. Rev. Drug Discov. 19, 39–56. https://doi.org/10.1038/s41573-019-0044-1

103. Sharma, K., Kumar, C., Ke´ri, G., Breitkopf, S.B., Oppermann, F.S., and Daub, H. (2010). Quantitative analysis of kinase-proximal signaling in lipopolysaccharide-induced innate immune response. J. Proteome Res. 9, 2539–2549. https://doi.org/10.1021/pr901192p

104. Golkowski, M., Perera, G.K., Vidadala, V.N., Ojo, K.K., Van Voorhis, W.C., Maly, D.J., and Ong, S.E. (2018). Kinome chemoproteomics characterization of pyrrolo[3,4-c]pyrazoles as potent and selective inhibitors of glycogen synthase kinase 3. Mol. Omics 14, 26–36. https://doi.org/10. 1039/c7mo00006e

105. Golkowski, M., Lau, H.T., Chan, M., Kenerson, H., Vidadala, V.N., Shoemaker, A., Maly, D.J., Yeung, R.S., Gujral, T.S., and Ong, S.E. (2020). Pharmacoproteomics identifies kinase pathways that drive the epithelial-mesenchymal transition and drug resistance in hepatocellular carcinoma. Cell Syst. 11, 196–207.e7. https://doi.org/10.1016/j.cels.2020.07.006

106. Golkowski, M., Vidadala, V.N., Lau, H.T., Shoemaker, A., ShimizuAlbergine, M., Beavo, J., Maly, D.J., and Ong, S.E. (2020). Kinobead/LCMS Phosphokinome profiling enables rapid analyses of kinase-dependent cell signaling networks. J. Proteome Res. 19, 1235–1247. https://doi.org/ 10.1021/acs.jproteome.9b00742

107. Ong, S.E., Schenone, M., Margolin, A.A., Li, X., Do, K., Doud, M.K., Mani, D.R., Kuai, L., Wang, X., Wood, J.L., et al. (2009). Identifying the proteins to which small-molecule probes and drugs bind in cells. Proc. Natl. Acad. Sci. USA 106, 4617–4622. https://doi.org/10.1073/pnas.0900191106

108. Szklarczyk, D., Gable, A.L., Nastou, K.C., Lyon, D., Kirsch, R., Pyysalo, S., Doncheva, N.T., Legeay, M., Fang, T., Bork, P., et al. (2021). The STRING database in 2021: customizable protein-protein networks, and functional characterization of user-uploaded gene/measurement sets. Nucleic Acids Res. 49, D605–D612. https://doi.org/10.1093/nar/gkaa1074

109. Oughtred, R., Stark, C., Breitkreutz, B.J., Rust, J., Boucher, L., Chang, C., Kolas, N., O'Donnell, L., Leung, G., McAdam, R., et al. (2019). The BioGRID interaction database: 2019 update. Nucleic Acids Res. 47, D529–D541. https://doi.org/10.1093/nar/gky1079

110. Ross, R.A., Spengler, B.A., and Biedler, J.L. (1983). Coordinate morphological and biochemical interconversion of human neuroblastoma cells. J. Natl. Cancer Inst. 71, 741–747.

111. Gautier, M., Thirant, C., Delattre, O., and Janoueix-Lerosey, I. (2021). Plasticity in neuroblastoma cell identity defines a noradrenergic-tomesenchymal transition (NMT). Cancers (Basel) 13, 2904. https://doi. org/10.3390/cancers13122904

112. Barretina, J., Caponigro, G., Stransky, N., Venkatesan, K., Margolin, A.A., Kim, S., Wilson, C.J., Leha´r, J., Kryukov, G.V., Sonkin, D., et al. (2012). The Cancer Cell Line Encyclopedia enables predictive modelling of anticancer drug sensitivity. Nature 483, 603–607. https://doi.org/10.1038/ nature11003

113. Gao, Z., Lee, P., Stafford, J.M., von Schimmelmann, M., Schaefer, A., and Reinberg, D. (2014). An AUTS2-Polycomb complex activates gene expression in the CNS. Nature 516, 349–354. https://doi.org/10.1038/ nature13921

114. Olsen, J.V., Blagoev, B., Gnad, F., Macek, B., Kumar, C., Mortensen, P., and Mann, M. (2006). Global, in vivo, and site-specific phosphorylation dynamics in signaling networks. Cell 127, 635–648. https://doi.org/10.1016/j. cell.2006.09.026

115. Hornbeck, P.V., Zhang, B., Murray, B., Kornhauser, J.M., Latham, V., and Skrzypek, E. (2015). PhosphoSitePlus, 2014: mutations, PTMs and recalibrations. Nucleic Acids Res. 43, D512–D520. https://doi.org/10.1093/nar/ gku1267

116. UniProt Consortium (2021). UniProt: the universal protein knowledgebase in 2021. Nucleic Acids Res. 49, D480–D489. https://doi.org/10.1093/nar/ gkaa1100

117. Villanueva, A. (2019). Hepatocellular carcinoma. N. Engl. J. Med. 380, 1450–1462. https://doi.org/10.1056/NEJMra1713263

118. Giannelli, G., Koudelkova, P., Dituri, F., and Mikulits, W. (2016). Role of epithelial to mesenchymal transition in hepatocellular carcinoma. J. Hepatol. 65, 798–808. https://doi.org/10.1016/j.jhep.2016.05.007

119. Krug, K., Mertins, P., Zhang, B., Hornbeck, P., Raju, R., Ahmad, R., Szucs, M., Mundt, F., Forestier, D., Jane-Valbuena, J., et al. (2019). A curated resource for phosphosite-specific signature analysis. Mol. Cell. Proteomics 18, 576–593. https://doi.org/10.1074/mcp.TIR118.000943

120. Subramanian, A., Tamayo, P., Mootha, V.K., Mukherjee, S., Ebert, B.L., Gillette, M.A., Paulovich, A., Pomeroy, S.L., Golub, T.R., Lander, E.S., et al. (2005). Gene set enrichment analysis: a knowledge-based approach for interpreting genome-wide expression profiles. Proc. Natl. Acad. Sci. USA 102, 15545–15550. https://doi.org/10.1073/pnas.0506580102

121. He, H., Dai, F., Yu, L., She, X., Zhao, Y., Jiang, J., Chen, X., and Zhao, S. (2002). Identification and characterization of nine novel human small GTPases showing variable expressions in liver cancer tissues. Gene Expr. 10, 231–242. https://doi.org/10.3727/000000002783992406

122. Wang, W., Jia, W.D., Hu, B., and Pan, Y.Y. (2017). RAB10 overexpression promotes tumor growth and indicates poor prognosis of hepatocellular carcinoma. Oncotarget 8, 26434–26447. https://doi.org/10.18632/oncotarget.15507

123. Mellman, I., and Yarden, Y. (2013). Endocytosis and cancer. Cold Spring Harb. Perspect. Biol. 5, a016949. https://doi.org/10.1101/cshperspect. a016949

124. Corallino, S., Malabarba, M.G., Zobel, M., Di Fiore, P.P., and Scita, G. (2015). Epithelial-to-mesenchymal plasticity harnesses endocytic circuitries. Front. Oncol. 5, 45. https://doi.org/10.3389/fonc.2015.00045

125. Aiello, N.M., Maddipati, R., Norgard, R.J., Balli, D., Li, J., Yuan, S., Yamazoe, T., Black, T., Sahmoud, A., Furth, E.E., et al. (2018). EMT subtype influences epithelial plasticity and mode of cell migration. Dev. Cell 45, 681–695.e4. https://doi.org/10.1016/j.devcel.2018.05.027. ll Resource Molecular Cell 83, 803–818, March 2, 2023 817

126. Nakashima, S., Morinaka, K., Koyama, S., Ikeda, M., Kishida, M., Okawa, K., Iwamatsu, A., Kishida, S., and Kikuchi, A. (1999). Small G protein Ral and its downstream molecules regulate endocytosis of EGF and insulin receptors. EMBO J. 18, 3629–3642. https://doi.org/10.1093/emboj/18. 13.3629

127. Penninkhof, F., Grootegoed, J.A., and Blok, L.J. (2004). Identification of REPS2 as a putative modulator of NF-kappaB activity in prostate cancer cells. Oncogene 23, 5607–5615. https://doi.org/10.1038/sj.onc.1207750

128. Oshiro, T., Koyama, S., Sugiyama, S., Kondo, A., Onodera, Y., Asahara, T., Sabe, H., and Kikuchi, A. (2002). Interaction of POB1, a downstream molecule of small G protein Ral, with PAG2, a paxillin-binding protein, is involved in cell migration. J. Biol. Chem. 277, 38618–38626. https://doi. org/10.1074/jbc.M203453200

129. Jullien-Flores, V., Dorseuil, O., Romero, F., Letourneur, F., Saragosti, S., Berger, R., Tavitian, A., Gacon, G., and Camonis, J.H. (1995). Bridging Ral GTPase to Rho pathways. RLIP76, a

Ral effector with CDC42/Rac GTPase-activating protein activity. J. Biol. Chem. 270, 22473–22477. https://doi.org/10.1074/jbc.270.38.22473

130. Jullien-Flores, V., Mahe´ , Y., Mirey, G., Leprince, C., Meunier-Bisceuil, B., Sorkin, A., and Camonis, J.H. (2000). RLIP76, an effector of the GTPase Ral, interacts with the AP2 complex: involvement of the Ral pathway in receptor endocytosis. J. Cell Sci. 113, 2837–2844

131. Lenoir, W.F., Morgado, M., DeWeirdt, P.C., McLaughlin, M., Griffith, A.L., Sangree, A.K., Feeley, M.N., Esmaeili Anvar, N., Kim, E., Bertolet, L.L., et al. (2021). Discovery of putative tumor suppressors from CRISPR screens reveals rewired lipid metabolism in acute myeloid leukemia cells. Nat. Commun. 12, 6506. https://doi.org/10.1038/s41467-021-26867-8

132. Dustin, D., Gu, G., Beyer, A.R., Herzog, S.K., Edwards, D.G., Lin, H., Gonzalez, T.L., Grimm, S.L., Coarfa, C., Chan, D.W., et al. (2021). RON signalling promotes therapeutic resistance in ESR1 mutant breast cancer. Br. J. Cancer 124, 191–206. https://doi.org/10.1038/s41416-020-01174-z

133. Kurimchak, A.M., Shelton, C., Duncan, K.E., Johnson, K.J., Brown, J., O'Brien, S., Gabbasov, R., Fink, L.S., Li, Y., Lounsbury, N., et al. (2016). Resistance to BET bromodomain inhibitors is mediated by kinome reprogramming in ovarian cancer. Cell Rep. 16, 1273–1286. https://doi.org/10. 1016/j.celrep.2016.06.091

134. Mundt, F., Rajput, S., Li, S., Ruggles, K.V., Mooradian, A.D., Mertins, P., Gillette, M.A., Krug, K., Guo, Z., Hoog, J., et al. (2018). Mass spectrometry-based proteomics reveals potential roles of NEK9 and MAP2K4 in resistance to PI3K inhibition in triple-negative breast cancers. Cancer Res. 78, 2732–2746. https://doi.org/10.1158/0008-5472.CAN-17-1990

135. Wang, C., Wang, H., Lieftink, C., du Chatinier, A., Gao, D., Jin, G., Jin, H., Beijersbergen, R.L., Qin, W., and Bernards, R. (2020). CDK12 inhibition mediates DNA damage and is synergistic with sorafenib treatment in hepatocellular carcinoma. Gut 69, 727–736. https://doi.org/10.1136/gutjnl2019-318506

136. Yam, J.W., Tse, E.Y., and Ng, I.O. (2009). Role and significance of focal adhesion proteins in hepatocellular carcinoma. J. Gastroenterol. Hepatol. 24, 520–530. https://doi.org/10.1111/j.1440-1746.2009.05813.x

137. Jiang, X., Tan, H.Y., Teng, S., Chan, Y.T., Wang, D., and Wang, N. (2019). The role of AMP-activated protein kinase as a potential target of treatment of hepatocellular carcinoma. Cancers (Basel) 11. https://doi.org/10.3390/ cancers11050647

138. Patricelli, M.P., Nomanbhoy, T.K., Wu, J., Brown, H., Zhou, D., Zhang, J., Jagannathan, S., Aban, A., Okerberg, E., Herring, C., et al. (2011). In situ kinase profiling reveals functionally relevant properties of native kinases. Chem. Biol. 18, 699–710. https://doi.org/10.1016/j.chembiol.2011.04.011

139. Bello, T., Chan, M., Golkowski, M., Xue, A.G., Khasnavis, N., Ceribelli, M., Ong, S.E., Thomas, C.J., and Gujral, T.S. (2021). KiRNet: kinase-centered network propagation of pharmacological screen results. Cell Rep. Methods 1, 100007. https://doi.org/10.1016/j.crmeth.2021.100007

140. Golkowski, M., Maly, D.J., and Ong, S.E. (2017). Proteomic profiling of protein kinase inhibitor targets by mass spectrometry. Methods Mol. Biol. 1636, 105–117. https://doi.org/10.1007/978-1-4939-7154-1_8

141. He, L., Isselbacher, K.J., Wands, J.R., Goodman, H.M., Shih, C., and Quaroni, A. (1984). Establishment and characterization of a new human hepatocellular carcinoma cell line. In Vitro 20, 493–504

142. Cox, J., Neuhauser, N., Michalski, A., Scheltema, R.A., Olsen, J.V., and Mann, M. (2011). Andromeda: a peptide search engine integrated into the MaxQuant environment. J. Proteome Res. 10, 1794–1805. https:// doi.org/10.1021/pr101065j

143. Tyanova, S., Temu, T., Sinitcyn, P., Carlson, A., Hein, M.Y., Geiger, T., Mann, M., and Cox, J. (2016). The Perseus computational platform for comprehensive analysis of (prote)omics data. Nat. Methods 13, 731–740. https://doi.org/10.1038/nmeth.3901

144. Chatr-Aryamontri, A., Oughtred, R., Boucher, L., Rust, J., Chang, C., Kolas, N.K., O'Donnell, L., Oster, S., Theesfeld, C., Sellam, A., et al. (2017). The BioGRID interaction database: 2017 update. Nucleic Acids Res. 45, D369–D379. https://doi.org/10.1093/nar/gkw1102

145. Hulsen, T., de Vlieg, J., and Alkema, W. (2008). BioVenn - a web application for the comparison and visualization of biological lists using area-proportional Venn diagrams. BMC Genomics 9, 488. https://doi.org/10.1186/ 1471-2164-9-488

146. Eid, S., Turk, S., Volkamer, A., Rippmann, F., and Fulle, S. (2017). KinMap: a web-based tool for interactive navigation through human kinome data. BMC Bioinformatics 18, 16. https://doi.org/10.1186/s12859-016-1433-7

147. Moffat, J., Grueneberg, D.A., Yang, X., Kim, S.Y., Kloepfer, A.M., Hinkle, G., Piqani, B., Eisenhaure, T.M., Luo, B., Grenier, J.K., et al. (2006). A lentiviral RNAi library for human and mouse genes applied to an arrayed viral high-content screen. Cell 124, 1283–1298. https://doi.org/10.1016/j.cell. 2006.01.040

148. Golkowski, M., Brigham, J.L., Perera, G.K., Romano, G.E., Maly, D.J., and Ong, S.E. (2014). Rapid profiling of protein kinase inhibitors by quantitative proteomics. Medchemcomm 5, 363–369. https://doi.org/10.1039/ C3MD00315A

149. Rappsilber, J., Mann, M., and Ishihama, Y. (2007). Protocol for micro-purification, enrichment, pre-fractionation and storage of peptides for proteomics using StageTips. Nat. Protoc. 2, 1896–1906. https://doi.org/10. 1038/nprot.2007.261

150. Ryoo, H. D., & Bergmann, A. (2012). The role of apoptosis-induced proliferation for regeneration and cancer. Cold Spring Harbor perspectives in biology, 4(8), a008797. https://doi.org/10.1101/cshperspect.a008797

151. Dechat, T., Pfleghaar, K., Sengupta, K., Shimi, T., Shumaker, D. K., Solimando, L., & Goldman, R. D. (2008). Nuclear lamins: major factors in the structural organization and function of the nucleus and chromatin. Genes & development, 22(7), 832–853. https://doi.org/10.1101/gad.1652708

152. Mancini, M. A., Shan, B., Nickerson, J. A., Penman, S., & Lee, W. H. (1994). The retinoblastoma gene product is a cell cycle-dependent, nuclear matrix-associated protein. Proceedings of the National Academy of Sciences of the United States of America, 91(1), 418–422. https://doi.org/10.1073/pnas.91.1.418

153. Fraser, P., & Bickmore, W. (2007). Nuclear organization of the genome and the potential for gene regulation. Nature, 447(7143), 413–417. https://doi.org/10.1038/nature05916

154. Lanctôt, C., Cheutin, T., Cremer, M., Cavalli, G., & Cremer, T. (2007). Dynamic genome architecture in the nuclear space: regulation of gene expression in three dimensions. Nature reviews. Genetics, 8(2), 104–115. https://doi.org/10.1038/nrg2041

155. Zuo, L., Zhao, H., Yang, R., Wang, L., Ma, H., Xu, X., Zhou, P., & Kong, L. (2018). Lamin A/C might be involved in the EMT signalling pathway. Gene, 663, 51–64. https://doi.org/10.1016/j.gene.2018.04.040

156. Hu, C., Zhou, A., Hu, X., Xiang, Y., Huang, M., Huang, J., Yang, D., & Tang, Y. (2022). LMNA Reduced Acquired Resistance to Erlotinib in NSCLC by Reversing the Epithelial-Mesenchymal Transition via the FGFR/MAPK/c-fos Signaling Pathway. International journal of molecular sciences, 23(21), 13237. https://doi.org/10.3390/ijms232113237

157. Fan, J. R., Chang, S. N., Chu, C. T., & Chen, H. C. (2023). AKT2-mediated nuclear deformation leads to genome instability during epithelial-mesenchymal transition. iScience, 26(6), 106992. https://doi.org/10.1016/j.isci.2023.106992

158. Kosugi, S., Hasebe, M., Tomita, M., & Yanagawa, H. (2009). Systematic identification of cell cycle-dependent yeast nucleocytoplasmic shuttling proteins by prediction of composite motifs. Proceedings of the National Academy of Sciences of the United States of America, 106(25), 10171–10176. https://doi.org/10.1073/pnas.0900604106

159. Kosugi, S., Hasebe, M., Matsumura, N., Takashima, H., Miyamoto-Sato, E., Tomita, M., & Yanagawa, H. (2009). Six classes of nuclear localization signals specific to different binding grooves of importin alpha. The Journal of biological chemistry, 284(1), 478–485. https://doi.org/10.1074/jbc.M807017200

160. Kosugi, S., Hasebe, M., Entani, T., Takayama, S., Tomita, M., & Yanagawa, H. (2008). Design of peptide inhibitors for the importin alpha/beta nuclear import pathway by activity-based profiling. Chemistry & biology, 15(9), 940–949. https://doi.org/10.1016/j.chembiol.2008.07.019